

# **ELECTRONIC INTERACTIONS AT NOBLE METAL SURFACES STUDIED BY SCANNING TUNNELING MICROSCOPY**

**THÈSE N° 2659 (2002)**

**PRÉSENTÉE À LA FACULTÉ SCIENCES DE BASE**

**SECTION DE LA PHYSIQUE**

**ÉCOLE POLYTECHNIQUE FÉDÉRALE DE LAUSANNE**

**POUR L'OBTENTION DU GRADE DE DOCTEUR ÈS SCIENCES**

**PAR**

**Nikolaus KNORR**

**Diplom-Physiker, Universität Kaiserslautern, Allemagne  
de nationalité allemande**

**acceptée sur proposition du jury:**

**Prof. K. Kern, directeur de thèse  
Prof. B. Deveaud-Plédran, rapporteur  
Prof. H. Kroha, rapporteur  
Dr D. Pavuna, rapporteur  
Prof. L. Schlapbach, rapporteur**

**Lausanne, EPFL  
2002**

# Abstract

In this thesis, the unique possibilities offered by a cryogenic scanning tunneling microscope (STM) have been exploited to study aspects of the interaction of bulk conduction band and surface-state electrons with adsorbates on noble metal surfaces: one topic is the long-range lateral interaction between adsorbates mediated by a surface-state electron gas, another the correlation of conduction electrons due to scattering at magnetic adsorbates, called Kondo effect, with special interest in the spatial extent of the correlation for surface-state and bulk conduction electrons.

Adsorbates interact via many types of interaction like the direct chemical interaction and the indirect electrostatic (dipole-dipole), elastic (deformation of substrate lattice) and electronic interactions (Friedel oscillation in the density of bulk conduction electrons), but the range of all these interactions never exceeds a few atomic distances. The only exception is the special case of the indirect oscillatory electronic interaction mediated by a two-dimensional electron gas (2DEG). This type of interaction has been investigated here for the three systems Cu/Cu(111), Co/Cu(111) and Co/Ag(111), where a 2DEG is present in the form of the surface-states of the noble metal (111) surfaces. The interaction energy of isolated pairs of adatoms as a function of adatom distance has been determined from nearest neighbor distance distributions of the adatoms. The distributions are from series of STM images recorded at temperatures (10 K to 20 K) where the adatoms diffusion is sufficiently activated so that the adatoms probe the potential landscape in their surroundings but are not able to overcome the energy barrier for nucleation or trapping at steps. The comparison of the three adsorbate/substrate systems suggests the general existence of long-range oscillatory adsorbate interactions and shows up common characteristics. In all cases, the interaction energies manifest themselves up to more than 60 Å distance, they decay as  $1/r^2$ , and they oscillate with a period of half the surface-state Fermi wavelength. The data are in good agreement with theory and establish the link between the spatial variation of the interaction energy and the adatoms' scattering properties. Despite the fact that the observed interaction energies are small (in the meV range), they are expected to influence every adsorbate/substrate system with a two-dimensional electron gas present at the surface. The interaction can potentially be employed for the creation of new ordered atomic and molecular structures.

Turning to the second main topic of this thesis, low temperature scanning tunneling spectroscopy has emerged as an important local probe of the Kondo resonance of a

variety of Kondo systems due to its high spatial and spectroscopic resolution. The Kondo resonance of magnetic adsorbates on the noble metal surfaces invokes a sharp Fano line shaped resonance of the tunneling conduction at zero bias. The measurements presented here are about the strength and spatial decay of the Kondo resonance for Co on Cu(100) and on the three noble metal (111) surfaces of Cu, Ag and Au. They quantify the amount of direct tunneling into the LDOS of the magnetic 3d orbital and they show a scaling of the Kondo temperature with the number of nearest substrate atoms to the Co adatom. The analysis of the spatial decay of the amplitude of the Fano line shapes reveals that the Kondo resonance of Co is dominated by the bulk electrons and not the surface-state electrons. The coupling to the surface-state electrons of all three noble metal (111) surfaces is substantially enhanced by hydrogen adsorption to Co adsorbates. The resulting strong Kondo resonance of the 2D surface-state electron gas can be detected on Ag(111) up to distances of more than 100 Å away from the adatom site. This long-range behavior enables the direct determination of the energy dependence of the scattering phase shift at a single Kondo impurity showing the resonant energy dependence expected from Fermi liquid theory.

# Kurzfassung

Im Rahmen dieser Dissertation wurden mit einem Tieftemperatur-Rastertunnelmikroskop die Wechselwirkung von Adsorbaten mit den Leitungselektronen von Edelmetallen lokal untersucht: ein Thema der Arbeit ist eine indirekte, extrem langreichweitige Wechselwirkung zwischen Adsorbaten, die durch die Streuung von Oberflächenzustands-Elektronen an den Adsorbaten übertragen wird. Ein weiteres Thema ist die Korrelation von Leitungselektronen aufgrund der Wechselwirkung mit lokalisierten magnetischen Momenten von Adsorbaten, dem sogenannten Kondo-Effekt, mit besonderem Hinblick auf die räumliche Ausdehnung der Korrelation von Volumen-Elektronen im Vergleich zu Oberflächenzustands-Elektronen.

Die üblichen Adsorbat-Adsorbat Wechselwirkungen reichen nicht weiter als einige wenige atomare Abstände. Ausgenommen davon ist eine spezielle, indirekte Art der Wechselwirkung, die durch ein zwei-dimensionales Elektronengas übertragen wird. Diese langreichweitige Wechselwirkung wird hier an den drei Systemen Cu/Cu(111), Co/Cu(111) und Co/Ag(111) untersucht, wobei die Oberflächenzustände der dichtgepackten Edelmetall-Oberflächen eine gute Näherung an ein zwei-dimensionales Elektronengas bieten. Die Adsorbat-Adsorbat Wechselwirkungs-Energie als Funktion des Adsorbat-Adsorbat Abstandes  $r$  wurde statistisch über Nächste-Nachbar-Abstandsverteilungen quantifiziert. Die Abstandsverteilungen stammen von Serien von Rastertunnelmikroskop Topographien, aufgenommen bei Temperaturen zwischen 10 K und 20 K, bei denen die thermisch diffundierenden Adatome zwar hinreichend angeregt sind um das Potential ihrer Umgebung zu sondieren, aber nicht genug Energie haben um zu nukleieren. Der Vergleich der Wechselwirkungs-Energien der drei untersuchten Adsorbat/Substrat Systeme deckt die generellen Eigenschaften der Wechselwirkung auf: in allen drei Systemen manifestiert sich die Wechselwirkungs-Energie bis über 60 Å mit einem  $1/r^2$  Abfall und sie oszilliert mit einer Periode von der halben Fermi Wellenlänge der Oberflächenzustände. Die ermittelten Energien stimmen gut mit theoretischen Werten überein und schaffen eine Verbindung zu den Streueigenschaften der Adsorbate. Obwohl die hier untersuchten Wechselwirkung klein sind (im meV Bereich), beeinflussen

sie die Diffusion, die Nukleation und das Wachstum aller Adsorbat/Substrat Systeme mit einem zwei-dimensionalen Elektronengas an der Oberfläche und können vermutlich genutzt werden, um neuartige geordnete Strukturen von Atomen und Molekülen zu erzeugen.

Bestimmte Kombinationen von magnetischen Adsorbaten auf Metallen zeigen eine starke, lokale Korrelation der Leitungselektronen. Dieser sogenannten Kondo Effekt verursacht eine scharfe Fano-Resonanz der Tunnelleitfähigkeit für kleine Tunnelspannungen, wenn die Spitze des Rastertunnelmikroskop über einem Adsorbat platziert wird. In dieser Doktorarbeit wird das räumliche Verhalten der Kondo-Resonanz als Funktion des Adsorbat-Spitzen Abstandes  $r$  anhand der Systeme von Kobalt Adatomen auf Cu(100) und auf den (111) Flächen von Cu, Ag und Au untersucht. Die Messungen quantifizieren den Anteil des direkten Tunnelns in das 3d Orbital des Co Adatoms und die Abhängigkeit der Kondo Temperatur von der Anzahl der dem Co Adatom benachbarten Substrat-Atome. Der Vergleich des Abfalls der Amplitude der Resonanz als Funktion von  $r$  für Co/Cu(100) und Co/Cu(111) zeigt, dass die Kondo Resonanz des Co Atoms von Volumen-Elektronen dominiert wird. Die Kopplung zu den Oberflächen-Elektronen aller drei (111) Edelmetall-Oberflächen wird durch Wasserstoff Adsorption erheblich gestärkt. Die resultierende starke Kondo Resonanz des zwei-dimensionalen Elektronengases kann bis zu 100 Å Entfernung von dem Adsorbat detektiert werden. Diese Langreichweitigkeit ermöglicht eine direkte Vermessung der lokalen Zustandsdichte der stehenden Wellen der resonant gestreuten Oberflächen-Elektronen als Funktion der Energie. Die Energieabhängigkeit der Phasenverschiebung der gestreuten Wellen zeigt dabei ein resonantes Verhalten, wie es von der Theorie der Fermiflüssigkeit erwartet wird.

# Contents

<b>Abstract</b>	<b>i</b>
<b>Kurzfassung</b>	<b>iii</b>
<b>Abbreviations and Common Symbols</b>	<b>vii</b>
<b>0 Introduction</b>	<b>1</b>
<b>1 The Instrument</b>	<b>7</b>
1.1 The STM . . . . .	7
1.2 The UHV system and the cryostat . . . . .	9
1.3 Analysis and sample preparation tools . . . . .	11
<b>2 Theory</b>	<b>13</b>
2.1 The tunneling current . . . . .	13
2.2 2D scattering theory in polar coordinates . . . . .	16
2.3 Scattering resonance and Fano line shapes . . . . .	19
2.3.1 The non-interacting resonant level model . . . . .	21
2.3.2 The adsorbate LDOS . . . . .	22
2.3.3 The conduction band electron LDOS . . . . .	23
2.3.4 The tunneling conductance . . . . .	24
<b>3 The <math>s</math>-<math>p</math>-derived noble metal (111) surface states</b>	<b>25</b>
<b>4 Long-range adsorbate interactions mediated by a two-dimensional electron gas</b>	<b>31</b>
4.1 Thermal hopping rate of individual adsorbates . . . . .	31
4.1.1 The skyhook effect . . . . .	34
4.2 Surface-state mediated adsorbate interactions . . . . .	35
4.3 Long-range order . . . . .	42

4.4	Summary . . . . .	44
<b>5</b>	<b>Kondo resonance of single magnetic adsorbates on noble metal surfaces</b>	<b>47</b>
5.1	The Anderson model . . . . .	47
5.2	Kondo resonance of single Co adatoms on Cu surfaces . . . . .	51
5.3	Surface-state electron Kondo resonance . . . . .	56
5.4	Summary . . . . .	64
<b>6</b>	<b>Outlook</b>	<b>65</b>
	<b>Bibliography</b>	<b>69</b>
	<b>Acknowledgements</b>	<b>79</b>
	<b>Curriculum vitae</b>	<b>81</b>
	<b>Publications</b>	<b>83</b>

# Abbreviations and Common Symbols

2D, 3D	two, three dimensional
2DEG	two dimensional electron gas
fwhm	full width at half maximum/minimum
(L)DOS	(local) density of states
ML	Monolayer
RLM	Resonant Level Model
rms	root mean square
STM	Scanning Tunneling Microscopy
STS	Scanning Tunneling Spectroscopy
UHV	Ultra-High Vacuum
$A$	minimum to maximum amplitude of the Fano resonance
$c_a, c_k, c_a^\dagger, c_k^\dagger$	annihilation and creation ( $\dagger$ ) operators of adsorbate and conduction electron states
$d_{ta}$	tip-adsorbate distance
$(\delta_{bg}^l), \delta_l$	(background) phase shift of the $l$ th partial wave
$dI/dV$	tunneling conductance
$e$	elementary charge, $e = 1.60 \cdot 10^{-19}$ C
$E_a, E_F, E_T$	energy of discrete atom level, Fermi energy, surface-state band
$E_m$	onset energy, diffusion migration barrier
$\varepsilon$	$\varepsilon = (E - E_T)/(\Gamma/2)$



$\Gamma$	energy width of virtual bound state
$G_{aa}(E + i\eta)$	adsorbate projected Green's function
$G_c^0(E + i\eta)$	free conduction electron projected Green's function
$H_l^\pm(\varrho)$	Hankel function, $H_l^\pm(\varrho) = J_l(\varrho) \pm iN_l(\varrho)$
$\hbar$	Planck constant, $\hbar = \frac{h}{2\pi} = 1.05 \cdot 10^{-34}$ Js
$J$	exchange coupling constant
$J_l(\varrho)$	Bessel function, $J_l(\varrho) = \frac{H_l^+(\varrho) + H_l^-(\varrho)}{2}$
$k_B$	Boltzmann constant, $k_B = 1.38 \cdot 10^{-23} \frac{J}{K} = 0.0862 \frac{meV}{K}$
$k_F^s, k_F^b$	surface-state, bulk electron Fermi wave vector
$L_0$	surface-state electron density, $L_0 = \frac{m^*}{\pi \hbar^2}$
$\Lambda$	energy shift of resonance
$\lambda_F^s$	surface-state electron Fermi wavelength
$m_e$	electron mass, $m_e = 9.11 \cdot 10^{-31}$ kg
$m^*$	effective electron mass
$N_l(\varrho)$	Neumann function, $N_l(\varrho) = \frac{H_l^+(\varrho) - H_l^-(\varrho)}{2i}$
$n_0$	density of surface-state electrons
$n_a, n_k$	number operator of adsorbate, conduction electron level
$\nu(T), \nu_0$	hopping rate, attempt frequency
$\Phi_a, \Phi_t$	adsorbate, tip wave function
$q$	Fano line shape paramter
$r_{aa}, r_{ta}$	adsorbate-adsorbate, tip-adsorbate distance
$\rho_b, \rho_s, \rho_t$	bulk, surface-state, tip LDOS
$T, T_K$	sample and tip temperature, Kondo temperature
$T_{s,t}, T_{a,t}$	tunneling matrix elements
$t(E)$	$t$ matrix
$\tau$	lifetime, $\tau = \Gamma/\hbar$
$\Theta$	adsorbate coverage
$U$	Coulomb interaction energy
$V$	voltage between biased sample and virtually grounded tip
$V_{k,a}$	conduction electron - adsorbate hybridization matrix element
$x, y, z$	$x$ -, $y$ -coordinate (parallel to sample surface), and $z$ -coordinate (vertical to surface)
$\xi_K$	Kondo correlation length
$z_t$	vertical core to core tip-sample distance

# Chapter 0

## Introduction

Matter is made up of atoms. Proposed by ancient Greek philosophers, the existence of atoms was still under discussion a hundred years ago. Since then, much has been learned about them with experimental methods accessing their physical characteristics in a more and more direct way. Fundamental to the properties of matter be it an atom, a molecule or a macroscopic structure are the electronic states of the object. The electron cloud makes up the volume of the object and the electrons mediate the interactions, the chemical bonds, between the atoms. An unprecedented access to the local electronic properties of materials on the atomic scale is offered by Scanning Tunneling Microscopy (STM), invented by Binnig and Rohrer in 1982 [1, 2]. The power of the tunneling microscope lies in its ability to spatially and energetically resolve the electronic states on a conducting surface. Spatially, the states can be observed with atomic resolution. Energetically, states which lie within a few electron-volts on either side of the Fermi level can be observed with an energy resolution of a few  $k_B T$ . Besides its investigational possibilities, the STM has been used for the engineering of atom sized structures by controlled moving and picking up of single atoms and molecules on metal surfaces [3–6]. The development of the scanning tunneling microscope together with other scanning techniques like the Atomic Force Microscope has been crucial to the rapid progress in the understanding and engineering of atom sized structures, which has become a highly funded interdisciplinary movement referred to as nanoscience.

The principle of the STM is beautifully simple: it's an electric circuit made up of a voltage source, the tunneling bias, applied to a tunable resistance, the tunneling resistance, which is determined by the size of the vacuum- (or gas-, liquid-) gap between the two electrodes of the STM. One electrode is tip shaped, i.e. microscopic, and can be positioned relative to the second electrode, which is the sample under study. If the gap is small enough such that electrons are able to cross (tunnel) the gap due to their

quantum mechanical wave character, a tunneling current flows. The current's strength increases exponentially on the overlap of the tip's apex wave function with the wave function of the substrate. Due to this sensitivity on the tip-probe distance, a highly spatially resolved information of the studied object is achieved by scanning the tip and measuring the tunneling current. Furthermore, the amount of current flowing for a given potential difference depends also on the electron energy levels available, i.e. on the local density of electronic states (LDOS) at the tip and the opponent object, and thus contains valuable spectroscopic information about the probe. In many cases, the LDOS can be determined by measuring the tunneling conductance signal, a method called scanning tunneling spectroscopy (STS). The technological problems to master for the operation of a STM have been the high precision needed in the placement of the tip, the stabilization of the tunneling gap, the measurement of the small noisy tunneling currents and the data collection, which powerful computers arrived just in time for.

An important step for the investigation of single adatoms was the development of scanning tunneling microscopes running at cryogenic temperature [7]. Not only can different physical phenomena like superconductivity be studied at low temperature, but also the quality and reproducibility of the measured tunneling current is enhanced: thermal noise in the current is small, thermal drifts of the piezo ceramics that move the tunneling tip are reduced, and probably most important, unwanted adsorbates at the tip and the surface are frozen so that they don't diffuse into the tunneling region and thereby disturb the tunneling current. All these points combined have made possible measurements like the mapping of the Abrikosov flux lattice at the surface of the superconducting NbSe<sub>2</sub> [8] or the  $\approx 10$  meV Kondo resonance of a single magnetic adatom [9, 10], which is a topic addressed in the present thesis. At cryogenic temperatures in an UHV, a single adatom can be observed for several days because it does not diffuse and is not contaminated by other adsorbates

In recent years new developments in condensed-matter physics came from two-dimensional (2D) electron systems like the quantum Hall effects and high-temperature superconductivity. For the effects studied here, the fact that local interactions are less effectively screened in two than in three dimensions is exploited. A good approach to a two-dimensional electron gas are so called surface-states, present for example on the noble metal (111) surfaces. Bulk forbidden electronic surface-states may arise at a crystal surface because of the breaking of the translational symmetry perpendicular to the surface [11, 12]. An electron in a surface-state is confined to the first few layers at the crystal surface, but can move freely parallel to it. Starting in 1991 with the work by Davis *et al.* [13], STM has frequently been used to investigate noble metal surface-states

[14–33]. Surface-state electrons contribute strongly to the tunneling current because of their high density at the surface and thus Fermi wavelengths are long enough to be easily resolved by STM driven in the spectroscopic mode. These two features allow for a fascinating insight into the wave nature of electrons: For example, the standing wave solutions of an electron in a potential well, a problem known to every student of quantum physics, can be directly mapped by STM by measuring the density of surface-state electrons trapped on small atomically flat terraces [26] or artificial corrals build by STM atom manipulation [14].

In this thesis, the unique possibilities of a cryogenic STM have been used to study aspects of the interaction of bulk conduction band and surface-state electrons with adsorbates on noble metal surfaces: one topic is the long-range lateral interaction between adsorbates mediated by a 2D electron gas, another the correlation of conduction electrons due to scattering at magnetic adsorbates, called Kondo effect, with special interest in the spatial extent of the correlation for 2D and 3D conduction electrons.

Turning to the first main topic of this thesis, lateral interactions between adsorbed species have a determining influence on heterogeneous catalysis, molecular self-assembly, and thin-film epitaxy. The usually considered interactions like the direct electronic interaction and the indirect electrostatic (dipole-dipole), elastic (deformation of substrate lattice), and electronic (bulk conduction electrons) interactions have amply been studied in the past and lead to complicated behavior with high chemical specificity and a range never exceeding a few atomic distances. For their investigation, STM has emerged as a quantitative tool [34–37], supplementing the well established field ion microscopy method [38–41]. However, for more than 20 years there has been the theoretical prediction that there should exist oscillatory adsorbate interactions of extremely long range, mediated by screening in a 2D electron gas [42]. The adsorbates interact indirectly via oscillations in the substrate electron density, due to scattering of conduction band electrons by the adsorbates. For a 2D electron gas, such an interaction for a pair of adsorbates falls off with the square of the distance  $1/r^2$  between two adsorbates, compared to  $1/r^5$  for a 3d electron gas. First qualitative indication of long-range interactions came from equidistant bulk segregated impurities on Cu(111) [43], first experiments quantifying such interactions mediated by surface-state electrons for Cu adatoms on Cu(111) were recently reported by Repp *et al.* [44] and by the work of this thesis [45,46], where in addition Co on Cu(111) and Co on Ag(111) have been investigated. The comparison of the three adsorbate/substrate systems suggests the general existence of long-range oscillatory interactions and shows common characteristics. In all cases, the interaction energy  $E(r)$  manifests itself up to more than 60 Å distance, it decays as  $1/r^2$ , and

oscillates with a period of half the surface-state Fermi wavelength. The data are in good agreement with theory and establish the link between the spatial variation of the interaction energy and the adsorbates' scattering properties.

In the following, the reader is introduced to the second main topic of this thesis, the Kondo resonance of single magnetic adsorbates on noble metal surfaces. In the 1930s, it was observed that some metals have a shallow resistance minimum at low temperatures ( $\approx 10$  K). Usually, the resistance of a metal drops monotonic as its temperature is lowered because of decreasing electron-phonon interactions until it saturates due to scattering at static defects in the material. The resistance minimum puzzled physicists until it was realized that the strength of the minimum was related to the concentration of magnetic impurities in the metal such as cobalt atoms. A first explanation of the phenomena was given by Jun Kondo in 1964 [47]: Impurities that keep their magnetic moment in the metal host have an internal spin degree of freedom that alters their scattering properties qualitatively compared to non-magnetic lattice imperfections. Considering the scattering from a magnetic ion that interacts with spins of the conduction electrons, Kondo found that higher order perturbation terms could be dominant resulting in a logarithmically increasing resistance with falling temperature. Kondo's perturbation approach correctly describes the resistance for temperatures above the Kondo temperature  $T_K$ , but makes the unphysical prediction that the resistance diverges as  $T$  approaches 0 K. The search for a more comprehensive theory became known as the Kondo problem [48]. Today, it is understood that the interaction of the localized  $d$ - or  $f$ -electrons of the magnetic impurity with the delocalized conduction electrons generate a correlated non-magnetic singlet ground state of the host and impurity electrons with the same energy as the Fermi level. This state manifests itself in a sharp resonance of the quasi particle density of states of width of order of  $k_B T_K$  at the Fermi energy, which explains the increase of the resistance, i.e. the increased scattering of conduction band electrons, with decreasing temperature. The resistance minimum together with other phenomena like the complete screening of the magnetic moment of the impurity at 0 K are collectively referred to as the Kondo effect.

Recently, the unprecedented control over Kondo systems [9, 10, 46, 49–73] provided by new experimental techniques from the rapidly developing field of nanotechnology has rekindled interest in the Kondo effect [74] starting in 1998, when the Kondo resonance of single magnetic adatoms were locally studied by STS [9, 10] and the Kondo resonance in an artificial quantum dot was observed [60, 61]. Quantum dots made for the study of the Kondo effect [60–70] are small ( $\approx 0.1 \mu\text{m}^2$ ) puddles of charge containing a well-defined number ( $\approx 100$ ) of electrons. They are typically fabricated by putting metallic

gates on a semiconductor region that behaves as a two-dimensional electron gas. If an odd number of electrons is trapped within the dot, the localized spin, embedded between large conductance electron seas in the two leads, mimics the magnetic impurity in a metal system. In contrast to increasing the resistance in a metal by increasing the scattering of the conduction electrons, the Kondo resonance increases the conductance of the quantum dot by coherently superposing the localized states on the quantum dot and the delocalized states in the two opposite electrodes, until the conductance reaches the unitary limit of  $2e^2/h$  which implies that the electrons are transmitted perfectly through the dot [65]. Low temperature STM has emerged as an important local probe of the Kondo resonance of a variety of Kondo systems due to its high spatial and spectroscopic resolution [9,10,46,49–59]. On noble metal surfaces, the Kondo resonance of magnetic adsorbates typically invokes a sharp antiresonance of the tunneling conduction at zero bias due to dominant tunneling into the perturbed conduction electron LDOS (and not into the LDOS of the magnetic orbital). The measurements presented here are about the strength and spatial decay of the Kondo resonance for Co on Cu(100) and on the three noble metal (111) surfaces of Cu, Ag and Au. They quantify the amount of direct tunneling into the LDOS of the magnetic orbital and they show a scaling of the Kondo temperature with the number of nearest substrate atoms to the Co adatom. It is further shown, that the surface-state electrons are essentially not involved in the Kondo resonance for Co adatoms. This is changed by adsorption of hydrogen to the cobalt, leading to a very long range Kondo effect, making the direct observation of the phase shift of the scattered surface-state electrons possible.

The following is a short summary of the thesis. Chapter 1 describes the setup and functionality of the low temperature STM system. In Chapter 2, some theoretical points important to STM studies of adsorbate – conduction band electron interactions are introduced: approximate expressions for the tunneling current, the relation of the tunneling conductance to the surface LDOS, 2D scattering formulas, and Fano line shapes derived from the resonant level model. Chapter 3 introduces the noble metal (111) surface-states to the reader, their characteristics and their accessibility by STM.

In Chapter 4, lateral long-range interactions between adsorbates on metal surfaces with a surface-state are investigated. The chapter begins with the investigation of the thermal hopping rate of isolated adsorbates in Section 4.1 in order to determine the corrugation of a single adsorbate's potential energy surface as well as to find the temperature range where the interaction is observable. In the main Section 4.2, the interaction energy of isolated pairs of adsorbates as a function of adsorbate distance is determined from the nearest neighbor distance distribution of adsorbates. The distri-

butions are determined from series of STM images recorded at temperatures (10 K to 20 K) where the adsorbate diffusion is sufficiently activated so that the adsorbates probe the potential in their surroundings *but are not able to overcome the energy barrier for* nucleation or trapping at steps. In the last Section 4.3, the potential of the interaction to create a long-range order between adsorbates is investigated.

Chapter 5 is about local scanning tunneling spectroscopy investigations of the Kondo resonance of single magnetic adsorbates on noble metal surfaces. After a theoretical introduction to the Kondo effect in Section 5.1, where it is shown that the Kondo effect of a magnetic adsorbate manifests itself as a Fano resonance at zero bias in the tunneling conductance, the Kondo resonances of Co adatoms on Cu(100) and Cu(111) are quantitatively compared in Section 5.2: the higher Kondo temperature  $T_K$  of Co/Cu(100) is ascribed to the scaling of  $T_K$  with the number of nearest substrate Cu atoms. While at the Cu(100) surface both, tunneling into the hybridized localized state and into the substrate conduction band contribute to the Kondo resonance, the latter channel is found to be dominant for Cu(111). The analysis of the spatial decay of the amplitude of the Fano line shapes reveals that the Kondo resonance is dominated by the Cu bulk electrons. In Section 5.3 it is shown that the coupling to the surface-state electrons of all three noble metal (111) surfaces is substantially enhanced by hydrogen adsorption to Co adsorbates. The resulting strong Kondo resonance of the 2D surface-state electron gas can be detected on Ag(111) up to distances of more than 100 Å away from the adatom site. This long-range behavior enables the direct determination of the energy dependence of the scattering phase shift at a single Kondo impurity showing the resonant energy dependence expected from Fermi liquid theory. Finally, Chapter 6 gives an outlook on the possible impact and implementations of the effects studied in this thesis.

# Chapter 1

## The Instrument

### 1.1 The STM

All measurements presented in this thesis have been performed with a home built  $^4\text{He}$  bath cooled STM working in UHV. It has a high spatial stability ( $\approx 0.5$  nm in the vertical direction) and a spectroscopic energy resolution better than 1 mV. The instrument was completed in 1998 at the École Polytechnique Fédérale in Lausanne [75, 76]; the UHV chamber has been redesigned on the occasion of a move of the group to the Max-Planck-Institute in Stuttgart in the year 2000.

The STM is of the beetle type [77] (Fig. 1.1). It is placed in a cylindrical copper pot for thermal isolation and good thermal coupling to the cryostat. The tip is attached to the scan piezo pointing down towards the sample. The sample is placed at the center of a sample holder which can be inserted with a wobble stick into a horizontal slit in the STM body underneath the tip. The sample holder is pressed upwards against a polished surface of the STM body by three spring-loaded Teflon plugs to fix the tip-sample distance and to guarantee a good thermal contact to the STM body.

The scan piezo is a hollow cylindrical piezo ceramic with five concentric vapor deposited electrodes covering most of the outer piezo surface and a grounded electrode covering the inner surface. The four electrode segments for the  $x$ - $y$ -scanning movement are located at the upper half of the piezo, the electrode for the vertical  $z$ -movement covers the lower part of the scan piezo. By applying high voltages ( $\pm 200$  V) to the outer electrodes, the piezo tube can be bent, stretched and compressed thereby placing the tip at a desired position or scanning it across the sample surface. An area of  $\approx 1 \mu\text{m}^2$  can be reached and the tip can be vertically moved by about 200 nm.

Because the scan piezo can be retracted only nanoscopically, a coarse approach mechanism is needed to avoid tip crashes during sample transfer: The scanning piezo



is attached to a molybdenum disk which has three helical ramps at its boarder with a height difference of 0.5 mm. The disk resides with its ramps on three ruby balls at the end of three piezo legs. Those stand upward and are glued to the STM body at their bottom. If the three piezos are controlled in the right way, the molybdenum disk can be turned in both directions by a “stick and slip” movement thereby moving the tip up and down via the helical ramps. Also, this technique allows for a macroscopic lateral mm-scale displacement of the tip which is very useful when looking for particularly clean areas of the sample, large atomic terraces, variation in adsorbate coverage or moving away from scratches.

The tip is a ca. 1 cm long 0.2 mm thick polycrystalline tungsten wire (99% pure) sharpened by chemically etching. The tip apex is cleaned in-situ by field-emission by applying a voltage of  $-600$  V to the tip and decreasing the tip-sample distance until a current of about  $200\text{ }\mu\text{A}$  is flowing. The high current density removes dirt from the tip apex by heating it up. During operation of the STM, smaller dirt particles are removed by dipping the tip several nanometers into the clean sample.

The STM is usually driven in two distinct modes, the topographic constant current mode and the spectroscopic mode. In the constant current mode, the tunneling current is compared to a preset current value and the difference is fed back to the voltage applied to the  $z$ -piezo so that the tip-sample distance is adjusted to minimize the difference of the measured and the preset current. During scanning of the surface with the tip, the voltage applied to the  $z$ -piezo in order to keep the current constant is recorded by a computer and assembled to a topographic image of the surface. In the spectroscopic mode, called scanning tunneling spectroscopy (STS), the differential tunneling conductance as a function of the bias voltage is recorded for a fixed tip position. This is done by opening the feed-back loop and ramping the bias voltage over the desired range. The differential conductance is derived from the tunneling current by standard lock-in technique with a high frequency modulation of  $\approx 4$  kHz to the bias voltage, which is well above the bandwidth of the feedback loop. Thus the  $z$ -piezo does not follow the modulation of the bias voltage.

All the basic functions of the STM like the feedback loop or the coarse approach are handled by a commercial electronics from RHK (STM 200 Control Electronics). The user interacts with the electronics via a graphical user interface (STMCPs) running on a Silicon Graphics Iris Workstation, which communicates with the electronics by an ethernet.

The STM was designed for a spectroscopic energy resolution better than 1 mV, limited by the operating temperature of the STM of  $\approx 6$  K. Thus grounding was done

very carefully and all signal lines to the microscope (bias voltage to the sample, all piezos connections, tunneling current from the tip) are filtered with radio frequency filters on top of the cryostat. The current is pre-amplified on top of the cryostat with  $10^7$  V/A gain, post-amplified alternatively with 1, 10, or 100 gain and can be additionally low-pass filtered with 10 to 0.3 kHz bandwidth. The bias voltage supplied by the RHK is also low-pass filtered with optional 3 k, 1 k, 100 or 10 Hz bandwidth and can be divided by 1 to 100 to fit the voltage range of interest to the bit resolution of the DA converter of the RHK electronics ( $\pm 10$  V, 12 bits).

## 1.2 The UHV system and the cryostat

The UHV system is constructed along two major axes, one vertical axis given by the cylinder of the longish cryostat (Oxford Instruments) and the STM, and a horizontal axis given by the STM at one side and the sample manipulator on the other side (Fig. 1.1). The cryostat is made up of two nested hollow-cylinder dewars, the inner for liquid helium (42 l) thermally shielded by the outer dewar for liquid nitrogen (25 l). The dewars are separated from each other and from the outside by the systems common vacuum. The STM is located at the lower end of the cryostat in the center of a superconducting split-pair magnet providing a magnetic field vertical to the sample surface of up to 5 T. For good thermal anchoring of the STM to the cryostat, a copper cone at the top of the STM body is pressed against its counterpart in the cryostat by a spring in the transfer rod. The rod is thermally anchored to the LN<sub>2</sub> dewar at the top to reduce the thermal flux to the STM. All signal lines to the microscope run along the rod.

Horizontally, the system is cut in two halves by a plate-valve in its center, separating the preparation chamber from the cryogenic chamber. Closing the central valve makes cleaning and preparation of the samples possible during low temperature operation of the STM without adsorbing dirt and sputter gas to all cooled surfaces. The sample can be moved on the manipulator from different preparation and analyzing stations within the preparation chamber across the central valve into the cryogenic chamber, where it can be picked up by a wobble-stick and transferred into the STM or put into a sample storage with room for two samples.

The whole system is encapsulated in a sound insulation cubicle damping acoustic noise by  $\approx 20$  dB to stabilize the tunneling gap. Additionally, three vibration isolation stages damp the low frequency vibrations coming from the ground: the system is mounted on an optical honeyweb table residing on four active dampers (HWL Bioanalytics/JRS) operating in the frequency region 1 – 40 Hz. A frame supporting the system

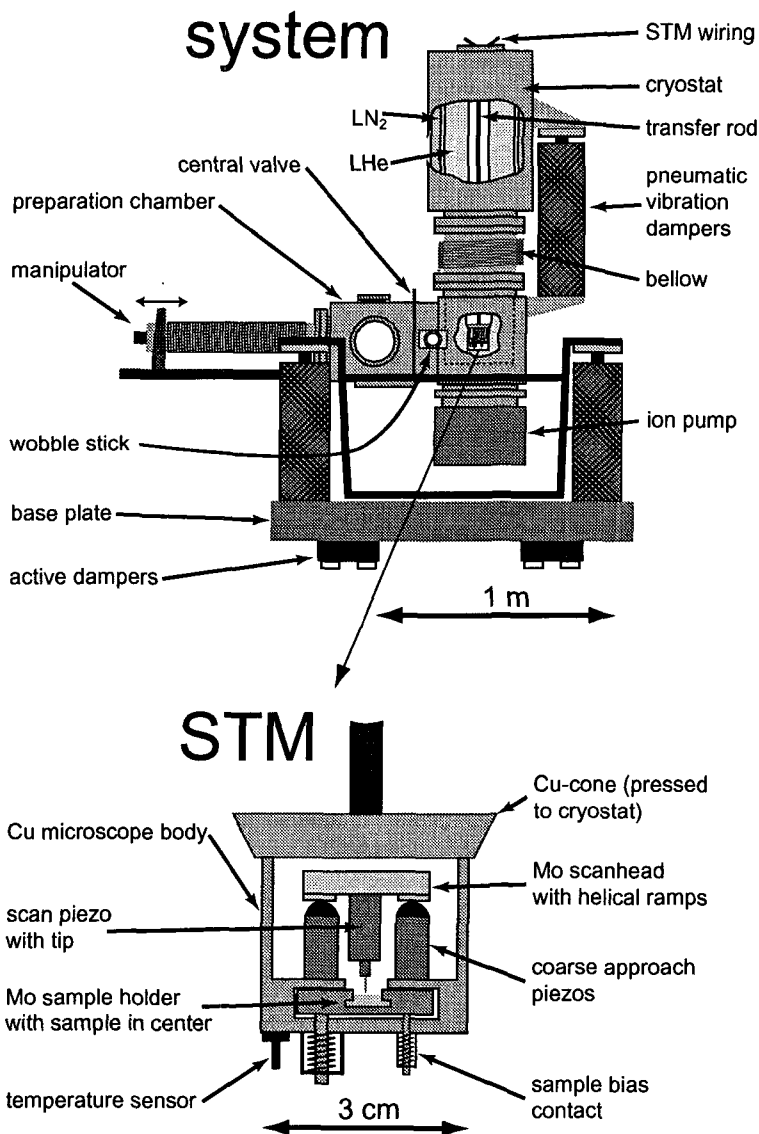


**Figure 1.1:** Sketch of the UHV-chamber and the scanning tunneling microscope.

stands on four passive pneumatic dampers (Newport). The last damping stage is made up of three pneumatic dampers (Newport) decoupling the cryostat from the rest of the system. A flexible bellow connects the two parts to retain the common vacuum. Since the STM is firmly connected to the cryostat without a vibration isolation in between to guarantee good thermal anchoring, vibrations coming from gas bubbles due to the evaporation of liquid nitrogen have to be suppressed during measurements by pumping the LN<sub>2</sub> dewar which solidifies the N<sub>2</sub>.

An ultra high vacuum (UHV) with a base pressure in the upper 10<sup>-11</sup> mbar region is sustained in the system by several pumps. The preparation chamber is pumped by a turbomolecular pump and an ion pump, the cryogenic chamber by an ion pump at the bottom of the system, a titanium sublimation pump and, if filled with liquid helium, by the cryostat itself.

## 1.3 Analysis and sample preparation tools

In the preparation chamber, standard UHV preparation and analysis tools are concentrically arranged around the sample transfer axis: a load-lock for sample insertion without destruction of the UHV, a differentially pumped sputter gun (IQE 12/38 from SPECS), two electron beam evaporators (EFM from Omicron), an Auger spectrometer with cylindrical mirror analyzer (CMA 150 from Omicron), a mass-spectrometer (TSP TH100 from Leybold) and a vacuum gauge.

The experiments described here have been performed on noble metal single crystals supplied by MaTeck precisely cut and polished in the (111) and (100) plane with an orientational misfit smaller than 0.1°. The hat shaped samples, Au(111), Ag(111), Cu(111), and Cu(100), with a circular upper surface of 7 mm in diameter and a total thickness of 3 mm are clamped into the sample holder (Fig. 1.1). Before measurements, the surfaces of the samples are cleaned from contaminations like oxide layers and water by sequential cycles of Ar<sup>+</sup> sputtering at room temperature and subsequent annealing to ≈800 K. The rather inert noble metal surfaces can be cleaned very efficient to impurity coverages of less than 10<sup>-4</sup> monolayers and they stay clean in the UHV for several days. Due to the small miscut of the samples, atomically flat terraces larger than 200 nm in width can be easily found.

Low coverages of adatoms are deposited directly onto the cold sample surface with a current heated line-of-sight filament evaporator located inside the cryogenic chamber. Thin wires ( $\varnothing = 0.1$  mm) of high purity (99.996%) of the metal to be evaporated are wired around a supporting tungsten filament ( $\varnothing = 0.25$  mm). The filament-sample

distance is 18 cm, the angle of incidence of the adatoms onto the sample is  $10^\circ$ . The evaporated atoms access the sample only by passing small holes in the helium dewar and the STM body. This way, the heat radiation on the sample during evaporation is reduced and the pressure stays in the  $10^{-10}$  mbar region.

A sample temperature of 5.6 K as measured by a temperature sensor (Cernox) replacing the sample is reached when inserting a copper plug into the sample transfer hole of the cryostat to block heat radiation. The sample temperature can be precisely varied by evaporating the liquid helium in the cryostat. After all the liquid He is gone, the temperature slowly rises by about 1 K every two hours enabling a precise temperature determination. During measurements, the sample temperature is measured by a sensor at the bottom of the STM body. Temperatures of this sensor are calibrated to temperatures which have been determined once by the sensor replacing the sample. The calibration is necessary because the bottom of the STM is slightly colder than the sample by about 1 K, or 5 K without inserted copper plug, due to residual heat radiation and heat flux to the sample.

## Chapter 2

### Theory

#### 2.1 The tunneling current

The amplitude of the wave function of an electron bound to a substance like a metal does not end abruptly at the surface of the metal but decays exponentially into the vacuum. This is a consequence of the wave nature of matter similar to the evanescent wave of totally reflected light in optics. The exponential decay of the vacuum tail of the wave function follows from the Schrödinger equation for a free particle with negative energy. When a second metal is brought very close, the tail of the electron's wave function reaches into the second metal giving rise to a finite transition probability of the electron to the second metal. This transition across a classically energetically forbidden region is known as the tunneling effect. Upon applying a potential difference between the two metals, a net tunneling current flows. In STM, the two electrodes are the tip and the

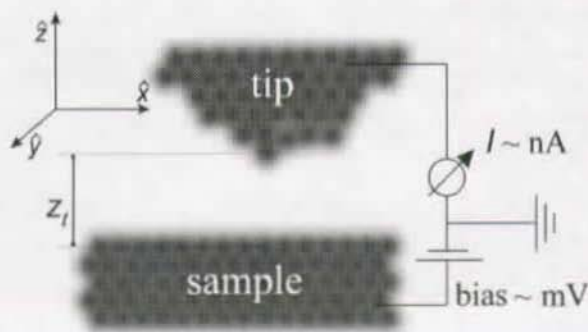


**Figure 2.1:** Electric circuit of the tunneling current. The sample is biased by the potential  $V$  with respect to ground. Typical tip-sample (core-to-core) distances  $z_t$  are 5 Å–10 Å.

sample (Fig. 2.1). Because of the exponential dependence of the tunneling current on the tip-sample distance, the current flows highly localized through the few atoms at the apex of the tip basically causing the high spatial resolution of the STM. An expression for the tunneling current  $I$  may be determined by time-dependent perturbation theory using Fermis golden rule [78–82]:

$$I(V) = 2e \sum_{s,t} \frac{2\pi}{\hbar} |T_{s,t}|^2 \delta(E_s - eV - E_t) \times \\ \left( f(E_s - eV, T) [1 - f(E_t, T)] - f(E_t, T) [1 - f(E_s - eV, T)] \right), \quad (2.1)$$

where the summation goes over all unperturbed quantum levels of the sample  $s$  with energy  $E_s$  and of the tip  $t$  with energy  $E_t$ <sup>1</sup>.  $T$  is the temperature of sample and tip,  $V$  is the voltage between the biased sample and the virtually grounded tip. The Fermi-Dirac distributions  $f$  make sure that only tunneling from occupied to unoccupied electron levels occurs, for positively biased sample from the tip to the sample (2. term of Eq.(2.1)) and vice versa (1. term of Eq.(2.1)). The delta function  $\delta$  assures that the energy of the tunneling electrons is conserved, i.e. elastic tunneling is described. The probability of transition from level  $t$  to level  $s$  is given by the tunneling matrix element

$$T_{s,t} = -\frac{\hbar^2}{2m_e} \int_{\Sigma} dS (\Psi_t^* \nabla \Psi_s - \Psi_s \nabla \Psi_t^*), \quad (2.2)$$

with the wave functions of the unperturbed sample  $\Psi_s$  and tip  $\Psi_t$  levels and the integral running over an arbitrary surface  $\Sigma$  within the tunneling barrier region.  $T_{s,t}$  depends on the overlap of the two wave functions, i.e. roughly exponential on the barrier width  $z_t$  as well as on the electron momentum perpendicular to the surface.

A common approximation in STM theory for Eq. (2.1) is the  $s$ -wave approximation for the tip wave function introduced by Tersoff and Hamann [83–85]. The tunneling current is given by an energy integration over the products of an electron supply function, an electron reception function and a transmission probability (Fig. 2.2):

$$I(V, T, x_t, y_t, z_t) \propto \int_{-\infty}^{\infty} dE \rho_s(E, x_t, y_t) \rho_t(E - eV) \times \\ \mathcal{T}(E, V, z_t) [f(E - eV, T) - f(E, T)], \quad (2.3)$$

where  $z_t$  is the distance between tip and sample measured between the virtual planes passing through the uppermost atoms of tip and the sample (Fig. 2.1),

<sup>1</sup>Throughout this thesis, the convention is adopted that the energies are measured with respect to the respective Fermi levels of the substrate and tip





mode, the  $z$  dependence is used to compose topographs of the sample surface. The term topograph is misleading in the sense that not the positions of the atomic nuclei are imaged but rather a surface of constant LDOS (in the topograph of Fig. 3.1 for example, the oscillations in the LDOS around the adsorbates and steps have an apparent elevation of the same order of magnitude as the topographic heights of the adsorbates).

In scanning tunneling spectroscopy (STS), the sample LDOS as a function of energy is derived from the voltage dependence of the tunneling conductance  $dI(V)/dV$ . For low bias voltages  $|V| \ll \hbar\sqrt{2W_t}/z_t\sqrt{m_e}$  it can be shown from Eq. (2.1) that the tunneling conductance is a function of the sample LDOS times the tip LDOS [86]. Usually, one is interested in the sample LDOS only, i.e. the sample LDOS has to be isolated from the generally unknown tip LDOS in the tunneling conductance. If the tip LDOS is flat over the energy range of interest, the  $dI/dV$  signal is directly proportional to the LDOS of the sample as can be seen from Eq. (2.6). Before taking spectra, the tip LDOS is modified by gently dipping the tip into the sample (1 nm) until the background spectra are as flat as possible in the energy range of interest. The background spectra are taken far away from any adsorbates and other objects like impurities and atomic steps, so that the sample LDOS is unstructured. If it is not possible to flatten the tip LDOS, the sample LDOS can be determined by numerically unfolding the  $dI/dV$  spectrum from a background spectrum.

Compared to other spectroscopic surface analysis tools like photo-emission spectroscopy, STS has the advantage of local probing with high spatial resolution, high energy resolution and direct access to the two sides of the Fermi edge, i.e. for positive sample bias the hole-states of the sample above the Fermi energy are probed, for negative sample bias the occupied sample states below the Fermi energy are probed. Disadvantages are that states far from the Fermi level with low tip overlap are not resolved and that the unknown tip LDOS is always folded into the spectra [86].

## 2.2 2D scattering theory in polar coordinates

As we will see, many aspects of the interaction of surface-state electrons with adsorbates can be well described by scattering theory because the adsorbates are small compared to the relevant wave lengths of the surface-state electrons. The time-independent 2D Schrödinger equation in polar coordinates for a particle of mass  $m$  and energy  $E$  in a potential  $V(r, \varphi)$  reads:

$$\left[ -\frac{\hbar^2}{2m} \frac{1}{r} \frac{\partial}{\partial r} \left( r \frac{\partial}{\partial r} \right) + \frac{1}{2mr^2} \left( -\hbar^2 \frac{\partial^2}{\partial \varphi^2} \right) + V(r, \varphi) \right] \Psi(r, \varphi) = E \Psi(r, \varphi). \quad (2.7)$$

The probability of finding the particle at  $(r_0, \varphi_0)$  in the infinitesimal area  $r_0 dr d\varphi$  is given by  $r_0 |\Psi(r_0, \varphi_0)|^2 dr d\varphi$ . For a central potential  $V(r)$ , the Schrödinger equation can be solved by a separation Ansatz

$$\Psi(r, \varphi) := R(r)\Phi(\varphi). \quad (2.8)$$

With a separation constant  $l^2$ , the normalized solution to the azimuthal equation  $\frac{\partial^2}{\partial \varphi^2} \Phi_l(\varphi) = -l^2 \Phi_l(\varphi)$  is

$$\Phi_l(\varphi) = \frac{1}{\sqrt{2\pi}} e^{il\varphi}, \quad (2.9)$$

where the angular momentum quantum number  $l$  has to be integer,  $l \in \{0, \pm 1, \pm 2, \dots\}$ , to guarantee uniqueness of the wave function. The radial equation can be transformed to

$$\left[ \frac{\partial^2}{\partial \varrho^2} + \frac{1}{\varrho} \frac{\partial}{\partial \varrho} + (\varrho^2 - l^2) - \frac{2m}{\hbar^2} V(r) \right] R_{k,l}(r) = 0, \quad (2.10)$$

where  $\varrho = kr$  and  $E = \hbar^2 k^2 / 2m$ . For a free particle with  $V(r) = 0$ , the radial equation reduces to the Bessel equation, which has the linearly independent solutions  $J_l(\varrho)$ , the Bessel functions of the first kind, or simply Bessel functions, and  $N_l(\varrho)$ , referred to as the Bessel functions of the second kind, Neumann functions, or Weber functions. The linear combinations  $H_l^\pm(\varrho) = J_l(\varrho) \pm iN_l(\varrho)$ , called Hankel functions or Bessel functions of the third kind are in the asymptotical limit outgoing ( $H_l^+(\varrho)$ ) and incoming ( $H_l^-(\varrho)$ ) circular waves:

$$H_l^\pm(\varrho) \xrightarrow{kr \rightarrow \infty} \sqrt{\frac{2}{\pi}} \frac{e^{\pm i(\varrho - \frac{l\pi}{2} - \frac{\pi}{4})}}{\sqrt{\varrho}}. \quad (2.11)$$

The general solutions of Eq. (2.10) for  $V(r) = 0$  and positive energy  $E$  can be written as  $R_{k,l}^{(0)}(r) = c^- H_l^-(\varrho) + c^+ e^{i2\delta_l} H_l^+(\varrho)$  (times an overall phase factor). For zero absorption  $c^- = c^+ = c$  because the incoming and the outgoing probability flux have to be the same and  $\delta_l = 0$  because  $R_{k,l}^{(0)}(r) \rightarrow \infty$  as  $\varrho \rightarrow 0$  for  $\delta_l \neq 0$ . Therefore the general solutions to Eq. (2.7) for  $V(r) = 0$  and positive  $E$ , the free circular wave functions are

$$\Psi_{k,l}^{(0)}(r, \varphi) = \sqrt{\frac{k}{2\pi}} J_l(kr) e^{il\varphi}, \quad (2.12)$$

with  $J_l(\varrho) = (H_l^-(\varrho) + H_l^+(\varrho))/2$  and  $c = k$  from normalization in the extended sense:  $\langle \Psi_{k,l}^{(0)} | \Psi_{k',l'}^{(0)} \rangle = \delta(k - k') \delta_{ll'}$ . It can be seen from Eq. (2.11) that the probability per unit area of finding a free particle in the state  $\Psi_{k,l}^{(0)}(r, \varphi)$  falls off asymptotically as  $1/r$ . In comparison, in 3D space, the free spherical waves are [87]:

$$\Upsilon_{k,l,m}^{(0)}(r, \varphi, \vartheta) = \sqrt{\frac{2k^2}{\pi}} j_l(kr) Y_l^m(\varphi, \vartheta), \quad (2.13)$$

with the spherical Bessel functions  $j_l(kr) = \sqrt{\pi/(2kr)} J_{l+1/2}(kr)$  and the spherical harmonics  $Y_l^m(\varphi, \vartheta)$ . The probability per volume of finding a free particle in the state  $\Upsilon_{k,l,m}^{(0)}(r, \varphi, \vartheta)$  falls off asymptotically as  $1/r^2$  since  $j_0(kr) = \sin(kr)/(kr)$ . This more rapid decay in three dimensions, which assures particle conservation, is of purely geometrical nature.

For a localized potential  $V(r, \varphi)$  that vanishes for  $r \rightarrow \infty$ , the Hankel functions are asymptotic solutions to the radial equation Eq. (2.10). The general solutions  $\Psi_{k,l}$  still have to guarantee particle conservations ( $c^- = c^+$ ), but the  $\delta_l$  are not zero: their values are determined by imposing continuity between the asymptotic solution

$$\Psi_{k,l}(r, \varphi) \underset{kr \rightarrow \infty}{\propto} \Phi_l(\varphi) \frac{e^{-ikr} e^{i(\frac{l\pi}{2} + \frac{\pi}{4})} + e^{ikr} e^{-i(\frac{l\pi}{2} + \frac{\pi}{4})} e^{2i\delta_l}}{\sqrt{2kr}} \quad (2.14)$$

and the full radial equation Eq. (2.10). The quantity  $\delta_l$  defined this way is called the phase shift of the partial wave  $\Psi_{k,l}(r, \varphi)$ . This expression can be explained in the following way: as the incoming circular wave of a particle with energy  $E$  and angular momentum  $l$  approaches the zone of influence of the potential, it is more and more perturbed by the potential. When, after turning back, it is transformed into an outgoing circular wave, it has accumulated a phase shift of  $2\delta_l$  relative to the free outgoing wave for a zero potential.

If absorption occurs, the amplitude of the outgoing wave will be reduced. This is described mathematically by a complex phase shift  $\eta_l = \delta_l + i\alpha_l$  with the factor  $e^{2i\eta_l} = e^{-2\alpha_l} e^{2i\delta_l}$  in Eq.(2.14) reducing the outgoing wave.  $\alpha_l = 0$  means no absorption and  $\alpha_l = \infty$  total absorption. Note that for full absorption, the partial wave  $\Psi_{k,l}(r, \varphi)$  differs from the free wave  $\Psi_{k,l}^{(0)}(r, \varphi)$  by the missing outgoing wave, i.e. there are strong scattering effects. In optics, this typical wave phenomenon is referred to as shadow or black dot scattering.

The probability per area of finding a particle that is in the state of a free circular wave function rises from the origin of the coordinate system like

$$|\Psi_{k,l,m}^{(0)}(r, \varphi)|^2 \underset{kr \rightarrow 0}{\approx} \frac{k}{2\pi} \left( \frac{kr}{2^l l!} \right)^{2l}. \quad (2.15)$$

Thus particles with high angular momentum  $l$  and small energy (small  $k$ ) will be less affected by a potential localized at  $r = 0$ . For the scattering of surface-state electrons by adatoms with electron energies close to the fermi energy, it is sufficient to consider  $s$ -wave ( $l = 0$ ) scattering only, because  $k_F \approx 0.1 \text{ \AA}^{-1}$  (Table 3.1) and the range  $r_0$  of the scattering potential is typically  $r_0 \approx 1 \text{ \AA}$  (basically determined by one over the Thomas-Fermi screening length of the bulk electrons), i.e.  $p$ -waves ( $l = 1$ ) have more than two orders of magnitude less overlap with the scattering potential.

Whereas in scattering experiments only the flux of the outgoing wave is accessible, it is possible with STM to directly observe the space and energy dependence of the LDOS of the scattered partial waves. The LDOS of a free 2DEG of independent electrons is given by incoherent summation of the absolute values of the free circular waves over all  $l$  and the two spin directions (that are assumed to be degenerate):

$$\begin{aligned}\rho^{(0)}(E, r, \varphi) &= 2 \sum_{l=-\infty}^{+\infty} |\Psi_{k,l}^{(0)}(r, \varphi)|^2 \\ &= \frac{m^*}{\pi \hbar^2},\end{aligned}\tag{2.16}$$

which is a constant  $L_0 = \frac{m^*}{\pi \hbar^2}$  in space and energy starting at the onset of the 2DEG which has been set equal to zero in this section. The change in the LDOS due to scattered partial waves of energy  $E$ , with  $k(E)$  determined by the dispersion of the 2DEG, is given by:

$$\begin{aligned}\Delta\rho(E, r) &= 2 \sum_{l=-\infty}^{+\infty} \left( |\Psi_{k,l}(r, \varphi)|^2 - |\Psi_{k,l}^{(0)}(r, \varphi)|^2 \right) \\ &\xrightarrow{kr \rightarrow \infty} \sum_{l=-\infty}^{+\infty} \frac{k^2}{\pi} \frac{1}{kr} \left[ \frac{e^{-4\alpha} - 1}{2} + e^{-2\alpha} \sin(2kr + l\pi + 2\delta_l) - \sin(2kr + l\pi) \right] \\ &\xrightarrow[\alpha \rightarrow 0]{kr \rightarrow \infty} \sum_{l=-\infty}^{+\infty} \frac{k^2}{\pi} \frac{1}{kr} [\sin(2kr + l\pi + 2\delta_l) - \sin(2kr + l\pi)],\end{aligned}\tag{2.17}$$

which is a function with period  $\pi$  of the phase shift valid for  $kr \gg 1$ . The change in the electron density  $\Delta n(r)$  of the 2DEG is given by summation over the  $\Delta\rho(E, r)$  of all occupied  $\Psi_{k,l}$ . At low temperatures, the discontinuity in the electron occupation at the Fermi surface causes oscillation of  $\Delta n(r)$  with wave number  $2k_F$ . Friedel examined such oscillations to calculate the conductivity of dilute metallic alloys [88]. Whereas Friedel oscillations escape from direct observation in the bulk, they become apparent at the surface [89]. STM topographs taken at low bias directly reflect the oscillating LDOS close to  $E_F$ , enabling direct observation of the Friedel oscillations. Such oscillations of surface-state electrons can be seen in Fig. 3.1 where the scattering occurs at step edges and impurities.

## 2.3 Scattering resonance and Fano line shapes

When an atom chemisorbs on a metal surface, an electron in an atomic orbit  $\Phi_a$  has a finite transition probability to the continuum of conduction band states because of hybridization. The coupling to the continuum of states shifts and spreads out the

discrete energy  $E_a$  of the atomic level to a resonance of energy levels at  $E_r = E_a + \Lambda$  of the combined substrate-adatom system [90, 91]. This resonance is also referred to as quasidiscrete level or virtual bound state: the electrons spend a relatively large proportion of the time in the region of the adatom, but it is not a bound state because the wave functions become Bloch states far from the adsorbate. For weak coupling, the width  $\Gamma$  of the resonance is related to the lifetime  $\tau$  of the electron to stay in the atomic orbit by  $\Gamma = \hbar/\tau$ .  $\tau$  is also referred to as the mean autoionisation time. Mathematically, the lifetime of the quasidiscrete state can be described by a complex energy  $E = E_r + i\Gamma/2$  of the electron: the time factor of the wave function  $e^{-iEt/\hbar} = e^{-iE_r t/\hbar} e^{-\Gamma t/2\hbar}$  from the imaginary energy part damps the probability of finding the electron in the atomic orbit exponentially with time by  $e^{-t/\tau}$ .

The LDOS of the atomic orbit is converted by the chemisorption interaction from a discrete delta function at  $E_a$  to a Lorentzian density around  $E_r$ . The LDOS of the conduction electrons as a function of energy depends on the distance to the adatom: the quasidiscrete state gives rise to a scattering resonance of the conduction electrons with strongly energy dependent phase shifts  $\delta_l(E)$  close to  $E_r$ . For a small imaginary energy,  $\delta_l(E)$  can be approximated by a resonance law [92, 93] (similar to the law of the phase shift of a damped swinging mass to an oscillating excitation force)

$$\delta_0(E) = \delta_{bg} + \frac{\pi}{2} \pm \arctan \varepsilon, \quad (2.18)$$

where  $\varepsilon = (E - E_r)/(\Gamma/2)$  and  $\delta_{bg}$  is the background phase shift far away from  $E_r$  due to other adsorbate-metal interactions such as hybridization of the other adsorbate electronic states. The total change of the phase shift over the whole resonance varies from  $\delta_{bg}$  at  $\varepsilon = -\infty$  to  $\delta_{bg} \pm \pi$  at  $\varepsilon = \infty$ . The energy dependence of the change of the conduction electron LDOS  $\Delta\rho_l(E, r)$  (Eq. (2.17)) with a resonantly increasing scattering phase shift  $\delta_l(E)$  given by Eq. (2.18) can be transformed to

$$\Delta\rho_l(E, r) \underset{kr \rightarrow \infty}{\sim} \frac{k^2}{2\pi} \frac{1}{kr} \left[ \sin(2kr + l\pi + 2\delta_{bg}^l) - \sin(2kr + l\pi) + 2a(\beta) \frac{2q(\beta)\varepsilon + q(\beta)^2 - 1}{\varepsilon^2 + 1} \right], \quad (2.19)$$

with  $q(\beta) = \sin(\beta)/\cos(\beta)$ ,  $a(\beta) = \cos^2(\beta)$ , and  $\beta = kr - \frac{l\pi}{2} - \frac{\pi}{4} + \delta_{bg}^l$ . For weak dispersion within the resonance, i.e.  $k(E) \approx k(E_r)$ ,  $q(k, r)$  and  $A(k, r)$  can be assumed to be energy independent. The line shape of Eq. (2.19) as a function of  $\varepsilon$  is then primarily determined by  $q(r)$  in the last term of the equation (Fig. 2.3).  $q$  is referred to as the Fano line shape parameter after Ugo Fano who studied such line shapes in the context of atomic excitation spectra [93, 94].

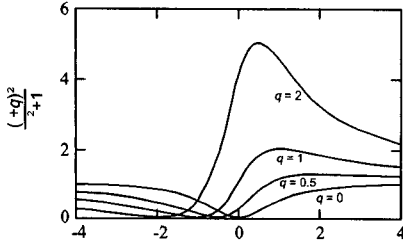


**Figure 2.3:** Fano line shapes  $((\varepsilon + q)^2/(\varepsilon^2 + 1) = 1 + (2q\varepsilon + q^2 - 1)/(\varepsilon^2 + 1)$ , see Eq.(2.28)) for different values of the Fano line shape parameter  $q$ . The Fano line shape is a negative Lorentzian for  $q = 0$ , a positive Lorentzian for  $q = \pm\infty$  and most asymmetric for  $q = \pm 1$ . The maxima are at  $\varepsilon = 1/q$  with an amplitude of  $1 + q^2$ . Reverse the scale of abscissas for negative  $q$ .

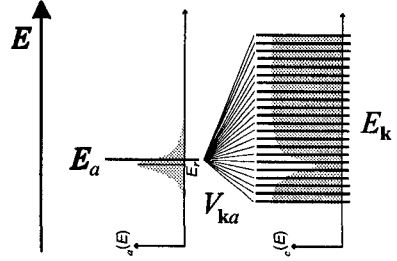


**Figure 2.4:** Energy scheme of the resonant level model. The adsorbate level  $E_a$  is coupled to the conduction levels  $E_k$  via the hybridization matrices  $V_{ka}$ . The thick horizontal lines are the discrete energy levels with no hybridization present. The interaction broadens and shifts the adsorbate's density of states  $\rho_a(E)$  and modifies the conduction electron density of states  $\rho_c(E)$ .

### 2.3.1 The non-interacting resonant level model

The electronics of an adsorbate on a metal surface can be described by a very general Hamiltonian specifying all the electrons and their interactions, but first principle calculations based on such a Hamiltonian would be difficult due to the strong Coulomb interactions. Instead, adsorbate effects are commonly calculated from a simpler phenomenological model Hamiltonian, the resonant level model (RLM) Hamiltonian [90,93,95,96], which describes the low energy excitations associated with the adsorbate and ignores features that are not directly relevant to the calculation of the adsorbate effects. The Fano resonances can be derived from the RLM Hamiltonian, also called Newns-Fano Hamiltonian or non-interacting Anderson Hamiltonian, using the Green's function techniques. The RLM Hamiltonian reads, in the non-degenerate second-quantized form:

$$H = \sum_{\mathbf{k}} E_{\mathbf{k}} n_{\mathbf{k}} + E_a n_a + \sum_{\mathbf{k}} [V_{ka} c_{\mathbf{k}}^\dagger c_a + V_{ka}^* c_a^\dagger c_{\mathbf{k}}], \quad (2.20)$$

where the first term represents the conduction band of the metal substrate,  $E_{\mathbf{k}}$  is the energy of the conduction band electronic state of wavevector  $\mathbf{k}$ ,  $c_{\mathbf{k}}^\dagger$  and  $c_{\mathbf{k}}$  are the corresponding creation and annihilation operators, and  $n_{\mathbf{k}} = c_{\mathbf{k}}^\dagger c_{\mathbf{k}}$  is the electron number operator. The conduction states are characterized by their density of states given by  $\rho_c^0(E) = \sum_{\mathbf{k}} \delta(E - E_{\mathbf{k}})$ . The second term in Eq. (2.20) represents the single localized

adatom orbital  $\Phi_a(\mathbf{r})$  of energy  $E_a$ ,  $n_a = c_a^\dagger c_a$  is the number operator for the adatom orbital. The third term in Eq. (2.20) represents the hybridization energy between the localized state and the conduction band wave functions of the metal. The products of the creation and annihilation operators describe the hopping of electrons away from (first term) and to (complex conjugate of the first term) the adatom, with a weight given by the hybridization matrices  $V_{ka}$  (Fig. 2.4).

### 2.3.2 The adsorbate LDOS

The retarded one-electron Green's operator of the Hamiltonian  $H$ , fourier transformed to the energy (frequency) representation, is given by

$$G(E + i\eta) = \frac{1}{E + i\eta - H}, \quad (2.21)$$

with infinitesimal positive  $\eta \rightarrow 0^+$ . The adsorbate projected Green's function  $G_{aa}(E + i\eta) = \langle a | G(E + i\eta) | a \rangle$  may be renormalized to

$$G_{aa}(E + i\eta) = \frac{1}{E + i\eta - E_a - \Sigma_{aa}(E + i\eta)}, \quad (2.22)$$

with the complex self-energy

$$\begin{aligned} \Sigma_{aa}(E + i\eta) &= \sum_{\mathbf{k}} \frac{|V_{ka}|^2}{E + i\eta - E_{\mathbf{k}}} \\ &\underset{\eta \rightarrow 0}{=} \Lambda(E) - i \frac{\Gamma(E)}{2}, \end{aligned} \quad (2.23)$$

where  $\Gamma(E) = 2\pi \sum_{\mathbf{k}} |V_{ka}|^2 \delta(E - E_{\mathbf{k}})$  is a weighted density of states (replacing  $|V_{ka}|^2$  by its average value  $\langle V^2 \rangle$  gives  $\Gamma(E) = 2\pi \langle V^2 \rangle n_0(E)$ , where  $n_0$  is the density of conduction states in the absence of the adsorbate). The shift of the resonance  $\Lambda(E) = (1/\pi) \mathcal{P} \int_{-\infty}^{\infty} \Gamma(E') / (E - E') dE'$  is the Hilbert transform of  $\Gamma$  according to the Kramers-Kronig relation.  $\mathcal{P}$  denotes the Cauchy principle value of the integral. Thus, the renormalized Hamiltonian is complex  $H^r(E) = E_a + \Lambda(E) - i\Gamma(E)/2$  with a life time given by  $\tau = \hbar/\Gamma$ , as explained in Section 2.3. The adsorbate projected LDOS is

$$\begin{aligned} \rho_a(E) &= \lim_{\eta \rightarrow 0} \left[ -\frac{1}{\pi} \text{Im} G_{aa}(E + i\eta) \right] \\ &= \frac{\Gamma(E)}{2\pi} \frac{1}{(E - E_a - \Lambda(E))^2 + (\Gamma(E)/2)^2} \\ &= \frac{2}{\pi \Gamma(E)} \frac{1}{1 + \varepsilon^2} \end{aligned} \quad (2.24)$$

with

$$\varepsilon = \frac{E - E_a - \Lambda(E)}{\Gamma/2}. \quad (2.25)$$

In the wide band limit,  $\Gamma(E) \approx \Gamma(E_a)$  and  $\Lambda(E) \approx \Lambda(E_a)$  are only weakly dependent on energy and  $\rho_a(E)$  is a Lorentzian shaped resonance at  $E_r = E_a + \Lambda(E_a)$  of full width  $\Gamma(E_a)$  at half maximum (fwhm). Thus, the effect of the hybridization is to shift and broaden the discrete energy level of the adatom, as described in Section 2.3.

### 2.3.3 The conduction band electron LDOS

The change  $\Delta G_c$  of the free conduction electrons Green's function  $G_c = G_c^0 + \Delta G_c$  due to the presence of the adsorbate can be determined by the  $t$  matrix technique:

$$\Delta G_c = G_c^0 t G_c^0. \quad (2.26)$$

For  $V = V_{ka}$  ( $s$ -wave scattering), the  $t$  matrix is proportional to the adsorbate projected Green's function  $G_{aa}$  [48, 95]:

$$t(E) = \frac{\Gamma}{2\pi\rho_0} G_{aa}(E). \quad (2.27)$$

The perturbation in the conduction electron LDOS  $\Delta\rho_c$  is given by:

$$\begin{aligned} \Delta\rho_c(E) &= \lim_{\eta \rightarrow 0} \left[ -\frac{1}{\pi} \text{Im} \Delta G_c(E + i\eta) \right] \\ &= -\frac{1}{\pi} (\text{Im} G_c^0(E))^2 [(q^2 - 1) \text{Im} t(E) - 2q \text{Re} t(E)] \\ &= \frac{1}{\rho_0 \pi^2} a(E) \frac{2q(E)\varepsilon + q(E)^2 - 1}{1 + \varepsilon^2}, \end{aligned} \quad (2.28)$$

where  $\text{Re} t(E) = -\varepsilon \text{Im} t(E) = \frac{1}{\pi\rho_0} \frac{\varepsilon}{1+\varepsilon^2}$ ,  $a(E) = (\text{Im} G_c^0(E))^2$  and the Fano line shape parameter

$$q(E) = \frac{\text{Re} G_c^0(E)}{\text{Im} G_c^0(E)}. \quad (2.29)$$

If the adsorbate resonance is sharp, the energy dependence of  $q$  can be neglected within the resonance. But  $q$  will vary strongly with the distance to the adsorbate because of its dependence on the conduction electron Green's functions. For example, the Green's function  $G_c^0 = \sum_{\mathbf{k}} G_{\mathbf{k}\mathbf{k}}^0(E, \mathbf{r}, \mathbf{r}')$  of free 2d electrons of positive energy  $E = \hbar\mathbf{k}^2/2m$  in the  $\mathbf{r}$ -representation are [97]:

$$G_c^0(E, \mathbf{r}, \mathbf{r}') = -\frac{i}{4} H_0^+(\mathbf{k}(\mathbf{r} - \mathbf{r}')). \quad (2.30)$$

The corresponding  $q(r)$  oscillates between  $-\infty$  and  $\infty$ , i.e. the Fano line shapes change from Lorentzian dips to peaks with an oscillation period given by the wave number  $k(E_r)$ .



### 2.3.4 The tunneling conductance

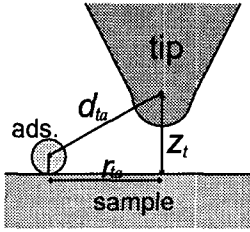


Figure 2.5: Measurement geometry.

For the atomic physics processes like light absorption studied by Fano [93,94], both the discrete state under investigation and the probe state, that is the initially excited decaying or autoionizing state, are atomic states spatially localized at the same site by the same atomic central potential. This means that only the value of  $q$  with the probe's focus fixed at the site of the discrete state can be determined.

In contrast, the spatial degree of freedom the STM, i.e. the possibility to move the probe (the tip) with respect to the adsorbate, introduces the possibility to measure the distance dependence of  $q$ . Tunneling may take place directly into the adsorbate LDOS as well as into the perturbed conduction band LDOS, dependent on the strength of the corresponding tunneling matrices. The tunneling matrices depend on the overlap of the tip wave function  $\Phi_t(\mathbf{r})$  with the adsorbate  $\Phi_a(\mathbf{r})$  and conduction electron wave functions. Tunneling into the adsorbate LDOS will be localized close to the adsorbate site with an approximately exponential drop off with the tip-adsorbate distance:

$$T_{ta}(\mathbf{r}_t, \mathbf{r}_a) = \int d^3 \mathbf{r} \Phi_p^*(\mathbf{r} - \mathbf{r}_a) v_{ta}(\mathbf{r}; \mathbf{r}_t; \mathbf{r}_a) \Phi_a(\mathbf{r} - \mathbf{r}_a) \propto e^{-\frac{d_{ta}}{\alpha}}, \quad (2.31)$$

where  $v_{ta}$  is the potential representing the mutual interaction of the tip and the adsorbate,  $d_{ta}$  the tip-adsorbate distance (Fig. 2.5), and  $\alpha$  an effective decay constant. The presence of the adsorbate effects the conduction LDOS over a long range. Tunneling into the perturbed conduction LDOS can be interpreted as an indirect tunneling into the adsorbate LDOS via tunneling into the conduction states, conduction state propagation and hopping to the adsorbate state. Both tunneling channels, the direct one into the adsorbate LDOS and the indirect one via the conduction states, interfere, i.e.  $q$  can be approximated as the sum of two terms [55,98]:

$$q(\mathbf{r}_t) = \frac{\text{Re } G_c(r_{ta}) + D(d_{ta})}{\text{Im } G_c(r_{ta})}, \quad (2.32)$$

where  $D(d_{ta}) = D_0 e^{-\frac{d_{ta}}{\alpha}}$ .  $D_0$  is a constant dependent on the strength of the coupling of the conduction states to the adsorbate and the tip, and  $G_c$  is the Green's function of the conduction electrons as seen by the tip [98].

## Chapter 3

### The $s$ - $p$ -derived noble metal (111) surface states

Surface states are electron states localized close to the surface of a solid. The envelope of their probability amplitude decays exponentially into the vacuum as well as into the bulk, with an oscillating penetration of a few atomic layers (Fig. 3.3). The origin of surface states lies in the breaking of the translational symmetry perpendicular to the surface: In an infinite crystal complex Bloch wave vectors are forbidden because

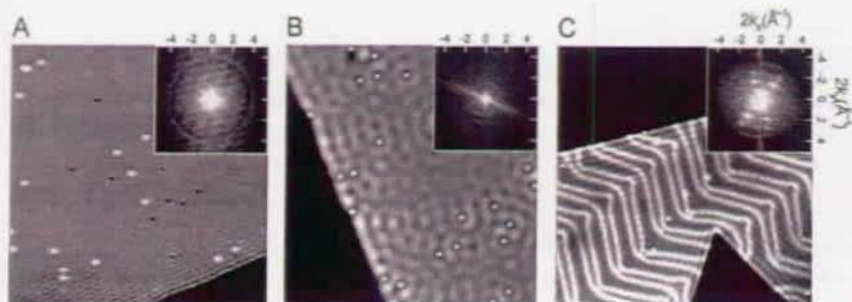


**Figure 3.1:** STM topographs ( $70 \text{ nm} \times 70 \text{ nm}$ , bias  $50 \text{ mV}$ ) of the noble metal (111) surfaces with low coverages  $\theta \approx 10^{-4} \text{ ML}$  of Co adatoms (white dots). Friedel oscillations of the surface state electron density can be seen at the atomic steps and around adatoms and impurities. The insets are the Fourier transforms of the images, with the Fermi surface at  $2|k_F|$ . (A) Cu(111): the black dots are impurities of unknown chemical identity. (B) Ag(111). (C) The Au(111) surface is reconstructed, known as the "herringbone" reconstruction. The "soliton" walls (the zig-zag lines) separate hcp and fcc domains. The Fourier transform (from a different image) reproduces the long-range  $22 \times \sqrt{3}$  symmetry of the reconstruction.

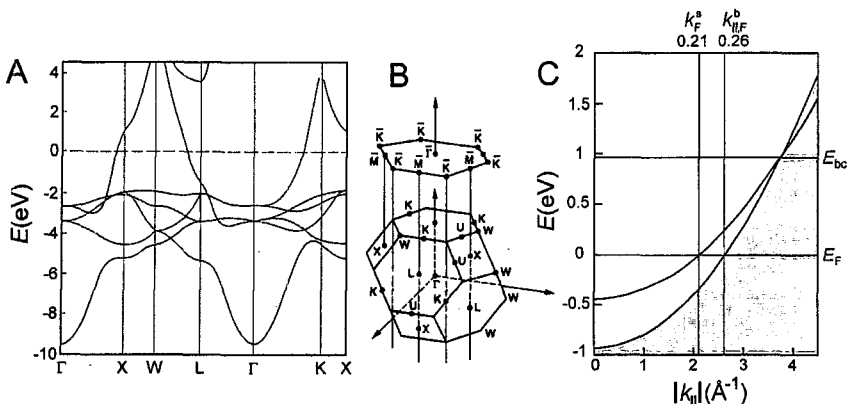


**Figure 3.2:** (A) Calculated bulk bands of Cu. No band crosses the Fermi energy along the direction  $\Gamma L$ . It is in this so called L gap that the  $s$ - $p$  derived surface state exists. (Figure from Ref. [99].) (B) First Brillouin zone for an fcc lattice and the corresponding surface Brillouin zone (SBZ) for the (111) surface. The distance  $\bar{\Gamma}\bar{K}$  is given by  $4\pi/3a$ , where  $a$  is the next neighbor distance. (Figure from Ref. [100].) (C) Electronic band structure of the (111) surface of Cu in the SBZ center around  $\bar{\Gamma}$ . There exist bulk states in the gray regions. The dispersion of the surface state (solid line) is parabolic with a positive effective mass of  $m^* = 0.38 m_e$ . (Reproduced from Ref. [101].)

the corresponding wave functions grow exponentially and can thus not be normalized. But at a surface, exponentially growing wave functions can be matched to exponentially decaying vacuum tails. Parallel to the surface, the surface state electrons are free to move and consequently constitute a good approach to a dynamically two-dimensional electron gas (2DEG). Since the 2D translational symmetry parallel to the surface persists, the surface states can be characterized by the Bloch wave vector  $k_{||}^s$ . A prerequisite for the existence of a true surface state is the absence of bulk states with the same energy and same  $k_{||}$  (Fig. 3.2). When a surface state band crosses a bulk band, so-called surface resonances appear, which are extended states with an enhanced probability amplitude at the surface.

The total number of bulk states in a real sample is comparable to the number of atoms, i.e.  $\approx 10^{23}$ , whereas the number of surface states is of the order of the number of surface atoms of the sample, i.e.  $\approx 10^{15}$ . Thus there are about  $10^8$  bulk states per surface state in a macroscopic sample. Therefore the surface states can be completely neglected when one is interested in bulk properties. However, surface properties are influenced by surface states because they contribute a considerable fraction to the

	$E_{\bar{\Gamma}}$ (meV)	$\frac{m^*}{m_e}$	$k_F^s, k_F^b, \min k_{F\parallel}^b$ ( $\frac{1}{\text{\AA}}$ )	$\frac{\lambda_F^s}{2}$ (Å)	$n_0$ ( $\frac{10^{13}}{\text{cm}^2}$ )	$\tau_{E_{\bar{\Gamma}}}$ (fs)	$E_{bc}$ (eV)
Cu(111)	-445	0.38	0.21, 1.36, 0.26	15	7.1	27	0.96
Ag(111)	-67	0.40	0.083, 1.20, 0.15	38	1.1	120	0.35
Au(111)	-505	0.27	0.17, 1.21, 0.22	20	5.7	35	1.20

**Table 3.1:** Characteristics of the *s-p*-derived noble metal (111) surface-states: STS values for the band onset energies  $E_{\bar{\Gamma}}$  [31], effective masses  $m^*$  [31], Fermi wave vectors  $k_F^s$  as well as the bulk Fermi wave vectors  $k_F^b$  [128] and their smallest components  $k_{F\parallel}^b$  parallel to the surface [101], Fermi wavelengths  $\lambda_F^s/2 = \pi/k_F^s$ , total surface-state electron density  $n_0 = |E_{\bar{\Gamma}}|m^*/(\pi\hbar^2)$ , and quasi surface-state electron life times  $\tau_{E_{\bar{\Gamma}}}$  at the band onset energies [31] as well as the calculated bulk – surface-state band crossing energies  $E_{bc}$  [101].

local density of states at the surface. For example, they affect the physisorption potential [12, 102, 103], their contribution is relevant for the total energy balance of surface reconstructions [104, 105], they play an important role in the epitaxial growth on metal surfaces [103, 106], and even the equilibrium crystal shape may be influenced through surface-state mediated interactions between step edges [107], in a way similar to the adsorbate-adsorbate interactions described in Chapter 4.

Surface states are present on many different crystal surfaces of metals and semiconductors [11, 12, 100, 108]. The noble metal (111) surfaces harbor *s-p*-derived surface states placed in a bulk band gap around the Fermi energy. The gap results from an *s-p* band crossing in the  $\Gamma$ L projected bulk band structure in the SBZ center around  $\bar{\Gamma}$  (Fig. 3.2). There are two further surface states on the noble metal (111) surfaces but their bands are far away from the Fermi energy, i.e. they are difficult to access by STS and they are irrelevant to physical effects happening at the Fermi edge like the ones studied here. The *s-p*-derived surface states have been extensively studied by angle-resolved photoemission spectroscopy [86, 109–123] and  $\mathbf{k}$ -resolved inverse photoemission spectroscopy [124–127], and STM [14–33]. The fact that similar dispersions of the surface states have been found by photoemission spectroscopy and STS establishes the STM as a new spectroscopic surface analysis tool. In the surface plane, the surface state’s dispersion is parabolic and isotropic:

$$E = E_{\bar{\Gamma}} + \frac{\hbar^2}{2m^*} k_{\parallel}^2. \quad (3.1)$$

with positive effective masses  $m^*$  and an energy onset  $E_{\bar{\Gamma}}$  below the Fermi energy (Table 3.1).

Deviations from the parabolic behavior only start at energies higher than 1 eV above the Fermi energy, band crossing with bulk bands occurs at  $\approx 1$  eV (Table 3.1). As derived

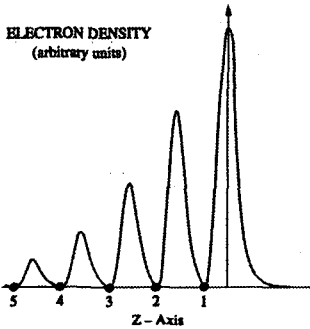


**Figure 3.3:** Probability density  $\rho$  of a surface-state electron.  $z$  denotes the direction perpendicular to the surface, the black dots are the atomic layers of the substance. (Figure from Ref. [129]).

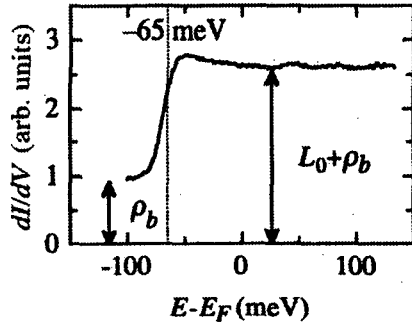


**Figure 3.4:** Spectrum taken in the center of a clean wide Ag(111) terrace showing the onset of the surface-state ( $T = 6$  K, bias = 91 mV,  $I = 1$  nA). Close to  $E_F$ , the surface-state contributes strongly to the tunneling current  $I$  (up to  $2/3$  of  $I$ ). (Reproduced from Ref. [76].)

in Section 2.2, the LDOS of a 2DEG with a free dispersion like in Eq.(3.1) sets on with a step at  $E_F$  and is constant for higher energies,  $\rho_{2D}(E) = L_0 \Theta(E - E_F)$ , where  $\Theta$  is the step function. STS spectra taken on flat terraces far from impurities show such a behavior (Fig. 3.4). That the onset is not abrupt is due to the limited lifetimes of the surface-state quasiparticles [31]. Thermal excitations ( $\approx 0.5$  meV at 6 K) at the operating temperature of the STM are negligible. Lifetimes of the surface-state electrons at  $E_F$  derived from the width of the surface-state onset are given in Table 3.1.

From Eq. 2.1 one could argue that the surface-state electrons hardly contribute to the tunneling current because they have no momentum perpendicular to the surface, i.e. little momentum towards the tip. That they do contribute and even dominate the tunneling current at the onset of the surface-state (Fig. 3.4) is due to their limited lifetimes: For a typical tunneling current of 1 nA, one electron tunnels on average every 0.16 ns which is about three orders of magnitude longer than the lifetimes of the surface-state electrons (Table 3.1). As a consequence, the electron can easily scatter into other single-particle states during the "slow" tunneling process, i.e. the relaxation rate is faster than the tunneling rate so that current may flow [130].

The total density  $n_0$  of the surface-state electron gas is given by  $n_0 = |E_F|L_0$  (Table 3.1). Compared to other 2DEG systems, the noble metal (111) surface-states constitute a high-density 2DEG ( $n_0 \approx 10^{13}$  electrons/cm<sup>2</sup>) of low-mobility  $\mu = e\tau/m^*$ . Other

2DEGs are realized for example in the metal-oxide-semiconductor field effect transistor (MOSFET) with  $n_0$  tunable from 0 to  $10^{13}$  electrons/cm<sup>2</sup>, in semiconductor heterojunctions with  $n_0 \approx 10^{11} - 10^{12}$  electrons/cm<sup>2</sup> [131], or on the surface of liquid helium with  $n_0 = 10^5 - 10^9$  electrons/cm<sup>2</sup>, where the electrons are trapped by a combination of an electric field and an image potential [132, 133].

The surface-state electrons are surrounded by the highly polarizable bulk electron gas. It screens the Coulomb field of each surface-state electron by a positively charged depletion cloud of bulk electrons. The screening is very efficient because on the one hand there are about  $10^8$  bulk states for every surface-state and on the other hand because the Thomas-Fermi screening length of the bulk electrons is about one order of magnitude shorter than the one of the surface-state electrons (Table 3.1). The surface-state electrons thus effectively behave like uncharged and independent particles. As a consequence, external potentials are not screened by the surface-state electrons in a Thomas-Fermi way (which is the reason for the pronounced LDOS oscillations around scatterers as seen in Fig. 3.1) and the lifetimes of surface-state quasiparticles with energies far above the Fermi energy are mainly governed by inelastic electron-electron scattering with bulk electrons [28].



# Chapter 4

## Long-range adsorbate interactions mediated by a two-dimensional electron gas

### 4.1 Thermal hopping rate of individual adsorbates

The dynamics of an atom adsorbed on a surface is fundamentally a complex quantum-mechanical problem. An important simplification is obtained by using the Born-Oppenheimer approximation to separate the motion of the nuclei from the electronic degrees of freedom and by neglecting quantum-mechanical effects of the adatom like tunneling and zero-point motion, which are good approximations for the massive Co and Cu atoms studied here. Due to the periodic arrangement of the surrounding substrate atoms, the adsorbed atoms experience a periodic potential along the surface. In order to diffuse, the adatom must pass over the energy barrier that separates regions of lower energies from each other, the surface lattice sites. The barrier region, called bridge site or saddle point, is a transition state, a state that must be visited during the passage from one site to another and it acts as a bottleneck for the transition reaction. The migration barrier  $E_m$  for diffusion is the difference between the barrier energy and minimum energy of the potential along the surface. If  $E_m$  is large compared with the thermal energy  $k_B T$ , the adatoms are mainly localized at fixed surface lattice sites with occasional hops to neighboring sites driven by the substrate's heat bath providing stochastic excitations. With the assumption of  $E_m \gg k_B T$ , the hopping rate of uncorrelated jumps between adjacent lattice sites can be quantified according to transition state theory (TST) [134–137] in the form of an Arrhenius law:

$$\nu(T) = \nu_0(T) e^{-\frac{E_m}{k_B T}}, \quad (4.1)$$



where the Boltzmann factor is given by one over the exponent of the proportion of the migration barrier  $E_m$  to the thermal energy  $k_B T$ . Eq. (4.1) can be derived from thermal equilibrium considerations about the speed and the position of the adatom within the potential landscape of the substrate. The prefactor of Eq. (4.1), the attempt frequency  $\nu_0$ , is given by the frequency-product formula of Vineyard for a single adsorbate [138]:

$$\nu_0(T) = \frac{\prod_{i=1}^{3N+3} \nu_i^I}{\prod_{i=1}^{3N+2} \nu_i^T}, \quad (4.2)$$

where  $\nu_i^I$  and  $\nu_i^T$  are all the harmonic-vibration frequencies of the whole system with the adsorbate in the initial lattice site and in the transition state, respectively, and  $N$  denotes the number of atoms of the substrate. The attempt frequency is a measure of the entropy at the transition state, as compared to that of the initial state. The frequencies  $\nu_i^I$  and  $\nu_i^T$  that are most strongly coupled to the motion of the adatom are roughly proportional to the harmonic-vibration frequency of the potential-energy minimum at the initial site and the maximum at the transition site, respectively. If the substrate is not strongly perturbed by the motion of the adatom, the dependence of  $\nu_0$  on all frequencies other than those associated with the adatom may be neglected [139, 140], i.e.  $N = 0$ . Usually the frequencies lie in the range 1-10 THz, and  $\nu_0$  is expected to lie in that range, as well [141, 142].  $\nu_0$ , essentially determined by the curvature of the potential energy minimum and maximum, scales weakly as  $\nu_0 \propto \sqrt{E_m}$  on the distance of the minimum of energy to the maximum of energy, i.e. the migration barrier. This counteraction of the prefactor to the Boltzmann factor is referred to as the compensation effect.

The hopping rate  $\nu(T)$  of isolated adsorbates as a function of temperature is measured here in a most direct way by tracing their trajectory on consecutive STM images taken from the same surface area. In comparison to other, established techniques for the determination of the diffusion rate, the direct STM method used here has the advantage of the control of the surface quality, the high number of systems that can be investigated and the close link to the transition-state theory. Much care has to be taken to avoid tip influences on the diffusion rate. That the tip might interact strongly with adsorbates is known from atom manipulation experiments, where the tip is used to move adsorbates [143–147]. Here, the tip influence was minimized by increasing the tip-surface distance, i.e. lowering the electric field ( $I \approx 50$  pA with  $U \approx 300$  mV,  $R \approx 6$  G $\Omega$ ) and by increasing the scanning speed, i.e. the time of influence of the electric field on the adsorbate, as much as possible without losing the necessary resolution to resolve the single hopping events. The influence of the tip on the hopping rate was controlled by comparing the diffusion rates determined with different image recording rates: As soon

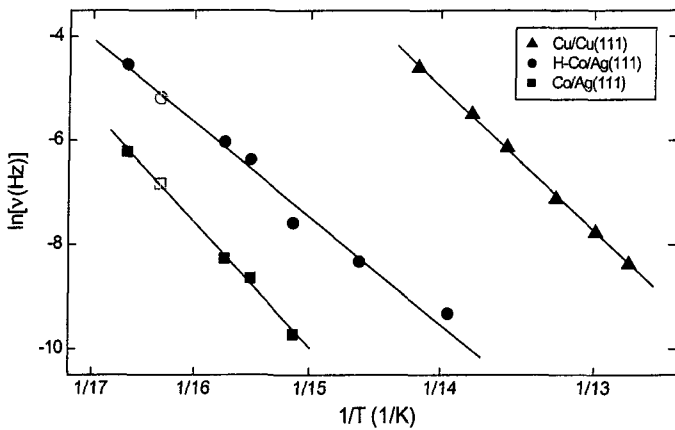


**Figure 4.1:** Arrhenius plot of the hopping rates of isolated Co adatoms ( $\nu_0 = 3 \times 10^{13}$  Hz,  $E_m = 50 \pm 2$  meV) and H-Co adsorbates ( $\nu_0 = 2 \times 10^9$  Hz,  $E_m = 38 \pm 2$  meV) on the Ag(111) surface as well as Cu adatoms ( $\nu_0 = 1 \times 10^{12.0 \pm 0.5}$  Hz,  $E_m = 40 \pm 1$  meV) on the Cu(111) surface. The data in gray has been determined from a series of STM images which can be seen animated under: [http://www.mpi-stuttgart.mpg.de/KERN/Res\\_act/supmat\\_3.html](http://www.mpi-stuttgart.mpg.de/KERN/Res_act/supmat_3.html).

as the image recording rate is high enough to record every hopping event, increasing the image recording rate should not influence the observed hopping rate unless there are tip influences. We found that for  $R > 100$  M $\Omega$  increasing the image recording rate four fold did not alter the hopping rates more than within the statistical error.

The average hopping rate  $\nu(T)$  of a single adatom is given by the total number of hopping events within a series of STM images taken at temperature  $T$  divided by the number of adsorbates on the scanned surface area and the time elapsed during the series of images. An animated series of STM images used to determine the hopping rate of Cu adatoms on Cu(111) at 13.5 K can be found at:

[http://www.mpi-stuttgart.mpg.de/KERN/Res\\_act/supmat\\_1\\_1.html](http://www.mpi-stuttgart.mpg.de/KERN/Res_act/supmat_1_1.html)

The frames of this movie (35 nm  $\times$  35 nm, bias = 100 mV,  $I = 1$  nA,  $T = 13.5$  K, 120 s per frame) are topographs of the Cu(111) surface, the white spots are Cu adatoms, the black spots are impurities. Each data point  $\nu(T)$  in Fig. 4.1 is from such a series of  $\approx 20$  STM topograph. Generally, low adsorbate coverages  $\theta \approx 10^{-4}$  ML have been used to minimize the effects of adsorbate-adsorbate interactions on the hopping rate. The image sizes ( $\approx 50$  nm) were chosen to include as many adsorbates as possible to improve the statistics under the restriction that the jumps of the adsorbates are resolved (for example 4 Å for jumps from fcc to fcc sites on Cu(111)). To simplify the analysis care



**Figure 4.2:** Constant current STM image ( $30 \text{ nm} \times 30 \text{ nm}$ ,  $I = 0.8 \text{ nA}$ , and  $-60 \text{ mV}$  bias) of two Co adatoms ( $0.8 \text{ \AA}$  high) and seven H-Co adsorbate complexes ( $0.6 \text{ \AA}$  high) on the Ag(111) surface (see also Fig. 5.7(B)). The concentric rings around the adsorbates are the Friedel oscillations in the surface-state electron density.

is taken that the temperature is low enough for the average jump rate ( $10^{-5}$  to  $10^{-2} \text{ Hz}$ , see Fig. 4.1) to stay well below the image recording rate ( $10^{-2}$  to  $10^{-1} \text{ Hz}$ ), i.e. it is assumed that every jump is recorded.

The jump rates of the studied systems show an Arrhenius behavior (Fig. 4.1). The experimental migration barrier of Cu/Cu(111) of  $E_m = (40 \pm 1) \text{ meV}$  is within the error of a previously reported value of  $E_m = (37 \pm 5) \text{ meV}$  [44], and compares well with recent *ab-initio* calculations of  $E_m = 50 \text{ meV}$  [148]. The attempt frequency  $\nu_0 = 1 \times 10^{12.0 \pm 0.5} \text{ Hz}$  lies within the usual range of  $\nu_0 = 10^{12-13} \text{ Hz}$ . We observe only jump distances of entire lattice spacings indicative of a significant binding energy difference between the two three-fold hollow sites. In agreement, theory finds the hcp site to be as unstable as the bridge site and therefore predicts diffusion to occur between fcc sites only [148].

#### 4.1.1 The skyhook effect

In this subsection, the effect of hydrogen adsorption to a metal adatom on the diffusion properties of the adatom are investigated. The results are used in Chapter 5.3 to interpret the strong electronic effects the hydrogen induces. Hydrogen adsorbed to a metal adatom is known to weaken the adatom's bond to the substrate, as demonstrated

by thermal diffusion experiments [149,150] and calculations [150,151]. Figuratively, the strong hydrogen bond to the adatom pulls the adatom away from the substrate, sometimes referred to as the "skyhook-effect". Here, the same effect is observed when hydrogenating Co adatoms on the noble metal (111) surfaces. As a consequence, the migration barrier  $E_m$  for the thermal diffusion of the H-Co complexes is reduced.

Hydrogenated Co adsorbates are obtained by establishing a background pressure of  $10^{-8}$  mbar  $H_2$  during the evaporation of the cobalt. On the Ag(111) surface, this procedure results in 90% H-Co complexes that are easily distinguishable from the pure Co adatoms in STM topographs by their apparent height of  $\approx 0.6$  Å compared to  $\approx 0.8$  Å for the pure Co adatoms (Fig. 4.2), with similar results on the Cu(111) and the Au(111) surface (Fig. 5.7). The diffusion parameters  $E_m$  and  $\nu_0$  for the two kinds of adsorbates were determined as described above. To avoid relative errors in the temperature and other systematic errors, the measurement was done simultaneously for the two kinds of adsorbates by choosing a coverage of half Co and half H-Co adsorbates. As expected, the migration barrier  $E_m = 38 \pm 2$  meV of H-Co/Ag(111) is reduced by the skyhook effect with respect to  $E_m = 50 \pm 2$  meV of Co/Ag(111) (Fig. 4.1). The faster diffusion of the H-Co complexes on Ag(111) as compared to the Co adatoms at a substrate temperature of 11 K can be seen in a STM movie at:

[http://www.mpi-stuttgart.mpg.de/KERN/Res\\_act/supmat\\_3.html](http://www.mpi-stuttgart.mpg.de/KERN/Res_act/supmat_3.html)

The frames (55 nm  $\times$  55 nm, bias = 80 mV,  $I = 100$  pA,  $T = 16$  K, 130 s per frame) are topographs of the Ag(111) surface, the brighter spots are Co adatoms, the darker spots are H-Co adsorbates. The hopping rate data points in gray in Fig. 4.1 have been determined from this movie. Apart from the reduction of the migration barrier, also the attempt frequency is strongly reduced ( $\nu_0 = 2 \times 10^9$  Hz for H-Co/Ag(111) compared to  $\nu_0 \approx 10^{13 \pm 1}$  Hz for Co/Ag(111)) and falls well below the common value of  $\nu_0 = 10^{12-13}$  Hz (Fig. 4.1). The reason for this reduction might be the new elastic degree of freedom between the H and the Co which complicates the migration process of the H-Co complex. TST is not valid if several migration steps for a hopping event are relevant. The compensation effect is too weak to explain the strong reduction in  $\nu_0$ .

## 4.2 Surface-state mediated adsorbate interactions

Lateral adsorbate-adsorbate interactions have attracted theoretical [152] and experimental [38] interest since the 1970's. The interactions have several origins which can be divided according to the mutual adsorbate separation. At small interatomic distances *direct electronic interaction dominates leading to the formation of localized chemical*

bonds. This interaction falls off exponentially and is therefore of very short range. At larger separations adsorbate interactions are predominantly indirect and may be mediated in three ways: electrostatically (dipole-dipole) and elastically (deformation of substrate lattice), which both lead to non-oscillatory interactions which decay monotonically with separation  $r$  as  $1/r^3$  [153]. The third way of mediation, which is the subject of this chapter, is by substrate electrons leading to an oscillatory interaction energy: the adsorbates interact via Friedel oscillations through the fact that the binding energy of one adsorbate depends on the substrate electron density, which oscillates around the other. Such oscillatory interactions depend on adsorbate-adsorbate distance as  $\cos(2k_F r)/r^5$  for the density oscillations of a 3D electron gas at the surface of the substrate and as  $\cos(2k_F r)/r^2$  for a 2D electron gas [42].<sup>1</sup>

Hence the bulk (3D) electron mediated adsorbate interactions fall off much faster than the dipole-dipole and elastic interactions. The superposition of all three indirect interactions, dipole-dipole, elastic and bulk-electron mediated, leads to complicated behavior with high chemical specificity and a range never exceeding a few atomic distances. In contrast, for substrates with a surface-state band present at the Fermi level, the slow fall off of the interaction mediated by the 2DEG should lead to interactions of extreme long range. First experimental indication of long-range interactions, possibly mediated by surface-state Friedel oscillations, came from equidistant bulk segregated impurities on Cu(111) [43]. Quantitative interaction energies have first been reported by us [45,46] and by Repp *et al.* [44] for the system Cu/Cu(111). The results of ref. [44] clearly show the predicted oscillation period of  $\lambda_F^2/2$  and the  $1/r^2$ -decay for large distances. However, there are significant deviations from theory in the distance regime where the interactions are expected to be strongest, namely at  $r < 20$  Å. Quantitative experimental information down to short distances is crucial for two reasons. First, the interactions at these distances become sufficiently strong to delay nucleation and to stabilize an ordered superlattice of adsorbates. Second, experimental data on this length scale are important for comparison with theory since recent DFT-calculations [148,156,157] can now address this distance range, whereby they meet the validity range of scattering theory [158].

Here the disagreement with theory is removed for Cu/Cu(111) by careful analysis of the data in terms of two body interactions only. Furthermore, by investigating the interactions also for Co atoms on Ag(111), it is observed that the oscillation wave length changes according to the surface-state band structure of the respective substrate.

---

<sup>1</sup>Note that the asymptotic  $\cos(2k_F r)/r^5$ -decay of this reference only holds for isotropic Fermi-surfaces. In the general case, one must figure out which  $\mathbf{k}$ -vector along the Fermi surface to use. It is the one pointing in the direction of the interaction [154,155].

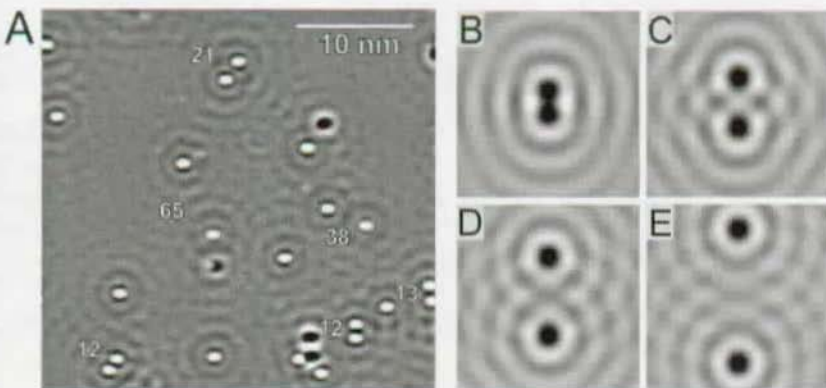


**Figure 4.3:** (A) STM topograph (100 mV bias) of Cu adatoms on the Cu(111) surface. The white dots are the Cu adatoms, the black dots are impurities of unknown chemical identity. The image was taken at 6 K after cooling down the sample from 19 K where the Cu adatoms were rapidly diffusing. The Cu adatoms are prevalently frozen close to certain distances  $r$  to each other which are favored by the oscillatory surface-state mediated interaction. The numbers in the image are the distances in Å of the adjacent adatoms pairs. The interaction is due to the oscillations in the surface-state electron density, which are imaged as concentric rings around the adatoms. The surface-state density patterns are reproduced by scattering theory calculations using Eq.(2.17) with full absorption ( $\alpha = \infty$ ) and  $s$ -wave scattering only: The maps (B)-(E) show the calculated surface-state density for two scattering centers with vertical separations  $r_n^{\min}$  corresponding to the  $n$ th interaction energy minima in Fig. 4.4(A): (B)  $r_1^{\min} = 12$  Å, (C)  $r_2^{\min} = 27$  Å, (D)  $r_3^{\min} = 42$  Å, and (E)  $r_5^{\min} = 72$  Å.

This unambiguously identifies the cause of the interaction as mediation by surface-state electrons. Comparing different adsorbates, Cu and Co atoms, on the same substrate, Cu(111), reveals the insensitivity to the adsorbate's chemical identity and suggests the general existence of long-range interactions on surface-state substrates.

The lateral adatom interaction is quantified by analyzing extensive STM time sequences in terms of site occupation probabilities as function of adatom distances. In order to focus on two body interactions only nearest neighbor  $nn$ -distances  $r$  are counted, i.e., a distance  $r$  from a selected atom to a nearby atom is counted only if no third scatterer (adatom or impurity) is closer than  $r$ . For the low adatom coverages ( $\Theta = 1 \times 10^{-3}$  ML) and the low defect densities ( $\Theta = 2 \times 10^{-4}$  ML) this is a good approximation to the idealized situation of two isolated, interacting adatoms.

A distance histogram  $f(r)$  obtained that way from an STM series recorded at 15.6 K (Fig. 4.4(A)) shows significant oscillatory deviations from random site occupation  $f_{\text{ran}}(r)$ , shown as full curve. One finds the following expression for  $f_{\text{ran}}(r)$  at coverage  $\Theta$ , image size  $L \times L$ , with  $N = L^2\Theta/A_{\text{unit-cell}}$  atoms per image, and a set of  $n$  images:

$$f_{\text{ran}}(r) = 2\pi r \Delta r n \frac{N^2}{L^2} \times \left(1 - \pi \frac{r^2}{L^2}\right)^N \times \frac{(\pi L^2 + (4 - \pi)r^2 - 4rL)}{\pi L^2}. \quad (4.3)$$

The first factor is the linearly increasing probability to find a pair of atoms being distance  $r$  apart (the width of the histogram classes is  $\Delta r$ ), the second factor accounting for the  $nn$ -statistic is the probability of finding such a pair with no third atom in the area  $\pi r^2$  around the first, and the third factor accounts in a good approximation for the finite rectangular image size. This function was tested successfully with kinetic Monte-Carlo simulations for statistical growth. Boltzmann statistics yields the differences in adatom binding energy

$$E(r) = -k_B T \ln \frac{f(r)}{f_{\text{ran}}(r)}. \quad (4.4)$$

The curve shown below the histogram in Fig. 4.4(A) is the result of an average of  $E(r)$ -curves obtained from histograms at various temperatures ( $14.3 < T < 16.2$  K). The reason to include a range of temperatures is that at higher  $T$ , the statistical independence of consecutive images is sufficient also for adsorbates mutually bound in the first profound minimum  $\tau_{\text{min}}^1$  of the interaction (Fig. 4.7), whereas the smaller energy variations in the tail of the interaction can better be studied at lower  $T$ .

The  $E(r)$ -curve for Cu/Cu(111) clearly shows oscillations in binding energy extending up to 60 Å. For  $r > 20$  Å,  $E(r)$  behaves as in ref. [44]. However, the data agrees with the scattering theory [158] way down to the first minimum in the interaction energy, where the study [44] found a decrease of the interaction strength. The low count rate

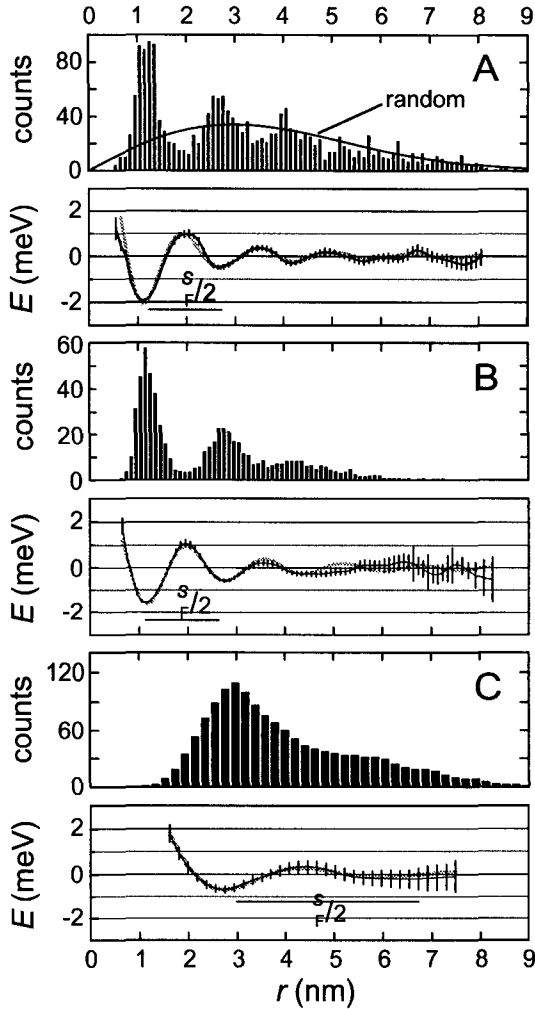


**Figure 4.4:**  $nm$ -distances histograms for (A) Cu/Cu(111) ( $\Theta = 1.4 \times 10^{-3}$  ML,  $T = 15.6$  K), (B) Co/Cu(111) ( $\Theta = 2 \times 10^{-3}$  ML,  $T = 10.2$  K) and (C) Co/Ag(111) ( $\Theta = 4 \times 10^{-4}$  ML,  $T = 18.5$  K) and pair interaction energies  $E(r)$  according to Eq. 4.4. Fits to the  $E(r)$  data according to Eq. 4.5 are shown as gray lines with  $r_0 = 10$  Å in (A), 14 Å in (B), and 3 Å in (C), respectively.



of adatoms separated by  $\approx r_{\min}^1$  of this study might be due to an insufficient statistical independence of consecutive STM images due to a too low coverage of adatoms at the spotted surface region: if the diffusion of the adatoms is not fast enough and the time between consecutive images is too short, the adatoms may not be able to get close to each other and may thus not probe their mutual interaction. Also, from the published histogram and from the number of distances analyzed, as well as from their formula for  $f_{\text{ran}}$ , it can be concluded that the authors of ref. [44] analyzed all interatomic distances and therefore included many-adatom interactions.

For a quantitative comparison with theory the asymptotic  $1/r^2$ -model by Hyldgaard *et al.* [158] is used, establishing a link of  $E(r)$  with the scattering properties of the adsorbates. The fit reveals good agreement between theory and experiment up to the second maximum of the interaction. For smaller  $r$ , the  $1/r^2$ -law predicts a deeper first minimum than the experimental data. To extend the model to small values of  $r$  a parameter  $r_0$  is introduced as follows:

$$E(r) = CE_{\text{F}} \left( \frac{2 \sin \delta_0}{\pi} \right)^2 \frac{\sin(2k_{\text{F}}r + 2\delta_0)}{(k_{\text{F}}r)^2 + (k_{\text{F}}r_0)^2}. \quad (4.5)$$

Fits to the experimental data are shown in Fig. 4.4. Note that similar values for the adsorbate's scattering phase  $\delta_0$  and for the wave vector  $k_{\text{F}}$  are obtained when fitting without  $r_0$  and starting from the second maximum of  $E(r)$ . The position of the first minimum determines the  $s$ -wave scattering phase  $\delta_0 = (0.50 \pm 0.07)\pi$  and a scattering amplitude of  $C = 0.13 \pm 0.01$ , which are in good agreement with the properties expected of a black-dot scatterer. The best fit is obtained with  $r_0 = 10 \text{ \AA}$ , meaning that the first minimum is slightly attenuated with respect to a  $1/r^2$  behavior, which may be indicative of the onset of repulsive interactions at short distances (see also Fig. 4.5). Notice, however, that the first minimum of  $E(r)$  is clearly more attractive than the second one in contrast to ref. [44]. The wave vector  $k = (0.20 \pm 0.01) \text{ \AA}^{-1}$  is in good agreement with Fermi surface-state wave vector  $k_{\text{F}}^s = 0.21 \text{ \AA}^{-1}$  of Cu(111) (Table 3.1).

For short distances, there is a strong repulsion  $E_{\text{max}}$  between the Cu adatoms, before they become bound as dimer at the distance of neighboring fcc sites (the dimer bond energy was calculated to be  $E_{\text{b}} = 520 \text{ meV}$  [159]). The repulsion is evidenced by the following observations permitting to establish lower bounds of  $E_{\text{max}}$  by comparison with KMC simulations: the absence of dimer formation at 16.5 K after 20 min observation time ( $\Theta = 1.4 \times 10^{-3} \text{ ML}$ , image size  $800 \times 800 \text{ \AA}^2$ ) yields  $E_{\text{max}} \geq 13 \text{ meV}$ . The observed absence of dimer formation, beyond the few ones expected from statistical growth, for deposition of  $3 \times 10^{-3} \text{ ML}$  at 19 K equally yields  $E_{\text{max}} \geq 13 \text{ meV}$ . From the observation of the onset of dimer formation at 19–21 K reported in ref. [44] one derives

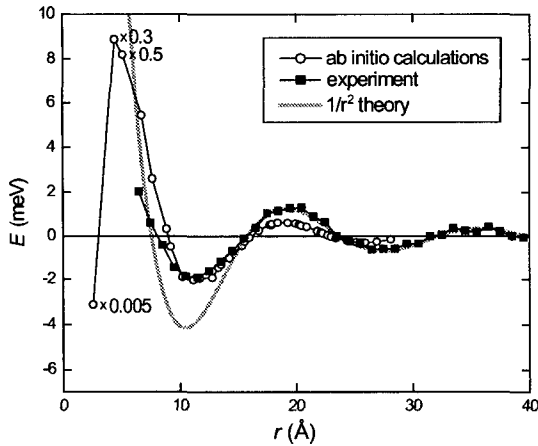


**Figure 4.5:** Comparison of *ab-initio* calculations [157] to the experimentally determined adsorbate-adsorbate interaction energies for Co on Cu(111). The gray line is a fit of the asymptotic  $1/r^2$ -law (Eq. (4.5) with  $r_0 := 0$ ) to the experimental data. The fit, starting at the second zero-crossing of  $E(r)$ , yields  $C = 0.104$ ,  $k = 0.192$ , and  $\delta_0 = 1.68$ .

22–28 meV as upper bounds for  $E_{\max}$  under the assumptions of  $\Theta = 3.0 \times 10^{-3}$  ML and that “onset of dimer formation” corresponds to 10 % of the monomers having formed dimers and trimers after 20 min time. In *ab-initio* calculations a slightly larger value of  $E_{\max} \approx 40$  meV has been reported [148]. For reasons of scale on the energy axis this short-range repulsion is not included in Fig. 4.4. For systems where  $E_{\max}$  is of the order of  $E_m$ , the interaction is of importance in delaying nucleation to much higher coverages than in classical nucleation and growth scenarios [148, 156, 160], which can explain the small apparent diffusion prefactors systematically deduced for systems with small barriers  $E_m$  [159, 160].

To investigate how the long-range interactions relate to the adsorbate’s chemical nature, pair correlations are in the following explored in the very same way as for Cu also for Co adatoms on Cu(111) (Fig. 4.4(B)). The results are within error bars identical to Cu/Cu(111):  $\delta_0 = (0.49 \pm 0.03)\pi$ ,  $C = 0.12 \pm 0.01$ , and  $k_F = (0.20 \pm 0.01) \text{ \AA}^{-1}$ , and the interaction decays again as  $1/r^2$ . This suggests the generality of surface-state mediated interactions between adsorbates. The interaction energies determined here for Co adatoms on the Cu(111) surface are in good agreement with recent *ab-initio* calculations based on the density functional theory and multiple-scattering theory using the Korringa-Kohn-Rostoker Green’s function method for low-dimensional systems [157].

The agreement is remarkable considering the minute values of the interaction compared to the binding energies and the statistical experimental method used (Fig. 4.5).

To unequivocally prove the electronic origin of the interaction, its period for Co on Ag(111) is investigated, which has a different surface-state band structure resulting in an expected  $E(r)$  period of  $\lambda_F^s/2 = 38 \text{ \AA}$  [27]. In agreement, the wave length of the interactions is more than twice as long as for Cu(111), as is evident from the  $E(r)$ -curve (Fig. 4.4(C)), the fit yields  $\delta_0 = (0.33 \pm 0.02)\pi$  and  $k_F = (0.10 \pm 0.02) \text{ \AA}^{-1}$  in agreement with  $k_F^s = 0.083 \text{ \AA}^{-1}$ . Co atoms repel each other for  $r < 20 \text{ \AA}$  and the first minimum in interaction energy is at around  $27 \text{ \AA}$ . The absolute values for  $E(r)$  are much smaller than for Cu and Co on Cu(111). This can be attributed to the lower total electron density in the surface-state of Ag(111) as compared to Cu(111) (Table 3.1).

### 4.3 Long-range order

Let us now turn to an important implication of the observed long-range interactions: they may lead to “superstructures” and long-range order between molecular and atomic adsorbates which might be exploited in manifold ways [161]. For system with a low migration barrier as the ones studied here, the effects of the interaction on the mutual adsorbate distances can directly be observed during the diffusion process at low temperatures over a wide range of hopping rates. But even for systems with higher migration barriers, the interaction will influence the mutual adsorbate distances if the adsorbate have enough time to thermally equilibrate at low temperatures. Thus, not too high migration barriers should not impede the formation of stable long-range ordered structures if the adsorbates are frozen slowly. This has been demonstrated by the distance distribution at room temperature of non-diffusing adatoms on Cu(111) [43] (probably sulfur adatoms with a relatively high migration barrier  $E_m \approx 200 \text{ meV}$  [162]), which have been segregated from the bulk by annealing the sample to 900 K. We have tried to grow superstructures of adsorbates by depositing an increasing coverage of adsorbates onto the substrates at temperatures where the adsorbates diffuse, but are not able to overcome the repulsion  $E_{\max}$  to form dimers. For low coverages ( $\approx 10^{-3} \text{ ML}$ ), an often found structure are curved chains of adsorbates with a  $nn$ -distance of the first minimum  $r_1^{\min}$  of the interaction energy (Fig. 4.6(A,C)). Such chains are energetically favorable because for a scattering phase shift of  $\pi/2$ , the second nearest neighbor distance falls within the second minimum of the pair interaction energy (Fig. 4.7). In principle, additional to the pair interaction studied so far, for structures of more then two adsorbates interactions produced by interference of electrons which propagate the entire superstructure have to

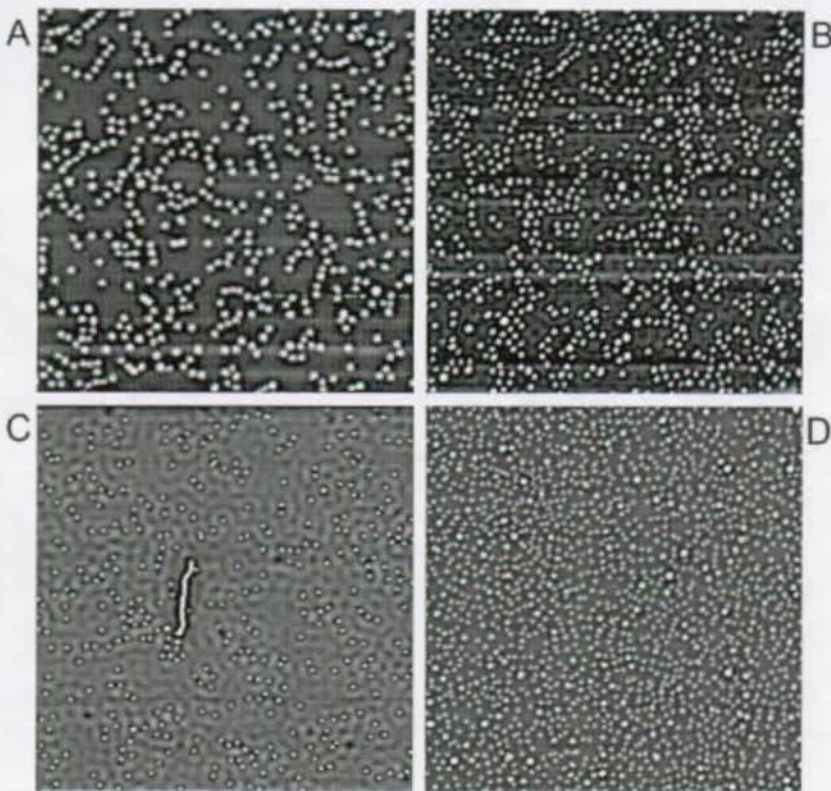


**Figure 4.6:** Attempts to create ordered superlattices. The small white dots are Co adatoms, larger white spots are first nucleations of islands. The scattering phase of  $\delta_0 \approx \pi/2$  favors atomic chains but disfavors hexagonal lattices **(A)-(B)** Co/Cu(111) with  $\Theta = 0.005$  ML in **(A)** and  $\Theta = 0.021$  ML in **(B)** ( $50 \text{ nm} \times 50 \text{ nm}$ ,  $T_{\text{ads}} = 19 \text{ K}$ ). **(C)-(D)** Co/Ag(111) with  $\Theta = 0.003$  ML in **(C)** and  $\Theta = 0.012$  ML in **(D)**. For Co/Ag(111) the interactions are about 3 times weaker ( $100 \text{ nm} \times 100 \text{ nm}$ ,  $T_{\text{ads}} = 19 \text{ K}$ ). (The white line in **(C)** is from an adsorbate dragged along the surface by the tip.)

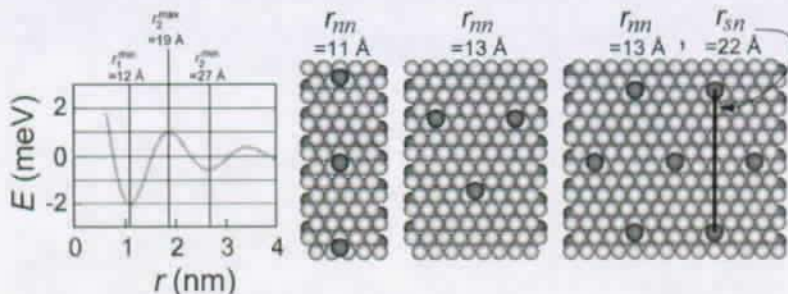


**Figure 4.7:** Some possible adsorbate "super-structures" on Cu(111) with adsorbate-adsorbate  $nn$ -distances  $r_{nn}$  approximately equal to the first minimum distance  $r_1^{\min}$  of the pair interaction energy of the surface-state mediated interaction.  $r_{\min}^1$  is the first minimum of the long-range interaction energy apart from the minimum of dimer formation.  $r_{sn}$  is the second-nearest-neighbor adsorbate-adsorbate distance.

be considered. But, as recently shown for three adsorbates [163, 164], trio interactions are weak (about one fourth of the pair interaction strength) and they fall off with the adsorbate distances faster than the pair interactions. Even though equilateral triangles of three adsorbates with a  $nn$ -distance of  $r_1^{\min}$  are energetically favorable, only few are observed (Fig. 4.6(A,C)). The reason might be that they are less likely to form in the diffusion process: a third adsorbate approaching a pair of adsorbates which are separated by  $r_1^{\min}$ , has to overcome the second maximum of the interaction with the other two adsorbates in order to reach the favorable distance where it is separated from the two other adsorbates by  $r_1^{\min}$ . For the formation of hexagonal units and superlattices, the oscillating character of the interaction has to be considered. For example, for a lattice constant given by  $r_1^{\min}$ , the  $\sqrt{3} \times r_1^{\min}$ -distance appearing as second-nearest-neighbor distance  $r_{sn}$  in a hexagonal lattice falls close to the second maximum of the pair interaction energy if the scattering phase shift is close to  $\pi/2$  (Fig. 4.7). Another point to consider is that the lattice of adsorbing sites offered by the underlying substrate lattice might not match with the distances of the minima of the interaction, especially for sharp minima when  $\lambda_F^*/2$  is not much larger than the lattice constant of the substrate.

## 4.4 Summary

In summary to this chapter, the potential landscapes of adatoms on the three noble metal (111) surfaces have been investigated. For isolated adsorbates, the migration bar-

rier  $E_m$  to neighboring fcc sites has been determined ( $E_m = 50$  meV for Co/Ag(111) and  $E_m = 40$  meV for Cu/Cu(111)) by direct observation of the adsorbates' hopping rates at different temperatures. The  $E_m$  values are in good agreement with theory [148]. Weak, long-range modulations of the potential landscapes due to adsorbate-adsorbate interactions for low adsorbate coverage have been quantified by the analysis of the distribution of nearest-neighbor adsorbate distances. Using this statistical method, we have been able to determine oscillating pair-interaction energies  $E(r)$  in the meV range for Cu on Cu(111) and Co on Cu(111) and Ag(111) up to distances of 60 Å. The mediation of these long-range adsorbate-adsorbate interactions by Friedel oscillations of the surface-state electron charge density expresses itself in the link of the oscillation period  $\lambda$  of the interaction energy with the surface-state Fermi-vector as  $\lambda/2 = \pi/k_F^s$ . This relationship was demonstrated for Co on Cu(111) and Ag(111), which have very different  $k_F^s$ , clearly excluding a mediation of the interaction by other means like elastic lattice deformation. Comparison between Co and Cu adatoms on Cu(111) shows within the error margin similar  $E(r)$ -curves, suggesting only little effect of the adsorbate's chemical identity on  $E(r)$ . Thus, as opposed to short-range interactions the surface-state mediated interactions are far less adatom specific and therefore of general significance since they predominantly reflect the surface-state band structure. The  $E(r)$  data enable quantitative comparison with theory; the short range data agree reasonably well with recent *ab-initio* results [148,157], in the long range the theory of Lau and Kohn and the scattering model derived from it by Hyldgaard and Persson have been confirmed: The interaction decays asymptotically as  $1/r^2$  and scales with the density of surface-state electrons. The Fermi energy phase shifts of the surface-state electrons scattering at the adatoms are all close to  $\pi/2$ , which is the value expected for black dot scattering. For the systems investigated here, there is a significant short-range repulsion superimposed on the oscillatory long-range interactions, which acts as attachment barrier and delays island formation. A lower bound of this repulsion has been determined from the absence of dimer formation at higher temperatures during the observation period. The adsorbate-adsorbate interactions can potentially be employed for the creation of superstructures like ordered atomic and molecular lattices. In the symmetry of such structures the adsorbate's scattering phase, the favorable adsorption sites offered by the substrate and presumably also trio and higher order interactions play a role. We observe chains of adatoms with nearest neighbor distance about equal to the distance of the first minimum of the pair interaction.



## Chapter 5

# Kondo resonance of single magnetic adsorbates on noble metal surfaces

### 5.1 The Anderson model

Many aspects of the interaction of a localized moment of a chemisorbed magnetic adsorbate with the conduction electrons of a metal substrate can be understood within the Anderson model [48,95,165]. The Anderson model, also called interacting resonant level model, adds to the phenomenological parameters of the RLM discussed in Section 2.3.1 a short range intrasite interaction energy term  $U$  for the coulomb repulsion of two electrons within the localized adsorbate level:

$$U = \int \Phi_a^*(\mathbf{r}) \Phi_a^*(\mathbf{r}') \frac{e^2}{|\mathbf{r} - \mathbf{r}'|} \Phi_a(\mathbf{r}) \Phi_a(\mathbf{r}') d\mathbf{r} d\mathbf{r}'. \quad (5.1)$$

$U$  usually ranges from 1 – 10 eV for 3d and 4f electrons in an impurity or adsorbate in a metallic environment. The Anderson Hamiltonian reads, in the single-orbital second-quantized form under consideration of the electron spin  $\sigma$ :

$$H = \sum_{\mathbf{k},\sigma} E_{\mathbf{k}} n_{\mathbf{k},\sigma} + \sum_{\sigma} E_a n_{a,\sigma} + \sum_{\mathbf{k},\sigma} [V_{\mathbf{k}a} c_{\mathbf{k},\sigma}^\dagger c_{a,\sigma} + V_{\mathbf{k}a}^* c_{a,\sigma}^\dagger c_{\mathbf{k},\sigma}] + U n_{a,\uparrow} n_{a,\downarrow}. \quad (5.2)$$

Whereas the RLM Hamiltonian can in principle be diagonalized to an independent electron Hamiltonian, the additional coulomb term in the Anderson model introduces subtle many-body correlation.

For  $U = 0$  and  $E_a < E_F$ , the ground state of the system is non-magnetic with a double occupied adsorbate level. In the following, the local moment parameter regime (also called Kondo regime) is discussed, where  $E_a < E_F$  and  $E_a + U > E_F$  (Fig. 5.1). For  $V_{\mathbf{k}a} = 0$ , the localized state is decoupled from the conduction electrons and will be single



occupied with a spin  $\sigma = \uparrow, \downarrow$ . The corresponding ground state has two-fold degeneracy corresponding to spin 1/2 with an associated magnetic moment. For non-zero  $V_{\mathbf{k}a}$ , the localized state and the conduction states are mixed.

The hybridization broadens the discrete energy of the localized state to spin-split resonances of width  $\Gamma = 2\pi \sum_{\mathbf{k}} |V_{\mathbf{k}a}|^2 \delta(E - E_{\mathbf{k}})$  (as seen in Section 2.3.2) at  $\approx E_a$  and  $\approx E_a + U$ , thereby equalizing spin up and spin down occupancies of the localized level. Thus, stronger hybridization favors a non magnetic ground state, in competition to the  $U$  term, which favors an unbalanced occupation of the localized level, i.e. a magnetic ground state. The local moment survives for  $|E_a + U - E_F|, |E_F - E_a| \gg \Gamma$ . The moment has an antiferromagnetic exchange interaction with the conduction electrons: the exchange interaction originates in lowest order in  $V_{\mathbf{k}a}$  from virtual excitations from the  $n_a = 1$  ground state to the  $n_a = 2$  and the  $n_a = 0$  subspaces (Fig. 5.1). It can be shown that the Anderson model is equivalent to a Heisenberg type model (called *s-d-model*)

$$H_{sd} = \sum_{\mathbf{k}, \mathbf{k}'} J_{\mathbf{k}, \mathbf{k}'} (S^+ c_{\mathbf{k}, \downarrow}^\dagger c_{\mathbf{k}', \uparrow} + S^- c_{\mathbf{k}, \uparrow}^\dagger c_{\mathbf{k}', \downarrow} + S_z (c_{\mathbf{k}, \uparrow}^\dagger c_{\mathbf{k}', \uparrow} - c_{\mathbf{k}, \downarrow}^\dagger c_{\mathbf{k}', \downarrow})), \quad (5.3)$$

where  $S_z$  and  $S^\pm = S_x \pm iS_y$  are the spin operators for the localized state of spin  $S$ . The effective exchange coupling  $J_{\mathbf{k}, \mathbf{k}'}$  is given by [166]

$$\begin{aligned} J_{\mathbf{k}, \mathbf{k}'} &= V_{\mathbf{k}a}^* V_{\mathbf{k}'a} \left[ \frac{1}{U + E_a - E_{\mathbf{k}'}} + \frac{1}{E_{\mathbf{k}} - E_a} \right] \\ &\stackrel{E_{\mathbf{k}} \approx E_F}{=} \frac{\Gamma}{2\pi n_0} \left[ \frac{1}{U + E_a} + \frac{1}{-E_a} \right], \end{aligned} \quad (5.4)$$

with the Fermi level energy set equal to zero. In the local moment regime,  $E_a + U > E_F$  and  $E_a < E_F$ , the exchange is antiferromagnetic,  $J > 0$ , for scattering of conduction electrons in the region of the Fermi level.

The spin exchange qualitatively changes the energy spectrum of the system. When many such processes are taken together, one finds that a new state, a weakly bound non-magnetic many-body singlet ground state is generated with about the same energy as the Fermi level. This Kondo ground state is unusual for it is generated by exchange processes between a localized electron and free electron states. The preserved magnetic moment of the localized level is completely compensated by the spins of the conduction electrons. In contrast to the static screening of a firmly aligned magnetic moment by static RKKY-oscillations, the spin-density correlations of the adsorbate spin to the conduction electron spins are lost after the spin-flip time  $\tau_K = \hbar/(k_B T_K)$ . The many electrons that are involved in the spin-flip processes combine to build the Kondo resonance, which has a very small weight in the LDOS  $\rho_a(E)$  (Fig. 5.1). The so-called Kondo cloud consists

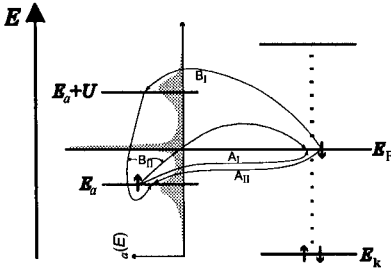


**Figure 5.1:** Schematic energy representation of the single-orbit Anderson model in the magnetic moment regime. Spin flip processes are indicated by arrows. In process A, the zero occupation  $n_a = 0$  subspaces is virtually excited, in process B, the double occupation  $n_a = 2$ . Note that this is no independent electron scheme, i.e. the energy of an electron in the adsorbate orbit depends on its occupation.

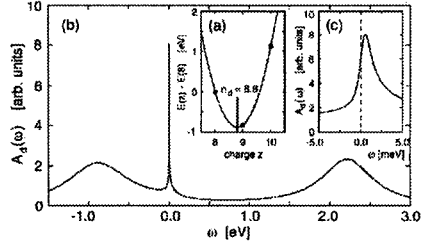


**Figure 5.2:** (A) The average 3d orbital electron occupation of a Co adatom on the Au(111) surface is  $n_a = 8.8$ . (B) Calculated LDOS of the Co adatom's  $d$ -orbital from an effective  $n_a = 8, 9, 10$  spin-1/2 Anderson model. (C) The Kondo resonance near  $E_F$  is slightly shifted above the Fermi energy due to level repulsion. (Figure from Ref. [167]).

of electrons that have previously interacted with the same magnetic impurity. Since each of these electrons contains information about the same impurity, they are mutually correlated. The size of the Kondo cloud is given by the distance  $\xi_K \approx v_F \tau_K$  the electrons with the Fermi velocity of  $v_F = \hbar k_F / m^*$  can travel during the spin-flip time  $\tau_K$ . No experiment has ever directly detected the size of the Kondo cloud, probably due to the large values of  $\xi_K \approx 100$  nm for typical Kondo systems.

The behavior of the Anderson model in the low temperature range can be understood in terms of interacting quasi-particles within a Fermi liquid theory [48]. The quasi-particles can be described by an Anderson model with a renormalized hybridization  $\tilde{V}$ , intrasite interaction term  $\tilde{U}$  and energy  $\tilde{E}_a$ . The renormalized Anderson Hamiltonian describes quasi-particle excitations from the interacting many-body singlet ground state. The quasi-particle density of states  $\rho_a(E)$  corresponds to a resonance of width  $k_B T_K$  close to the Fermi level, the Kondo resonance. If the weak interquasi-particle interaction is ignored,  $\tilde{U} \approx 0$ , the model for the quasi-particle becomes a RLM which qualitatively describes the correct low  $T$  behavior. The situation is then similar to the single particle description of an impurity with a narrow virtual bound state of width of order of  $k_B T_K$  at the Fermi level. Thus, in the low temperature limit  $T \ll T_K$  the magnetically

screened impurity scatters the conduction electrons like a non-magnetic impurity with a resonance at the Fermi level with an energy width of order of  $k_B T_K$  [168]. The Kondo temperature  $T_K$  is given by [169]

$$\begin{aligned} T_K &= \frac{\sqrt{\Gamma U}}{2} e^{\frac{\pi E_a(E_a+U)}{\Gamma U}} \\ &= T_0 e^{-\frac{1}{2n_0 J}}, \end{aligned} \quad (5.5)$$

where  $T_0 = W\sqrt{\Gamma/(\pi W)}$  and  $W$  is the conduction electron band width.

The degeneracy of the  $3d$  and  $4f$  orbitals of magnetic atoms is taken into account by the degenerate Anderson model, also called ionic model [48]. Usually, for a magnetic adatom, the orbital degeneracy is lifted due to crystal field splitting and the configurations with different numbers of electrons are separated by an energy of order of  $U$ . It is then sufficient to consider only fluctuations between the three lowest configurations, the ground state configuration and the configurations with one electron more and one electron less. This leads to an effective non-degenerate Anderson model. For Co on Au(111), the average  $3d$  orbital electron occupation is  $n_a = 8.8$  (Fig. 5.2(A)) as determined from the semirelativistic, screened Korringa-Kohn-Rostoker method in combination with the local spin-density approximation [167]. The lowering of the Co  $d$ -levels leading to the higher occupancy compared to  $n_a = 7$  of an isolated Co atom is mainly due to hybridization with the conduction electrons. The excess charge of the Co adatom is compensated by a positive conduction electron depletion cloud. The LDOS of the Co  $3d$ -orbital shown in Fig. 5.2(B) has been calculated with an effective spin-1/2 Anderson model considering only the  $n_a = 8, 9, 10$  configurations.

The Kondo resonance in the LDOS of the local orbital affects the conductivity of the conduction electrons. Therefore, it is obvious that the Kondo resonance can be examined by measuring the tunneling conductance with the tip placed close to a magnetic adsorbate. From the analysis of the tunneling spectra, the Kondo temperature for example can be determined with a much higher accuracy than previously possible. In the following, tunneling spectra taken close to a magnetic adsorbate are analyzed in the framework of two competing tunneling channels: For  $T \ll T_K$ , local Fermi liquid theory can be applied and the Kondo resonance in the LDOS of the  $d$ -level has a Lorentzian shape [48, 167] (Fig. 5.2). Tunneling into this LDOS, which is hardly accessible due to the strong localization of the  $3d$ -orbital at the atomic core, makes up only one part of the tunneling current; the other part is from tunneling into the conduction electron LDOS of the substrate modified by the presence of the Kondo impurity. These two tunneling channels interfere as described in Section 2.3.4 and the resulting tunneling LDOS, which is proportional to the measured  $dI/dV$  signal, has a Fano line shape. The

tunneling conductance close to zero bias is

$$dI(r_{ta}, V)/dV = \text{const.} + a(r_{ta}) \frac{q(r_{ta})^2 - 1 + 2q(r_{ta})\epsilon}{\epsilon^2 + 1}, \quad (5.6)$$

with  $\epsilon = (eV + \Delta E)/k_B T_K$ . The constant is the background  $dI/dV$  signal and  $\Delta E$  a small shift of the resonance from the Fermi energy due to level repulsion between the  $d$ -level and the Kondo resonance. The Fano line shape parameter  $q$  is given by [98]

$$q(r_{ta}) = \frac{\text{Re } G_c(r_{ta}) + D(r_{ta})}{\text{Im } G_c(r_{ta})}, \quad (5.7)$$

where  $D(\mathbf{r}_t) = D_0 e^{-d_{ta}(\mathbf{r}_t)/\alpha}$ , and  $D_0$  is a constant dependent on the strength of the coupling of the conduction states to the adsorbate and the tip.  $\alpha$  is a decay length and  $d_{ta}$  the overall tip-adatom distance,  $G_c(r_{ta})$  a modified Green's function of the unperturbed conduction electron as seen by the tip [98].  $D(r_{ta})$  depends on the overlap of the tip wave function with this state and will fall off rapidly with  $r_{ta}$ . With  $q(r_{ta})$  defined as in Eq. (5.7),  $a(r_{ta})$  is proportional to  $(\text{Im } G_c(r_{ta}))^2$  (see Eq. (5.6)). Even for  $D = 0$ , i.e. no direct tunneling into the localized state, different Fano line shapes can result due to the first part of  $q(r_{ta})$ ,  $\text{Re } G_c/\text{Im } G_c$ , which describes an indirect tunneling from the tip to the adsorbate by conduction electron propagation. For free conduction electrons, this first part gives rise to rapid oscillations of  $q(r)$  between asymmetric Fano and symmetric Lorentzian line shapes with a period of  $\pi/k_F$  (for example,  $\pi/k_F^b \approx 2 \text{ \AA}$  for the free bulk electrons (Table 3.1)) [167, 170]. But these oscillation are not resolved by the STM in the usual spectroscopic tunneling conditions with the tip about  $5 \text{ \AA} < z_t < 10 \text{ \AA}$  above the surface. By modelling the host metal electrons with a jellium model, the oscillations in  $G_c$  are found to be lost for  $z_t > 5 \text{ \AA}$  [98]. For true conduction electrons of a real band structure, the  $q(r_{ta})$  behavior may be much more complicated. To study the spatial decay of the Fano resonances, we further define the overall amplitude  $A$  of Eq. (5.6) as the distance from the lower minimum of the Fano curve to the upper maximum

$$A(r_{ta}) = a(r_{ta}) (1 + q(r_{ta})^2). \quad (5.8)$$

## 5.2 Kondo resonance of single Co adatoms on Cu surfaces

The Fano line shaped [93] tunneling spectra taken with the STM tip positioned on top of magnetic adatoms have been interpreted by an interference of two tunneling channels, one direct channel through the resonance localized on the magnetic impurity and another

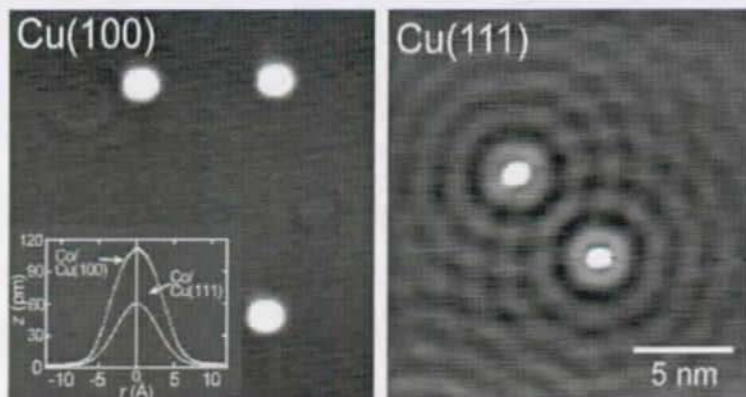


**Figure 5.3:** Constant current STM images ( $-50$  mV bias,  $I = 2$  nA) of Co adatoms on the Cu(100) (3 atoms) and the Cu(111) surface (2 atoms). The Friedel oscillations of the Cu(111) surface-state electrons can be easily detected up to  $10$  nm. The inset compares line cuts in the  $z$  signal over the adatoms on the two different surfaces for typical tip conditions.

channel into the conduction band of the substrate, but questions remain about the strength of the direct channel and the spatial changes of the Fano line shapes [167, 170]. Also, so far predominantly systems with a surface-state present at the Fermi energy have been investigated [9, 10, 52, 53], yet the role of the surface-state electrons in the Kondo resonance needs to be examined. In this section these questions are addressed by a comparative study of the interaction of Co adatoms with the conduction band electrons of the Cu(100) and (111) surfaces. The spatially resolved STS measurements of individual adatoms are quantitatively analyzed at and in the vicinity of isolated Co adatoms with the model of Plihal and Gadzuk [98]. In both systems, the Kondo resonance is detectable only within  $10$  Å of lateral tip-adatom distance  $r_{\text{ta}}$ , signifying an inferior role of the Cu(111) surface-state in the formation of the Kondo resonance. The  $r_{\text{ta}}$  dependance of the line shape and amplitude of the tunneling spectra reveals that direct tunneling into the localized state is negligible for Cu(111) but important for Cu(100). It is further demonstrated the correlation of the Kondo temperature  $T_K$  with the host electron density at the magnetic impurity.

The tip apex wavefunction was modified by gently dipping the tip into the substrate ( $\approx 1$  nm) until the Co adatoms are imaged spherically and the  $dI(V)/dV$  spectra on the bare surface have no sharp features near zero bias. This way the tip apex wavefunction is symmetric and optimized for spectroscopy at the expense of high spatial resolution (i.e. minimizing the radius of the tip apex wavefunction). Tips prepared in this way

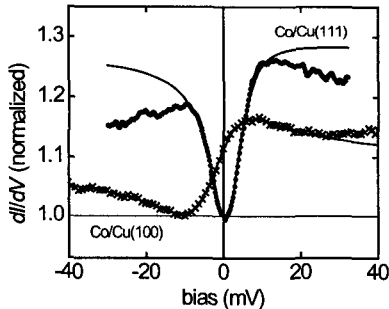


**Figure 5.4:** On atom differential conductance ( $dI/dV$ ) spectra for Co/Cu(100) and Co/Cu(111). The tunneling resistance was  $10\text{ M}\Omega$ . The spectra are normalized to their lowest values. The solid lines are Fano line shape fits according to Eq. (5.6), average parameters are summarized in Table 5.1.

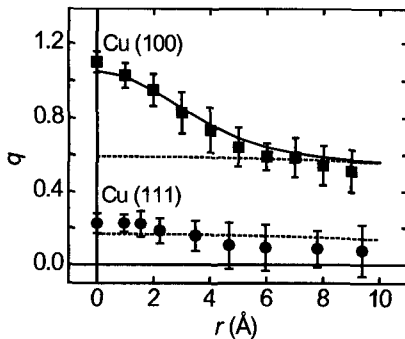


**Figure 5.5:** Spatial dependence of the Fano line shape parameter  $q(r_{ta})$  for Co/Cu(100) and Co/Cu(111). Each data set presents averaged values from measurements on four atoms. The dotted lines are from calculations with no direct tunneling into the localized state, for the solid line  $D(r_{ta})$  was fitted as described in the text.

reproducibly image the Co adatoms as bumps in the constant current images  $\approx 1.1\text{ \AA}$  and  $\approx 0.6\text{ \AA}$  high with a diameter (FWHM) of  $\approx 8\text{ \AA}$  and  $\approx 6\text{ \AA}$  for Co on Cu(100) and Cu(111), respectively (Fig. 5.3). Co on Cu(100) and (111) are Kondo systems characterized by Fano type scanning tunneling spectra near  $E_F$  (Fig. 5.4). Eq. (5.6) is fitted to on-atom ( $r_{ta} = 0$ )  $dI(V)/dV$  curves taken on different adatoms and with different tip structures. Prior to fitting, the  $dI(V)/dV$  curves are normalized to their minimal value. The form of the spectra did not change for different tunneling resistances in the range of  $0.2\text{ M}\Omega$  to  $100\text{ M}\Omega$ . Average Fano line shape parameters from fitting 10 different on-atom differential conductance spectra for Co on Cu(100) and (111) are summarized in Table 5.1. The Kondo temperatures are  $T_K = (88 \pm 4)\text{ K}$  and  $(54 \pm 2)\text{ K}$  for Co on the Cu(100) and (111) surface, respectively. The Cu(111) value is in very good agreement with the  $T_K$  value of  $(53 \pm 5)\text{ K}$  reported by Manoharan *et al.* [52].

The Kondo problem is essentially determined by only one relevant energy scale,  $k_B T_K$ . Once the Kondo temperature is known, predictions for all relevant physical observables can be made, e.g.  $T_K$  determines the parameters  $U$ ,  $E_d$  and  $\Gamma$  of the Anderson model. The Kondo temperature itself should depend only on the strength of the exchange coupling  $J$  and the density of the conduction electron states  $n_0$  at the magnetic

	Co/Cu(111)	Co/Cu(100)	Co in bulk
$T_K$ (K)	$54 \pm 2$	$88 \pm 4$	$\sim 500$ [165]
	$53 \pm 5$ [52]		
$n$	3	4	12
$q$	$0.18 \pm 0.03$	$1.13 \pm 0.06$	
$\Delta E$ (meV)	$1.8 \pm 0.6$	$-1.3 \pm 0.4$	

**Table 5.1:** Mean Fano line shape parameters and Kondo temperatures  $T_K$  from fits of Eq. (5.6) to scanning tunneling spectra of 10 different Co adatoms on Cu(100) and (111).  $n$  is the number of nearest neighbor Cu atoms.

impurity [48] (see Eq. 5.5). The increase in  $T_K$  from Cu(111) to Cu(100) to bulk Cu (see Table 5.1) is due to an increase in  $Jn_0$  which is in turn related to an increase of the number of nearest neighbor Cu atoms  $n$ . From atomic resolution images for Co/Cu(100), the Co adatom site is determined to be the four fold hollow site ( $n = 4$ ), for Co/Cu(111) the adsorption site is known to be the three fold hollow site [46], i.e.  $n = 3$ . We find that the logarithm of the Kondo temperature falls off linear with  $n$ . A fit of  $T_K$  to Eq. (5.5) under the assumption of  $Jn_0 \sim n$  and a constant  $T_0$  yields  $T_0 = 10^{3.00 \pm 0.12}$  K and  $Jn_0 = (0.055 \pm 0.007)n$ .

We now turn to the influence of the surface-state electrons on the Kondo resonance. To this end the change of the Fano resonances with the in-plane tip-adatom distance  $r_{ta}$  has been investigated by scanning over the adatoms and taking tunneling spectra for different  $r_{ta}$ .  $q(r_{ta})$  and  $A(r_{ta})$ , as determined from fits of Eq. (5.6) to spectra taken on four different Co adatoms on Cu(111) and Cu(100), are shown in Figs. 5.5 and 5.6. The errors are due to different tip structures, variations for different adatoms and noise in the  $dI/dV$  signal for larger  $r_{ta}$ . For both systems, as well as for Co on Ag(111) and Au(111), the Kondo spectra are only detectable for  $r_{ta} < 10$  Å (Fig. 5.6). The similar decay of  $A(r_{ta})$  clearly indicates that the Cu(111) surface-state does not significantly contribute to the formation of the Kondo resonance: Due to their 2D character,  $A(r_{ta})$  for the surface-state electrons should fall off only with  $1/r_{ta}$ , whereas  $A(r_{ta})$  for the bulk electrons falls off as  $1/r_{ta}^2$  or even faster due to band structure effects [98]. On the bare Cu(111) surface, about 2/3 of the current tunnels into the surface-state. This can be seen from the corresponding increase of the  $dI/dV$  signal at the onset ( $-440$  mV) of the Cu(111) surface-state similar to the onset on Ag(111) in Fig. 3.4. But it is known that close to strongly bound adsorbates, the tunneling channel into the surface-state is lost: the surface-state onset can no longer be detected on the adsorbate and the adsorbates Friedel oscillations of the surface-state are those of a highly absorbing (black

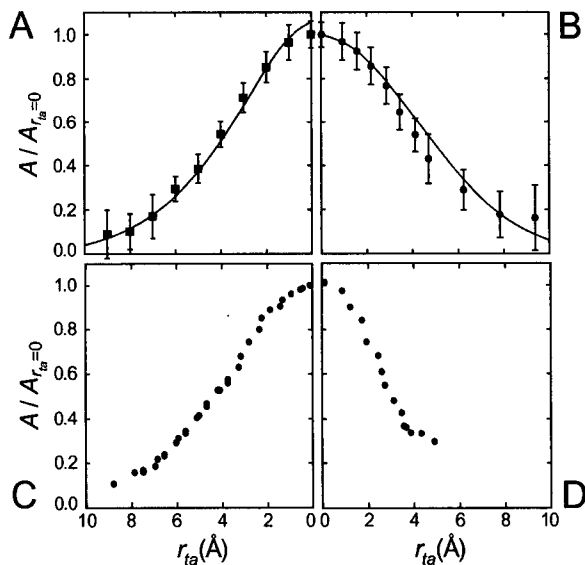


**Figure 5.6:** Spatial dependence of the normalized amplitude of the Fano resonance  $A(r_{ta})/A(0)$  on the in plane tip-adatom distance  $r_{ta}$  for (A) Co/Cu(100) and (B) Co/Cu(111). Each data set presents averaged values from measurements on four atoms. The solid lines are from model calculations described in the text. Similar spatial decays of  $A$  are found for (C) Co/Ag(111) and (D) Co/Au(111).



dot) scatterer [171–173], as also presumed in the previous chapter from the phase shift of the adsorbate-adsorbate interaction energy. The surface-state electrons thus scatter into bulk states at the Co adatoms [171] which can explain why their share in the Kondo resonance is below the experimental resolution. That they are not entirely uninvolved was demonstrated by Manoharan *et al.* [52, 172] in an ellipse corral experiment where a Fano spectrum was found in one focus about 8 nm away from the Co adatom in the other focus. In agreement with a weak surface-state contribution to the Kondo resonance, the spectrum in the empty focus was strongly diminished and only detectable for ellipse corrals formed in a way that the Fermi energy surface-state density at the adatom is enhanced. Weak traces of the Kondo resonance of Co with the Ag(111) surface-state electrons have also been found by investigating the dependence of the amplitude of the standing Friedel surface-state electron density oscillations on the bias for biases close zero [59].

Whereas  $q(r_{ta})$  for Co/Cu(111) keeps its small on-atom value  $q(0)$  within the error,  $q(r_{ta})$  for Co/Cu(100) falls off strongly within  $r_{ta} < 6 \text{ \AA}$  (Fig. 5.5). In both systems no oscillations in  $q(r_{ta})$  are observed as expected for tip distances  $z_t > 5 \text{ \AA}$  [98]. Accordingly, the difference in the spatial behavior of the asymmetry in the Fano line shape can be ascribed to substantial differences in the relative weight of the two competing tunneling channels for the two surfaces. In order to analyze the contribution of the tunneling channels into the resonance localized on the Co adatom and into the Cu substrate states quantitatively,  $A(r_{ta})$  and  $q(r_{ta})$  are modelled with a jellium model for  $G_c(r_{ta})$  under consideration of the tip-surface distance  $z_t$  according to a recent model by Plihal and Gadzuk [98]. This is done by first fitting  $(\text{Im } G_c(r_{ta}))^2$  to the measured  $a(r_{ta})$ . Then,  $\text{Re } G_c(r_{ta}) + D(r_{ta})$  is fitted to  $\text{Im } G_c(r_{ta})$  times the measured  $q(r_{ta})$  (see Eq. (5.7)). In the case of Co/Cu(111), this can be done with  $D(r_{ta}) = 0$ . In contrast, in the case of Co/Cu(100), the direct channel  $D(r_{ta})$  has to be considered to describe the measured  $q(r_{ta})$ . With the decay constant  $\alpha = 0.75 \text{ \AA}$  [98],  $D_0 = 170$  and  $z_t = 9.1 \text{ \AA}$ . The calculated  $q(r_{ta})$ , with and without the direct tunneling channel, are shown in Fig. 5.5. Finally,  $A(r_{ta})$  as calculated according to Eq. (5.8) with the  $\text{Im } G_c(r_{ta})$ ,  $\text{Re } G_c(r_{ta})$ , and  $D(r_{ta})$  as obtained above nicely follows the experimental data for both systems (Fig. 5.6).

### 5.3 Surface-state electron Kondo resonance

The Kondo resonances of 3d and 4f adatoms on the noble metal (111) surfaces [9, 10, 52, 53, 174] are localized to  $10 \text{ \AA}$  around the adatoms, as seen in the previous section.

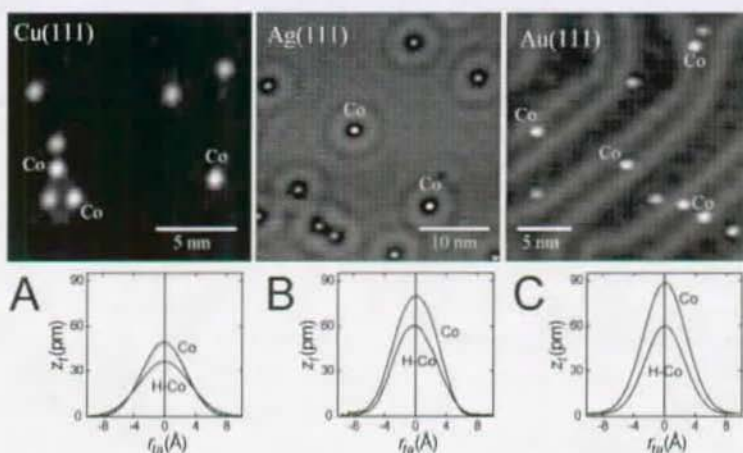


**Figure 5.7:** STM topographs of Co and H-Co adsorbates (not labelled) on the noble metal (111) surfaces. At low bias, the Co adatoms are imaged with a larger apparent height than the H-Co adsorbates due to their higher LDOS close to  $E_F$  (Fig. 5.8). **(A)** Cu(111), bias 60 mV,  $I = 0.5$  nA. **(B)** Ag(111), bias -60 mV,  $I = 0.8$  nA. **(C)** Au(111), bias 20 mV,  $I = 2$  nA.

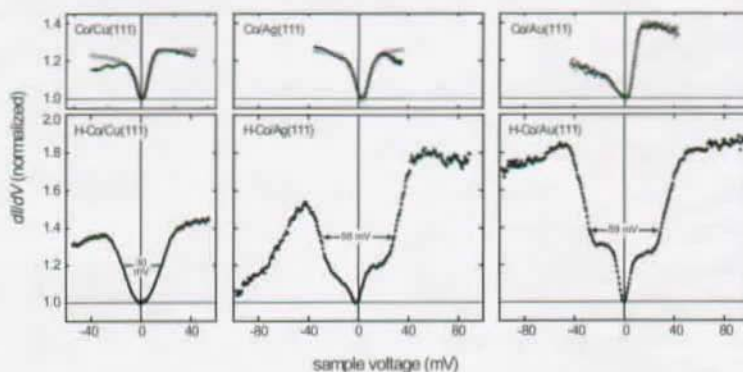


**Figure 5.8:** Differential conductance spectra taken with the STM tip centered on top of Co and H-Co adsorbates on the different noble metal (111) faces. Tunneling parameters prior to opening the feedback loop were  $\approx 100$  mV bias and  $I \approx 1$  nA, the  $dI/dV$  curves are taken using standard lock-in technique with a 4 kHz voltage modulation of  $\approx 1$  mV RMS applied to the sample. The grey lines are Fano line shape fits; average fit results for the Kondo temperatures are shown in Table 5.2. The arrows in the H-Co spectra indicate the full widths at half minimum of the overall dip. The spectra are normalized to their minimal value.

	$T_K$ of Co (K)	$T_K$ of H-Co (K)	$\xi_{\text{H-Co}}$ (nm)
Cu(111)	$54 \pm 3$	$175 \pm 7$	27.9
	$53 \pm 5$ [52]		
Ag(111)	$92 \pm 6$	$325 \pm 12$	5.6
Au(111)	$76 \pm 8$	$334 \pm 15$	16.7
	$75 \pm 6$ [55]		

**Table 5.2:** Kondo temperatures  $T_K$  of Co adatoms and H-Co complexes and their Kondo correlation lengths on the noble metal (111) surfaces. The values of the Co adatoms are from Fano line shape fits to the tunneling spectra recorded on-top of the atoms, the Kondo temperatures of the H-Co adsorbates are determined from the full width at half minimum of the corresponding tunneling spectra. All temperatures are average values from 10 different spectra taken on different adsorbates with different tip structures. The correlation length can be estimated with  $\xi_K \approx \hbar v_F^2 / k_B T_K$ , where  $v_F = \hbar k_F^s$  is the Fermi velocity of the surface-state.

Thus for these systems the interaction with bulk electrons and not the surface-states electrons dominates. The surface-state electrons are scattered into the bulk at the adsorbates and therefore do not contribute significantly to the Kondo resonance [59,174]. As will be shown in the following, the interaction with the surface-state electrons can significantly be enhanced when hydrogen is bound to the Co adatoms: The charge transfer associated with the H-Co bond weakens the Co bond to the substrate and thereby reduces the quenching of the surface-state in the vicinity of the Co atom. This allows for a stronger interaction of the 2D electron gas with the magnetic adsorbate and leads to a substantially increased spatial extent of the highly correlated Kondo state as well as to a fourfold increased Kondo temperature.

H-Co complexes (Fig. 5.7) are obtained as described in Section 4.1.1. Typical low bias  $dI/dV$  spectra taken with the tip centered on either the Co adatoms and the H-Co complexes on the noble metal (111) surfaces are shown in Fig. 5.8. The Fano line shaped spectra with low  $q$  of the bare Co adatoms (Fig. 5.8) are a consequence of the STM being more sensitive to the extended conduction band states than to the more localized  $d$ - or  $f$ -orbitals. For all three systems, the Kondo resonance is detectable only within  $10 \text{ \AA}$  of lateral tip-adatom distance  $r_{ta}$ , signaling that bulk and not surface-state electrons dominate the Kondo resonance [174]. The Kondo temperatures of Co adatoms on the three noble metal (111) surfaces as determined from fitting Fano line shapes to tunneling spectra are given in Table 5.2.

The  $dI/dV$  spectra taken on top of the H-Co complexes are quite different (Fig. 5.8): For H-Co on Cu(111), there is a symmetric antiresonance of  $\approx 30 \text{ meV}$  at zero bias, for

H-Co on Au(111) and Ag(111), a dip-like feature at zero bias similar to the one of the pure Co is embedded in a broader and more prominent reduction of the conductance with a FWHM of  $\approx 60$  mV. We first turn to this dominant feature: it can be interpreted to be due to a Kondo effect of the hydrogenated Co with a strong involvement of the surface-state electrons. Since the Kondo temperature depends exponentially on the electron charge density at the Kondo impurity, on the coupling strength, and on the energy of the hybridized  $d$ -level (see Eq. (5.5)), small changes in these quantities alter  $T_K$  substantially [48]. The Kondo temperatures of the H-Co spectra for the three noble metal (111) surfaces, determined by the full width at half minimum of the spectra, are given in Table 5.2. At all three surfaces the Kondo temperature of the hydrogenated cobalt is found to be substantially increased with respect to  $T_K$  of the bare Co adatoms.

The strongest support of the idea of a Kondo resonance being due to the involvement of the two-dimensional electron gas of the surface-state electrons comes from its large spatial extent. The Kondo resonance as function of the lateral tip-adsorbate distance  $r_{ta}$  for the Co and H-Co adsorbates on the Ag(111) surface is investigated by taking  $dI/dV$  spectra for  $r_{ta}$  up to 20 nm and assembling them to a greyscale map (Fig. 5.9). In these maps the  $dI/dV$  spectra discussed so far are vertical line cuts. If one analyses horizontal line cuts the energy resolved Friedel oscillations due to the surface-state electrons scattering at the adsorbates become apparent (Fig. 5.9(C,D)). These "standing waves" are also visible in the topography of Fig. 5.7. In contrast to the case of the Co adatom (Fig. 5.9(B)), the  $dI(r_{ta})/dV$  spectra taken in the vicinity of the H-Co complex (Fig. 5.9(A)) show a very long range disturbance ( $\approx 100$  Å) of the dispersion relation  $E(k)$  of the Ag(111) surface-state. This disturbance can be described in terms of a scattering resonance of the surface-state electrons with an energy dependent phase shift around  $E_F$  as described in Section 2.3. The change in the LDOS due to scattering of 2D electron waves at an adsorbate is given by Eq.(2.17). Only  $s$ -wave scattering has to be considered because the spread of the scattering potential of the adsorbate is small compared to the relevant wave lengths. Whereas a 2D scattering wave falls off slowly with  $\approx 1/r$ , a 3D scattering wave as from bulk conduction electrons falls off more rapidly with  $\approx 1/r^2$ . In accordance, the bulk electron dominated Kondo feature of the Co adatoms cannot be detected for  $r_{ta} > 10$  Å. For more remote  $r_{ta}$ , the dispersion of the Ag(111) surface-state is seen to be preserved due to the dominance of absorptive scattering (Fig. 5.9(B)) [171]. The LDOS near the Co adatoms can be fitted by Eq.(2.17) with  $\alpha = \infty$ , i.e. total absorption of the surface-state electrons at the Co adatom. The adatoms thus acts like "black dot" scatterers with the impinging surface-state electrons scattered into bulk states [171]. The fitted  $k$  values follow a parabolic dispersion with an

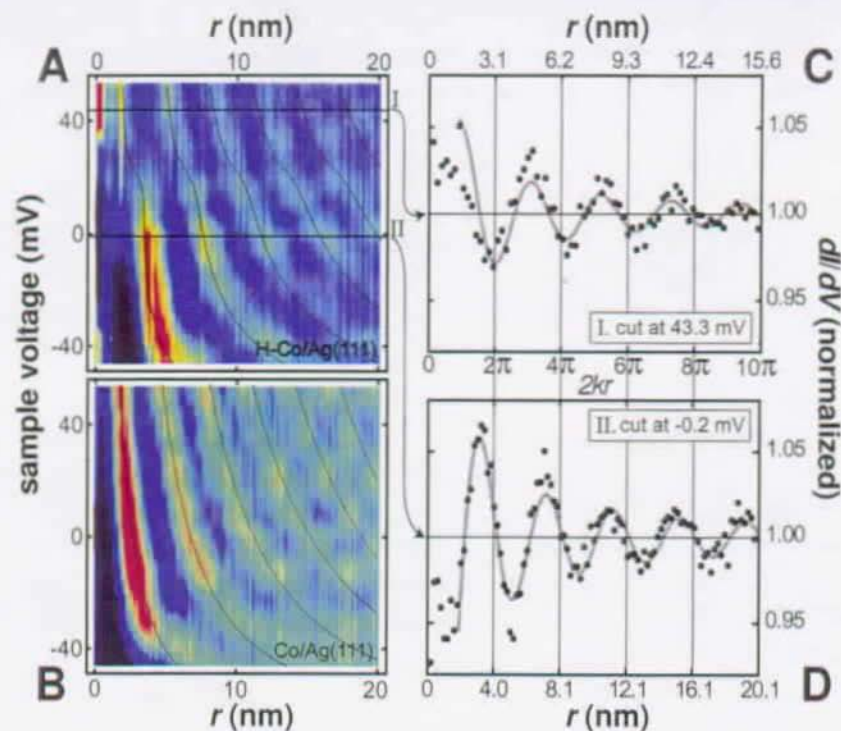


**Figure 5.9:** Color-scale LDOS( $E, r$ )-maps around a H-Co- (A) and a Co-adsorbate (B) on Ag(111), acquired by assembling  $dI(V)/dV$  spectra for tip-adsorbate distances  $r$  up to 20 nm with one spectrum every 2 Å. The spectra are normalized to background spectra taken far from any scatterer. The LDOS around the Co adatom (B) unveils the dispersion of the surface-state via the energy dependence of the wavelength of the electron standing waves. The dotted lines are calculated hyperbolas following the maxima of the standing waves with an effective mass  $m^* = 0.36$ , an onset at  $-65$  mV and full absorption  $\alpha = \infty$ . The standing waves in (A) have the same dispersion relation, but in addition they reveal an energy dependent scattering phase shift, best seen by the discontinuity of the first maximum of the scattered waves. The right column shows cuts of (A) for two different energies plotted against  $kr$  to make the change in the phase shift become apparent. The gray lines are fits of Eq. 2.17 with phase shifts  $\delta(-0.2 \text{ meV}) = 1.21$  and  $\delta(43.3 \text{ meV}) = -0.29$ . Only data points with  $r > 2$  nm were used in the fits to assure the validity of the asymptotic scattering wave formula (Eq. 2.17) and to prevent the interference of topographic effects on the spectra close to the adsorbate.

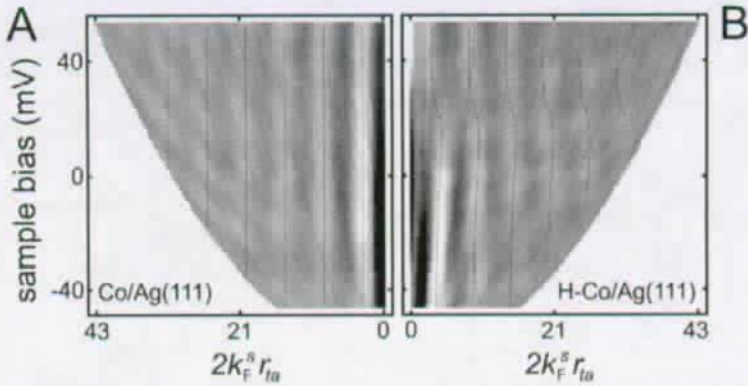


**Figure 5.10:** Grayscale LDOS( $E, r$ )-maps around a H-Co- (A) and a Co-adsorbate (B) on Ag(111). The same data as in Fig. 5.9 is plotted against  $k_F^s r_{ta}$  to eliminate the dispersion effects. Whereas the phase shift of the surface-state waves scattered by the Co adatom is independent of energy, H-Co scatters the surface-state waves with an energy dependent phase shift.

effective mass of  $m^* = 0.36$ , which compares well with published data for the Ag(111) surface-state of  $m^* = 0.40$  [27] (Table. 3.1).

In contrast, the surface-state waves scattered by a H-Co adsorbate have an energy dependent phase shift  $\delta_0(E)$  as seen most strikingly at small distances in the color scale plot (Fig. 5.9(A)). The change in the phase shift is clearly revealed by comparison of two scattered waves at different energy (Fig. 5.9(C,D)). The energy dependence of  $\delta_0(E)$  obtained from fits of Eq.(2.17) with absorption  $\alpha = 0.47$  to the  $dI(r_{ta})/dV$  data in Fig. 5.9(A) are shown in Fig. 5.11. The phase shift drops off rapidly close to the Fermi energy with a total change close to  $\pi$ . It can properly be described by a resonance law, Eq. (2.18). The change of the phase shift occurs in an energy range of  $\pm 30$  meV around  $E_F$  consistent with the width of the observed on-atom spectrum (Fig. 5.8). This resonant phase shift is a direct consequence of the spin screening as described by Fermi liquid theory of the Kondo effect [48]. Unlike the situation in the Anderson single impurity model we are dealing here with a real scatterer which also acts as a simple potential scatterer resulting in  $\delta_{bg}^0 \neq 0$ . In comparing e.g. the positions of the minima in the two line-cuts in Fig. 5.9(C) and Fig. 5.9(D) or the maxima in Fig. 5.10, it can be seen that the change in the phase shift is gradually reduced for  $r_{ta} > 100$  Å as one goes away from the Kondo impurity. The reason might be a loss of coherence in the electron correlation. The resonant phase shift should only be observable where the scattered

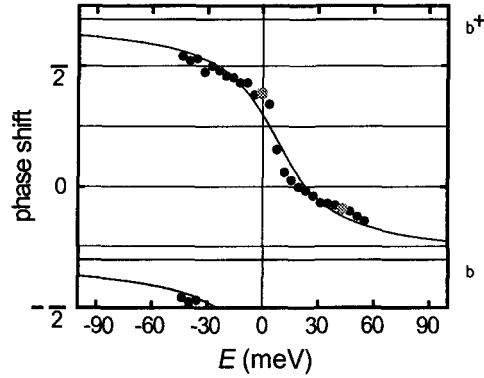


**Figure 5.11:** Energy dependence of the phase shift  $\delta_0(E)$  in the standing surface-state waves scattered by a H-Co adsorbate complex on the Ag(111) surface. The phase shifts are from fits of the scattering wave Eq.(2.17) with  $\alpha = 0.47$  to horizontal cuts in the LDOS( $E, r$ )-map as shown in Fig. 5.9 (the gray dots are from the fits shown in Figs. 5.9(C) and 5.9(D)). The black line is a fit of Eq. (2.18) with  $\delta_{bg}^0 = -0.96$ ,  $\Delta E = 7.6$  meV and  $\Gamma = 46$  meV.

electrons are correlated with the impurity spin. The correlation length can be simply estimated with  $\xi_K \propto \hbar v_F / k_B T_K$ , which gives  $\xi_K \approx 5.6$  nm using the parameters for the H-Co on Ag(111) system (Table. 5.2) consistent with the observed range of the resonant phase shift. Therefore this might be the first experimental indication of the extent of the Kondo cloud in a correlated electron system with a rather small  $\zeta_K$ .

Turning back to the H-Co spectrum (Fig. 5.8) it has to be noted that for H-Co on Ag(111) and Au(111), there is a spectral feature observable on the same energy scale as the Kondo resonance on the pure Co adatoms. The width and the spatial extent of this additional resonance is the same as that of the pure Co resonance, however, the line shape is not the same. The possibility of a switching of the Hydrogen from adsorbate to tip and consequently an overlapping of the pure Co spectrum with the H-Co spectrum is thus unlikely. For a double Kondo feature to appear there must be two independent spin states involved as shown recently for the case of a degenerate  $S = 1$  and  $S = 1/2$  system in a quantum dot [68]. From its fast spatial decay (within 10 Å), this narrow feature can be ascribed to an interaction with the bulk electronic system of the substrate. Further theoretical investigation will have to show whether the binding of H to a Co adsorbate can give rise to two independent Kondo systems that couple differently to surface-state and bulk conduction band electrons and hence are screened on different length and energy scales.

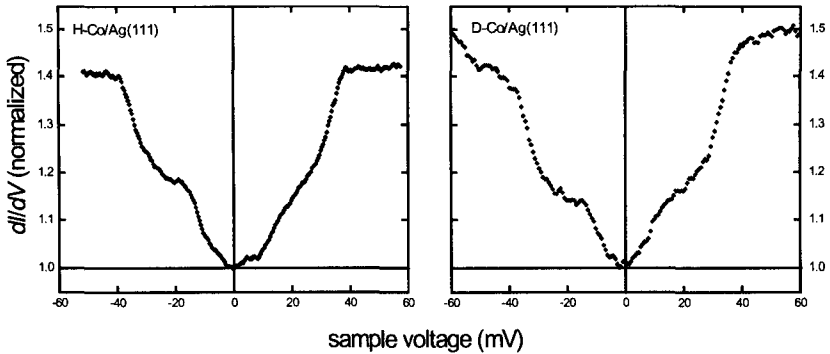


**Figure 5.12:** Differential conductance spectra taken with the STM tip centered on top of H-Co and D-Co adsorbates on Ag(111). Tunneling parameters prior to opening the feedback loop were 60 mV bias and  $I = 1.7$  nA, the  $dI/dV$  curves are taken using standard lock-in technique with a 4 kHz voltage modulation of 3 mV RMS applied to the sample. The spectra are normalized to their minimal value.

Another conceivable explanation of the H-Co  $dI/dV$  spectra would be in terms of inelastic electron tunneling (IETS). It is known that an excitation of vibrational modes of molecules by the tunneling current leads to small, sharp increases of the tunneling conductance when the energy of the tunneling current reaches the energy of a vibrational mode of the molecule in the tunneling junction [175]. This increase is due to a new tunneling channel for electrons which loose energy in the tunneling process by exciting a vibrational mode of the molecule. The increase of the tunneling conductance is at symmetric voltages for positive and negative tunneling bias because the direction of the tunneling current is not important. Thus, a vibrational mode which is excited by the tunneling electrons leads to a box-shaped dip in the  $dI/dV$  signal centered symmetrically around zero bias. The double-dip shaped H-Co spectra could accordingly be thought of as a superposition of a small Kondo antiresonance at zero bias and an extremely strong excitation of a vibrational mode at  $\approx 40$  meV related to the bond of the hydrogen to the cobalt. To check this interpretation, we performed the same kind of experiment with  $D_2$  instead of  $H_2$ . The two times higher isotopic mass of the deuterium should decrease the energy of the vibrational mode by a factor of  $1/\sqrt{2}$  [175]. The isotope experiment (see Fig. 5.12), however, clearly reveals no difference between the H-Co and D-Co spectra discarding an vibrational origin of the effect and thus supporting the electronic interpretation discussed above.



## 5.4 Summary

In summary to this chapter, spatially resolved scanning tunneling spectra taken on top and in the vicinity of individual Co adatoms and H-Co adsorbates on noble metal surfaces have been quantitatively analyzed. The Fano line shaped tunneling spectra close to zero bias are interpreted as fingerprints of the adsorbates' Kondo resonances. The comparison of the Fano resonances of Co adatoms on Cu(100) and Cu(111) reveals insight in several aspects of the physics of the Kondo effect: the higher Kondo temperature  $T_K = 88$  of Co/Cu(100) compared to  $T_K = 54$  for Co/Cu(111) can be ascribed to an increased embedding of the Co adatom in the copper host. Under consideration of  $T_K$  for a Co impurity in the bulk of a Cu host, a logarithmic scaling of  $T_K$  with the number of nearest substrate Cu atoms is found. From the rapid decay of the Fano line shape parameter  $q$  for Co/Cu(100) within a tip-adatom distance of 5 Å, it is concluded that for Co/Cu(100) both, tunneling into the hybridized localized state and into the substrate conduction band contribute to the observed spectra. In contrast, the latter channel is found to be dominant for Cu(111). The similar spatial decay of the amplitude of the Fano line shapes for Co on Cu(100) and Cu(111) reveals that the Kondo resonance is dominated by the bulk electrons and not the surface-state electrons. For Co on the other noble metal (111) surfaces of Ag(111) and Au(111), we observe similar Fano line shapes with  $T_K = 92$  for Co/Ag(111) and  $T_K = 76$  for Co/Au(111). Changing the chemical surrounding of the Co adatom by hydrogen adsorption strongly affects the bond of the Co to the noble metal substrates as concluded from the reduced migration barrier  $E_m = 38$  meV for H-Co/Ag(111) as compared to  $E_m = 50$  meV for Co/ag(111), as well as the tunneling spectra: the H-Co spectra have a double dip structure with an overall fwhm about four times increased as compared to the respective Co spectra. The coupling to the surface-state electrons is enhanced by the hydrogen adsorption: whereas the Co adatoms scatter the surface state electrons with an energy independent phase shift of about  $\pi/2$  characteristic of a black dot scatterer, the resulting strong Kondo resonance of the 2D surface-state electron gas can be detected for Co/Ag(111) up to distances of more than 100 Å away from the impurity site. This long-range behavior allows for a direct determination of the energy dependence of the scattering phase shift of a single Kondo impurity showing a resonant energy dependence close to the Fermi energy as expected from Fermi liquid theory.

# Chapter 6

## Outlook

The comparison of the adsorbate interactions of the three adsorbate/substrate systems which has been presented here suggests the general existence of long-range oscillatory adsorbate-adsorbate interactions and unravels the electronic origin and other common properties. Despite the fact that the observed interaction energies are small, they are expected to influence every adsorbate/substrate system with a 2DEG present at the surface. Particularly important for nucleation and growth processes is the short range region of the interaction energy  $E(r)$  for adsorbate-adsorbate distances smaller than 10 Å. We have tried to experimentally determine this range of  $E(r)$  more precisely by increasing the adsorbate coverage and thereby improving the statistic for small adsorbate distances. The problem to this method has been a stronger deviation from the assumption that the pair interaction of two isolated adsorbates can be determined by a nearest neighbor distance distribution. Third adsorbates close to a pair of adsorbates under survey generally increase the repulsion between the pair. A proper way to determine the short range region of the interaction energy would be to keep low coverages of adsorbates but increase the substrate temperature to get relatively more counts for the energetically unfavorable small distances. A high speed STM with an image recording rate of more than 10 Hz would then be needed to accurately determine the adsorbate positions of the rapidly diffusing adsorbates. Such an instrument might also be capable of tracing the diffusion of the single adsorbates until they nucleate or until they attach themselves to islands or substrate steps, allowing for the determination of the attachment barrier and giving direct insight in the effects of the interaction on nucleation and growth processes.

The observed adsorbate-adsorbate interactions can potentially be employed for the self-organized growth of ordered adsorbate superlattices. The obstacles to the formation of such structures, like misfits of the distances of the minima of the interaction energy

to the adsorption sites or an unfavorable proportion of the first minimum distance of the interaction energy to the second maximum distance, can probably be circumvented by using substrates with different types of surface-states and by using adsorbates of different shapes and with different scattering properties. Also, it is possible to tune the surface-state parameters of a substrate and the scattering properties of the adsorbates: For example, we have been able to adjust the Fermi wavelength of the Au(111) surface-state by epitaxially growing monolayers of Ag onto the Au(111) surface, whereby the surface-state Fermi wavelength changes gradually from the Au(111) value to the one of Ag(111) within a few atomic layers. The phase shift of an adsorbate is linked to the charge state of the adsorbate by Friedel's sum rule [176], i.e. the phase shift can possibly be tuned by co-adsorption of electronegative or -positive species. That co-adsorption may strongly influence the scattering properties of an adsorbate has been demonstrated here by a the reduced surface-state electron absorption at H-Co complexes compared to Co adatoms. Interactions between different kinds of adsorbates or with other scatterers may also be exploited to grow superstructures. For example, the surface-state electron density oscillation due to scattering by steps are stronger and more long-ranged because of the increased dimension of the scatterer. These LDOS oscillations at atomic steps may be used to grow chains of adsorbates separated by half the surface-state Fermi wave length on vicinal surfaces. Similar effects might be achieved with large, longish molecules.

The adsorbate interaction studied here has been interpreted in terms of conventional Friedel oscillations. Anomalous correlation-enhanced Friedel oscillation have been predicted for a high density of randomly distributed scatterers with mean distances of about the Fermi wavelength [177]. These enhanced Friedel oscillations have been used to explain the unusual thermal stability of certain amorphous alloys [178]. An enhancement of the standing surface-state density Friedel oscillations may be directly analyzed with the methods and systems described here by evaporating an increasing coverage of adatoms onto the noble metal (111) surfaces and comparing the amplitudes of the surface-state density oscillations in the topographic STM mode. Care would have to be taken that the tip does not change its structure between the evaporation steps to enable a comparison of the amplitude of the oscillations. Also, the substrate temperature would have to be kept low enough during evaporation so that the adatoms are frozen and cannot arrange themselves due to their long-range interaction.

Questions remain about the origin of the strong effect that hydrogen absorption has on the electronic properties of the Co adatoms on the three noble metal (111) surfaces. Neither the huge increase of the Kondo temperature nor the double-dip structure of the

tunneling spectra are well understood. Since the Kondo resonance is a resonance in the LDOS of the 3d orbital of the Co, the hydrogen absorption most probably has a strong effect on the 3d orbital. A trend related to the occupation and magnetic moment of the 3d orbital might be revealed, if similar effects of hydrogen absorption could be observed for other magnetic 3d adatoms. The local character of the magnetic moments of the pristine Co adatoms compared to the H-Co adsorbates can be investigated by X-ray magnetic circular dichroism. To learn more about the chemical bonds of the hydrogen and the cobalt, it might also be instructive to examine the H-Co adsorbates by surface vibration spectroscopic techniques like electron energy loss spectroscopy.

Instead of modifying the local magnetic moment, altering the conduction electron spectrum has a strong effect on the Kondo resonance as well. For example, it has been predicted that by reducing the extensions of the metallic host so far that the mean energy level spacing becomes comparable to the Kondo energy  $k_B T_K$ , the Kondo resonance of a magnetic impurity in the metal grain splits up into a series of subpeaks corresponding to the discrete box levels [179]. Such a splitting of the Kondo resonance has been observed for Co clusters on short nanotubes [56]. A system investigable by STS with a high control over the size of the “Kondo box” may be realized by growing metallic islands on conducting substrates, with a thin insulating layer in between to reduce the conduction electron coupling, and subsequently evaporating low coverages of magnetic adatoms onto the islands. The effect of the energy level discretisation on the Kondo resonance may then be analyzed by taken tunneling spectra on magnetic adatoms sitting on islands of different diameter and thickness.

Atomic manipulation provides new means for the investigating of the physics of the Kondo effect. Chen *et al.* [51] have studied the interaction of two Kondo resonances by moving together in increments a single pair of magnetic adatoms. It was found that the resonances disappear abruptly for interatomic distances of less than 6 Å, which has been explained with a drop of the Kondo temperature due to a reduced exchange coupling to the conduction electrons. The same kind of measurement could be done with the H-Co complexes studied here. The strong interaction with the surface-state should lead to a long-ranged interaction of two complexes making possible a more detailed analysis of the distance dependence of the interaction of two Kondo impurities. Also, the increased coupling to the surface-state electrons should enhance the mirage effect observed by Manoharan *et al.* [52], where the surface-state LDOS of a magnetic adatom was projected from one focus of an ellipse corral to the other, empty focus. Another way to use atomic manipulation is to modify the magnetic adatom’s substrate surrounding. The scaling of the Kondo temperature with the number of nearest neighbor substrate

atoms shown here might be further investigated by moving the magnetic adatoms to step edges or embedding it with an increasing number of substrate atoms.

A non-ambiguous test for the spin related origin of the resonance would be the quenching of the Kondo singlet state in a strong magnetic field. We have not been able to observe any effect on the tunneling resonances for magnetic fields up to 5 T, what is probably a consequence of the relatively high thermal energy of  $k_B T$  at 6 K compared to the Zeeman energy of  $\mu_B B$ . The new Scanning Tunneling Microscopes running at sub Kelvin temperatures with magnets providing fields of more than 10 T that are currently being build in several groups, might be capable of observing this effect for systems with low Kondo temperature.

# Bibliography

- [1] G. Binning, H. Rohrer, C. Gerber, and E. Weibel, Phys. Rev. Lett **49**, 57 (1982).
- [2] G. Binning and H. Rohrer, Helvetica Physica Acta **55**, 726 (1982).
- [3] J. S. Foster, J. E. Frommer, and P. C. Arnett, Nature **331**, 324 (1988).
- [4] D. M. Eigler and E. K. Schweizer, Nature **344**, 524 (1990).
- [5] G. Meyer, B. Neu, and K. H. Rieder, Applied Physics A - Materials Science and Processing **60**, 343 (1995).
- [6] G. Meyer, S. Zophel, and K. H. Rieder, Phys. Rev. Lett. **77**, 2113 (1996).
- [7] S. A. Elrod, A. L. de Lozanne, and C. F. Quate, Appl. Phys. Lett. **45**, 1240 (1984).
- [8] H. F. Hess, R. B. Robinson, R. C. Dynes, and J. V. Valles, J. M. anf Waszczak, Phys. Rev. Lett. **62**, 214 (1984).
- [9] J. Li, W. D. Schneider, R. Berndt, and B. Delley, Phys. Rev. Lett. **80**, 2893 (1998).
- [10] V. Madhavan *et al.*, Science **280**, 567 (1998).
- [11] S. G. Davison and M. Stęślicka, *Basic Theory of Surface States* (Oxford University Press, New York, 1992).
- [12] E. Bertel and M. Donath, *Electronic Surface and Interface States on Metallic Systems* (Wolrd Scientific Publishing, Singapore, 1995).
- [13] L. C. Davis, Phys. Rev. B **43**, 3821 (1991).
- [14] M. F. Crommie, C. P. Lutz, and D. M. Eigler, Nature **363**, 524 (1993).
- [15] Y. Hasegawa and P. Avouris, Phys. Rev. Lett. **71**, 1071 (1993).
- [16] M. F. Crommie, C. P. Lutz, and D. M. Eigler, Science **262**, 218 (1993).

- [17] P. Avouris and I. W. Lyo, *Science* **264**, 942 (1994).
- [18] P. Avouris, I. W. Lyo, R. E. Walkup, and Y. Hasegawa, *J. Vac. Sci. Technol. B* **12(3)**, 1447 (1994).
- [19] G. Hörmandinger, *Phys. Rev. Lett.* **73**, 910 (1994).
- [20] P. Avouris, I. W. Lyo, and P. Molinàs-Mata, *Chem. Phys. Lett.* **240**, 423 (1995).
- [21] J. Li, W. D. Schneider, and R. Berndt, *Phys. Rev. B* **56**, 7656 (1997).
- [22] L. Peterson, P. Laitenberger, E. Laegsgaard, and F. Besenbacher, *Phys. Rev. B* **58**, 7361 (1998).
- [23] J. Li, W. D. Schneider, R. Berndt, and S. Crampin, *Phys. Rev. Lett.* **80**, 3332 (1998).
- [24] L. Peterson, *Phys. Rev. B* **57**, R6858 (1998).
- [25] J. Li, W. D. Schneider, R. Berndt, and S. Crampin, *Phys. Rev. Lett.* **81**, 4464 (1998).
- [26] L. Bürgi, O. Jeandupeux, H. Brune, and K. Kern, *Phys. Rev. Lett.* **81**, 5370 (1998).
- [27] O. Jeandupeux *et al.*, *Phys. Rev. B* **59**, 15926 (1999).
- [28] L. Bürgi, O. Jeandupeux, H. Brune, and K. Kern, *Phys. Rev. Lett.* **82**, 4516 (1999).
- [29] L. Bürgi, H. Brune, and K. Kern, *J. Electron Spec. and Rel. Phen.* **109**, 33 (2000).
- [30] L. Bürgi, G. Peterson, H. Brune, and K. Kern, *Surface Science* **447**, L157 (2000).
- [31] I. Klier, *Science* **288**, 1399 (2000).
- [32] W. D. Schneider and R. Berndt, *J. Electron Spec. and Rel. Phen.* **109**, 199 (2000).
- [33] L. Bürgi *et al.*, *Appl. Phys. A - Material Science and Processing* **75**, 141 (2002).
- [34] J. Trost, T. Zambelli, J. Wintterlin, and G. Ertl, *Phys. Rev. B* **54**, 17850 (1996).
- [35] J. Barth *et al.*, *Phys. Rev. B* **55**, 12902 (1997).
- [36] S. Renisch, R. Schuster, J. Wintterlin, and G. Ertl, *Phys. Rev. Lett.* **82**, 3839 (1999).

- [37] L. Österlund *et al.*, Phys. Rev. Lett. **83**, 4812 (1999).
- [38] G. Ehrlich and F. Watanabe, Langmuir **7**, 2555 (1991).
- [39] S. J. Koh and G. Ehrlich, Phys. Rev. Lett. **87**, 106103 (2001).
- [40] T. T. Tsong, *Atom-probe field ion microscopy* (Cambridge University Press, New York, 1990).
- [41] G. L. Kellogg, Surf. Sci. Rep. **21**, 1 (1994).
- [42] K. H. Lau and W. Kohn, Surf. Sci. **75**, 69 (1978).
- [43] E. Wahlström, I. Ekvall, H. Olin, and L. Walldé, Appl. Phys. A **66**, 1107 (1998).
- [44] J. Repp *et al.*, Phys. Rev. Lett. **85**, 2981 (2000).
- [45] N. Knorr, H. Brune, M. A. Schneider, and K. Kern, *Direct evidence of surface-state long-range interactions for Cu atoms on Cu(111)* (ECOSS 19, Madrid, September 2000).
- [46] N. Knorr *et al.*, Phys. Rev. B **65**, 115420 (2002).
- [47] J. Kondo, Progress in Theoretical Physics **32**, 37 (1964).
- [48] G. Grosso and G. P. Parravicini, *The Kondo Problem to Heavy Fermions* (Cambridge University Press, Cambridge, 1993).
- [49] W. D. Schneider, Pramana - Journal of Physics **52**, 537 (1999).
- [50] R. Berndt, J. T. Li, W. D. Schneider, and B. Delley, Physica Status Solidi B-Basic Research **215**, 845 (1999).
- [51] W. Chen, T. Jamneala, V. Madhavan, and M. F. Crommie, Phys. Rev. B **60**, R8529 (1999).
- [52] H. Manoharan, C. P. Lutz, and D. M. Eigler, Nature **403**, 512 (2000).
- [53] T. Jamneala, V. Madhavan, W. Chen, and M. F. Crommie, Phys. Rev. B **61**, 9990 (2000).
- [54] W. D. Schneider and R. Berndt, J. Of Electron Spec. and Related Phenomena **109**, 19 (2000).
- [55] V. Madhavan *et al.*, Phys. Rev. B **64**, 165412 (2001).



- [56] T. W. Odom, J. L. Huang, C. L. Cheung, and C. M. Lieber, *Science* **290**, 1549 (2000).
- [57] O. Y. Kolesnychenko *et al.*, *Nature* **415**, 507 (2002).
- [58] K. Nagaoka, T. Jamneala, M. Grobis, and M. F. Crommie, *Phys. Rev. Lett.* **88**, 077205 (2002).
- [59] M. A. Schneider, L. Vitali, N. Knorr, and K. Kern, *Phys. Rev. B* **65**, 121406(R) (2002).
- [60] D. Goldhaber-Gordon, *Nature* **391**, 156 (1998).
- [61] D. Goldhaber-Gordon, *Phys. Rev. Lett.* **81**, 5225 (1998).
- [62] S. M. Cronenwett and L. P. Oosterkamp, T. H. abd Kouwenhoven, *Science* **281**, 540 (1998).
- [63] L. P. Rokhinson, L. J. Guo, S. Y. Chou, and D. C. Tsui, *Science* **60**, R16319 (1999).
- [64] S. Sasaki *et al.*, *Nature* **405**, 764 (2000).
- [65] W. G. van der Wiel *et al.*, *Science* **289**, 2105 (2000).
- [66] Y. Ji *et al.*, *Science* **290**, 779 (2000).
- [67] H. Jeong, A. M. Chang, and M. R. Melloch, *Science* **293**, 2221 (2001).
- [68] W. G. van der Wiel *et al.*, *Phys. Rev. Lett.* **88**, 126803 (2002).
- [69] D. Sprinzak *et al.*, *Phys. Rev. Lett.* **88**, 176805 (2002).
- [70] S. Sasaki *et al.*, *Physica E* **12**, 806 (2002).
- [71] J. Nygård, D. H. Cobden, and P. E. Lindelof, *Nature* **408**, 342 (2000).
- [72] W. J. Liang *et al.*, *Nature* **417**, 725 (2002).
- [73] J. Park *et al.*, *Nature* **417**, 722 (2002).
- [74] L. Kouwenhoven and G. Glazman, *Physics World* **14**, 33 (2001).
- [75] A. Hirstein, Ph.D. thesis, EPF Lausanne, 1998.
- [76] L. Bürgi, Ph.D. thesis, EPF Lausanne, 1999.

- [77] K. Besocke, *Surface Science* **181**, 145 (1987).
- [78] J. Bardeen, *Phys. Rev. Lett.* **6**, 57 (1961).
- [79] E. L. Wolf, *Principles of Electron Tunneling Spectroscopy* (Oxford University Press, New York, 1985).
- [80] *Methods of Experimental Physics*, edited by J. Stroscio and W. Kaiser (Academic, San Diego, 1993), Vol. 27.
- [81] R. Wiesendanger, *Scanning Probe Microscopy and Spectroscopy*, . (Cambridge University Press, Cambridge, 1994).
- [82] C. J. Chen, *Introduction to Scanning Tunneling Microscopy*, . (Springer, Berlin, 1996).
- [83] J. Tersoff and D. R. Hamann, *Phys. Rev. Lett.* **50**, 1998 (1983).
- [84] A. Selloni, P. Carnevali, E. Tosatti, and C. D. Chen, *Phys. Rev. B* **31**, 2602 (1985).
- [85] N. D. Lang, *Phys. Rev. B* **34**, 5947 (1986).
- [86] G. H rmandinger, *Phys. Rev. B* **49**, 13897 (1994).
- [87] C. Cohen-Tannoudji, B. Diu, and F. Lalo , *Quantum Mechanics* (Wiley-Interscience, New York, 1977).
- [88] J. Friedel, *Nuovo Cimento Suppl.* **7**, 287 (1958).
- [89] T. F. Page and B. Ralph, *Nature Phys. Sci.* **234**, 163 (1971).
- [90] D. M. Newns, *Physical Review* **178**, 1123 (1969).
- [91] J. W. Gadzuk, *Surface Science* **43**, 44 (1974).
- [92] L. D. Landau and E. M. Lifshitz, *Quantum Mechanics: Non-Relativistic Theory*, 3 ed. (Pergamon Press, ., 1977).
- [93] U. Fano, *Physical Review* **124**, 1866 (1961).
- [94] U. Fano, *Nuovo Cimento* **12**, 156 (1935).
- [95] P. W. Anderson, *Physical Review* **124**, 41 (1961).
- [96] G. Grosso and G. P. Parravicini, *Solid State Physics* (Academic Press, San Diego, 2000).

- [97] E. N. Economou, *Green's functions in quantum physics* (Springer, Berlin, 1990).
- [98] M. Plihal and J. W. Gadzuk, Phys. Rev. B **63**, 085404 (2001).
- [99] M. Mehta-Ajmani, I. P. Betra, E. E. Lafon, and C. S. Fadley, J. Phys. C **13**, 2807 (1980).
- [100] H. Lüth, *Surfaces and Interfaces of Solid Materials* (Springer, Berlin, 1995).
- [101] P. M. Echenique, Progress in Surface Science **67**, 271 (2000).
- [102] E. Bertel, Phys. Rev. B **52**, R14384 (1997).
- [103] N. Memmel, Surface Science Reports **32**, 91 (1998).
- [104] E. Bertel, P. Roos, and J. Lehmann, Phys. Rev. B **52**, R14384 (1995).
- [105] N. Memmel and E. Bertel, Physikalische Blätter **53**, 323 (1997).
- [106] N. Memmel and E. Bertel, Phys. Rev. Lett. **75**, 485 (1995).
- [107] N. Garcia and P. A. Serena, Surface Science **330**, L665 (1995).
- [108] A. Zangwill, *Physics at Surfaces* (Cambridge University Press, New York, 1988).
- [109] P. O. Gartland and B. J. Slagsvold, Phys. Rev. B **12**, 4047 (1975).
- [110] J. Tersoff and S. D. Kevan, Phys. Rev. B **28**, 4267 (1983).
- [111] H. Courths and S. Hüfner, Physics Reports **112**, 53 (1984).
- [112] T. C. Hsieh, T. Miller, and T. C. Chiang, Phys. Rev. Lett. **55**, 2483 (1985).
- [113] S. D. Kevan and R. H. Gaylord, Phys. Rev. B **36**, 5809 (1987).
- [114] Z. Qu, J. Vac. Sci. Technol. A **12**(4), 2187 (1994).
- [115] R. Paniago, R. Matzdorf, G. Meister, and A. Goldmann, Surface Science **336**, 113 (1995).
- [116] B. A. McDougall, T. Balasubramanian, and E. Jensen, Phys. Rev. B **51**, 13891 (1995).
- [117] R. Matzdorf, G. Meister, and A. Golmann, Phys. Rev. B **54**, 14807 (1996).
- [118] S. LaShell, B. A. McDougall, and E. Jensen, Phys. Rev. Lett. **77**, 3419 (1996).

- [119] R. Matzdorf, Surf. Sci. Rep. **30**, 153 (1998).
- [120] A. Mugarza, Phys. Rev. Lett. **87**, 107601 (2001).
- [121] V. Y. Yurov, Physics of Low-Dimensional Structures **11**, 155 (2001).
- [122] A. Bendounan, Surface Science **496**, L43 (2002).
- [123] F. Baumberger, T. Greber, B. Delley, and J. Osterwalder, Phys. Rev. Lett. **88**, 237601 (2002).
- [124] S. L. Hulbert, Phys. Rev. B **31**, 6815 (1985).
- [125] S. L. Hulbert, P. D. Jhonson, N. G. Stoffel, and N. V. Smith, Phys. Rev. B **32**, 3451 (1985).
- [126] D. P. Woodruff, W. A. Royer, and N. V. Smith, Phys. Rev. B **34**, 764 (1986).
- [127] A. Goldmann, V. Dose, and G. Borstel, Phys. Rev. B **32**, 1971 (1985).
- [128] N. W. Ashcroft and N. D. Mermin, *Solid State Physics* (HRW, Philadelphia, 1976).
- [129] J. A. Vergés and E. Louis, Solid State Communications **22**, 663 (1977).
- [130] S. Crampin, J. Electron Spec. and Rel. Phen. **109**, 51 (2000).
- [131] S. Datta, *Electronic Transport in Mesoscopic Systems* (Cambridge University Press, Cambridge, 1995).
- [132] Y. P. Monarkha and V. Shikin, Sov. J. Low Temp. Phys. **17**, 269 (1965).
- [133] C. G. Grimes, Surface Science **73**, 379 (1978).
- [134] H. Eyring, J. Chem. Phys. **3**, 107 (1935).
- [135] S. Glasstone, K. J. Laidler, and H. Eyring, *The Theory of Rate Processes* (McGraw-Hill, New York, 1941).
- [136] P. Hänggi, P. Talkner, and M. Borkovec, Rev. Mod. Phys. **62**, 251 (1990).
- [137] G. Wahnström, in *Interaction of Molecules with Solid Surfaces*, edited by V. Bortoloni, N. M. March, and M. P. Tosi (Plenum Press, New York, 1990).
- [138] G. H. Vineyard, J. Phys. Chem. Solids **3**, 121 (1957).
- [139] A. F. Voter and J. D. Doll, J. Chem. Phys. **80**, 5883 (1984).

- [140] C. Ratsch and M. Scheffler, Phys. Rev. B **58**, 13163 (1998).
- [141] V. P. Zhdanov, Surf. Sci. Rep. **12**, 183 (1991).
- [142] R. Gomer, Rep. Prog. Phys. **53**, 917 (1990).
- [143] D. M. Eigler and E. K. Schweizer, Nature **344**, 524 (1990).
- [144] J. A. Strosio and D. M. Eigler, Science **254**, 1319 (1991).
- [145] G. Meyer, S. Zophel, and K. H. Rieder, Appl. Phys. A - Materilas Science and Prcessing **63**, 557 (1996).
- [146] G. Dujardin, Phys. Rev. Lett. **80**, 3085 (1998).
- [147] S. Gauthier, Applied Surface Science **164**, 84 (2000).
- [148] A. Bogicevic *et al.*, Phys. Rev. Lett. **85**, 1910 (2000).
- [149] G. L. Kellog, Phys. Rev. B **55**, 7206 (1997).
- [150] S. Horch *et al.*, Nature **398**, 134 (1999).
- [151] R. Stumpf, Phys. Rev. B **53**, R4253 (1996).
- [152] T. L. Einstein, CRC Crit. Rev. Sol. State Mater. Sci. **7**, 261 (1978).
- [153] K. H. Lau and W. Kohn, Surf. Sci. **65**, 607 (1977).
- [154] T. L. Einstein, Surface Science **75**, 161L (1978).
- [155] T. L. Einstein, in *Handbook of Surface Science*, edited by W. N. Unertl (Elsevier Science, ., 1996).
- [156] K. A. Fichthorn and M. Scheffler, Phys. Rev. Lett. **84**, 5371 (2000).
- [157] V. S. Stepanyuk *et al.*, submitted ., . (2002).
- [158] P. Hyldgaard and M. Persson, J. Phys. Cond. Mat. **12**, L13 (2000).
- [159] S. Ovesson, A. Bogicevic, G. Wahnström, and B. I. Lundqvist, Phys. Rev. B **64**, 125423 (2001).
- [160] J. V. Barth *et al.*, Phys. Rev. Lett. **84**, 1732 (2000).
- [161] M. M. Kamna, S. J. Stranick, and P. S. Weiss, Science **274**, 118 (1996).

- [162] B. J. Hinch, J. W. M. Frenken, G. Zhang, and J. P. Toennies, *Surface Science* **259**, 288 (1991).
- [163] P. Hyldgaard and T. L. Einstein, *Europhysics Letters* **59**, 265 (2002).
- [164] P. Hyldgaard and T. L. Einstein, *Elsevier Science* ., . (2002).
- [165] G. T. Rado and H. Suhl, *Magnetism* (Academic Press, ., 1973), Vol. V.
- [166] K. D. Schrieffer and P. A. Wolf, *Phys. Rev.* **149**, 491 (1966).
- [167] O. Újsághy, J. Kroha, L. Szunyogh, and A. Zawadowski, *Phys. Rev. Lett.* **85**, 2557 (2000).
- [168] P. Nozières, *J. Low Temp. Phys.* **17**, 31 (1974).
- [169] F. D. M. Haldane, *Phys. Rev. Lett.* **40**, 416 (1978).
- [170] A. Schiller and S. Hershfield, *Phys. Rev. B* **61**, 9036 (2000).
- [171] E. J. Heller, M. F. Crommie, C. P. Lutz, and D. M. Eigler, *Nature* **369**, 464 (1994).
- [172] G. A. Fiete *et al.*, *Phys. Rev. Lett.* **86**, 2392 (2001).
- [173] S. D. Kevan, *Phys. Rev. Lett.* **50**, 526 (1983).
- [174] N. Knorr *et al.*, *Phys. Rev. Lett.* **88**, 096804 (2002).
- [175] B. C. Stipe, M. A. Rezaei, and W. Ho, *Science* **280**, 1732 (1998).
- [176] J. M. Ziman, *Theory of Solids* (Cambridge University Press, Cambridge, 1972).
- [177] J. Kroha, *J. Non-Crystalline Solids* **250**, 865 (1999).
- [178] P. Häusler, *Phys. Rep.* **222**, 65 (1992).
- [179] W. B. Thimm, J. Kroha, and J. von Delft, *Phys. Rev. Lett.* **82**, 2143 (1999).



# Acknowledgments

I thank Professor Klaus Kern, the director of my thesis, for giving me the opportunity to work in his group and for his guidance in the preparation of the publications. I am especially grateful to Alexander Schneider who supervised this work, for working closely with me and for his constant motivation in keeping the system running.

I want to thank my predecessors Andreas Hirstein and Lukas Bürgi, who build the system and who introduced the surface-state know-how to the group. I thank Lucia Vitali, Peter Wahl and Lars Diekhöner for fruitful discussions and helping me with the measurements and Ralph Vogelgesang for introducing me to Green's function. I thank Harry Brune and Max Eppele for their strong motivation on adsorbate-interactions and their accompaniment on the rocky road to getting it published, Kees Flipse for his stirring motivation concerning everything related to "Kondo" and Hans Kroha for valuable theoretical discussions and for being an expert to my thesis.

I also want to thank the other members of the jury for judging this thesis: Prof. B. Deveaud-Plédran, Dr. D. Pavuna, and Prof. L. Schlapbach.

All people working at the Institut de Physique des Nanostructures, both the scientific and the technical staff, I would like to thank. The nice lake Geneva region seems to have a positive impact on people's sentiment. It has been a pleasure to work there! During my time in Lausanne I found more than colleagues in Didi Peterka, Jense Weckesser, Renald Schaub, and Samuel Sarbach.

Mein ganz besondere Dank gilt meiner Familie, die all dies ermöglicht hat.





# Curriculum vitae

Name:	Nikolaus Knorr
Date of Birth:	November 22, 1973
Nationality:	German
October 2002	PhD thesis: "Electronic Interactions at Noble Metal Surfaces studied by Scanning Tunneling Microscopy"
2000–2002	Research assistant in the group of Prof. K. Kern in the department of Nanoscale Science at the Max-Planck-Institut für Festkörperforschung in Stuttgart, Germany
1999–2000	Research and teaching assistant in the group of Prof K. Kern at the Institute for Experimental Physics of the Swiss Federal Institute of Technology in Lausanne, Switzerland
1997–1998	Diploma thesis in the group of Prof. B. Hillebrands at the department of Solid State Physics of the Universität Kaiserslautern: "Magnetische Eigenschaften atomar geschichteter Eisen\Gold-Vielfachschichten"
1995–1996	Diploma studies in physics at the Université Joseph Fourier, Grenoble
1994–1998	Diploma studies in physics at the Universität Kaiserslautern, Kaiserslautern
1992–1994	Diploma studies in physics at the Johannes Gutenberg Universität, Mainz
1986–1987	Middle School at the Dewitt Middle School in Ithaca, New York, USA
1983–1992	Middle and High School at the Gymnasium Mainz-Gonsenheim, Germany



# Publications

V. S. Stepanyuk, A. N. Baranov, D. Tsivlin, W. Hergert, P. Bruno, N. Knorr, M. A. Schneider, K. Kern,  
“Quantum Interference and Long-Range Adsorbate-Adsorbate Interaction”,  
submitted.

N. Knorr, M. A. Schneider, C. F. J. Flipse, L. Vitali, L. Diekhöner, P. Wahl, H. Brune, and K. Kern,  
“Giant Kondo resonance of H-Co complexes on noble metal (111) surfaces”,  
submitted.

N. Knorr, M. A. Schneider, L. Diekhöner, P. Wahl, and K. Kern,  
“Kondo effect of single Co adatoms on Cu surfaces”,  
Physical Review Letters **88**, 096804 (2002).

L. Bürgi, N. Knorr, H. Brune, M. A. Schneider, and K. Kern,  
“Two-dimensional electron gas at noble-metal surfaces”,  
Applied Physics A-Material Science and Processing **75**, 141 (2002).

M. A. Schneider, L. Vitali, N. Knorr, and K. Kern,  
“Observing the scattering phase shift of isolated Kondo impurities at surfaces”,  
Physical Review B **65**, 121406 (2002).

N. Knorr, H. Brune, M. Eppe, A. Hierstein, M. A. Schneider, and K. Kern,  
“Long-range adsorbate interactions mediated by a two-dimensional electron gas”,  
Physical Review B **65**, 115420 (2002).